



HAL
open science

Equilibrium and Nonequilibrium Behaviours of 1D Bose Gases

Yiyuan Bess Fang

► **To cite this version:**

Yiyuan Bess Fang. Equilibrium and Nonequilibrium Behaviours of 1D Bose Gases. Optics [physics.optics]. Institut d'Optique Graduate School, 2014. English. NNT : 2014IOTA0005 . tel-01127046

HAL Id: tel-01127046

<https://pastel.hal.science/tel-01127046>

Submitted on 6 Mar 2015

HAL is a multi-disciplinary open access archive for the deposit and dissemination of scientific research documents, whether they are published or not. The documents may come from teaching and research institutions in France or abroad, or from public or private research centers.

L'archive ouverte pluridisciplinaire **HAL**, est destinée au dépôt et à la diffusion de documents scientifiques de niveau recherche, publiés ou non, émanant des établissements d'enseignement et de recherche français ou étrangers, des laboratoires publics ou privés.

INSTITUT D'OPTIQUE GRADUATE SCHOOL
ÉCOLE DOCTORALE ONDES ET MATIERE

DISCIPLINE Physique

THÈSE

pour l'obtention du grade de Docteur en science de l'Institut d'Optique Graduate School
préparée au Laboratoire Charles Fabry
soutenu le 01/10/2014

par
Bess FANG

**Equilibrium and Nonequilibrium Behaviors
of 1D Bose Gases**

Directeur de thèse :

Isabelle BOUCHOULE – Laboratoire Charles Fabry

Composition du jury :

Président du jury: Daniel ÉSTÈVE – CEA Saclay
Rapporteurs : David GUÉRY-ODELIN – Laboratoire de Collisions Agrégats Réactivité
József FORTÁGH – CQ Center for Collective Quantum Phenomena,
Universität Tübingen
Examineurs : Alain ASPECT – Laboratoire Charles Fabry
Chiara MENOTTI – BEC Center Trento
Membres invités : Patrizia VIGNOLO – Institut Non Linéaire de Nice
Björn HESSMO – Center for Quantum Technologies, Singapore

To Ola and Berge.

Contents

List of Acronyms	xi
List of Symbols	xiii
Acknowledgements	xix
Abstract	xxi
Introduction	3
I. 1D Tool Box	5
1. Atom Chip at Palaiseau	9
1.1. Reaching 1D regime	10
1.2. Experimental setup	11
1.3. Typical preparation sequence	17
2. Theory Overview	21
2.1. 1D Bose gas in a continuum	22
2.1.1. Lieb-Liniger model	22
2.1.2. Exact thermodynamics	23
2.1.3. 1D phase diagram	27
2.1.4. Beyond equation of state	28
2.2. 1D Bose gases in real life	29
2.2.1. Transverse trapping	29
2.2.2. Longitudinal trapping	31

3. Tools in the Box	35
3.1. Absorption imaging	38
3.2. In real space	38
3.2.1. Mean density profile	39
3.2.2. Atom-number fluctuations	41
3.2.3. Density ripples	45
3.3. In momentum space	48
3.3.1. Momentum distribution	50
3.3.2. Momentum correlations	52
II. Probing Nonequilibrium Systems	57
4. Breathing Modes	61
4.1. Motivation	62
4.2. Experimental procedures	63
4.2.1. Considerations	63
4.2.2. Procedures	64
4.2.3. Quantities of interest	65
4.3. Frequency study	67
4.3.1. Limiting cases	67
4.3.2. Crossovers	82
4.4. Lifetime studies	91
5. Long-lived Nonequilibrium States	95
5.1. Motivation	96
5.2. Experiments	96
5.2.1. Experiment 1: let's wait and see	98
5.2.2. Experiment 2: adjusting the evaporation parameters	100
5.3. Discussions	103
5.4. Future developments	105
6. Modifying the Interaction Strength	107
6.1. Motivation	108
6.2. Experiments	109
6.2.1. Modulation	109
6.2.2. Abrupt changes	113

6.2.3. Ramp	116
III. Beyond the Boundary	121
7. A New Imaging Objective	125
7.1. Motivation	126
7.1.1. Physics	127
7.1.2. Technology	129
7.1.3. Practical considerations	130
7.2. Problem	132
7.2.1. Optics	132
7.2.2. Mechanics	133
7.3. Solution	134
7.3.1. Design	135
7.3.2. Assembly	141
7.3.3. Testing	144
8. Other Technical Upgrades	153
8.1. About the atom chip	153
8.1.1. New layout	154
8.1.2. Exploring alternative fabrication processes	154
8.2. There is more light!	157
8.2.1. Hybrid magneto-optical potential	157
8.2.2. Updating the existing laser system	159
Concluding Remarks	163

List of Figures

1.1. 1D criterion	10
1.2. Atom chip	12
1.3. Vacuum system	14
1.4. Laser system	15
1.5. DDS card	16
1.6. Imaging system	17
1.7. Preparation sequence	20
2.1. 1D phase diagram	27
2.2. Local density approximation	32
3.1. Transverse integration	36
3.2. Routine to compute the density profile	40
3.3. Density profile, Palaiseau	41
3.4. Atom-number fluctuations, Palaiseau	44
3.5. Atom-number fluctuations, Heidelberg	45
3.6. $\tilde{g}_2(z, \tau_{\text{TOF}})$, Palaiseau	47
3.7. Density-ripples thermometry, Palaiseau	48
3.8. Focusing technique	49
3.9. Momentum distribution, Palaiseau	51
3.10. Momentum distribution, Amsterdam	53
3.11. Comparison of momentum correlations	54
4.1. Sequence of f_z quench	64
4.2. Profiles right after the f_z quench	65
4.3. Breathing mode: chart of various quantities	66
4.4. Breathing dynamics of a qBEC	69
4.5. Breathing mode of a qBEC: width variations	70
4.6. Breathing mode of a qBEC: scaling vs GPE	72

4.7. Breathing mode of an IBG: width variations	74
4.8. Breathing dynamics of a TG gas	77
4.9. Two colliding pendulums	79
4.10. Breathing dynamics of two colliding pendulums	81
4.11. Breathing mode: data in the 1D phase diagram	83
4.12. Breathing mode: the quasicondensation crossover	84
4.13. Demonstration of the ‘two-temperature’ phenomenon	86
4.14. Breathing mode of a sample in the quasicondensation crossover: width variations	88
4.15. Breathing mode: the qBEC to TG crossover	90
4.16. Breathing mode: lifetime	93
5.1. Sequence of RF frequency	98
5.2. Two temperatures: waiting	100
5.3. Two temperatures: sample data	101
5.4. Two temperatures: evaporation	102
6.1. Sequence of g_{1D} modulation	110
6.2. g_{1D} modulation: damping products	112
6.3. Sequence of g_{1D} double quench	114
6.4. g_{1D} double quench: long-time evolution of the widths	115
6.5. Sequence of g_{1D} ramp	116
6.6. g_{1D} ramp: momentum correlations	117
7.1. Spatial constraints of the new imaging objective	127
7.2. SNR considerations	129
7.3. Object NA of recent experiments with <i>ex vacuo</i> imaging optics	131
7.4. Result of the tolerance tests	139
7.5. Objective: drawing	140
7.6. Objective: simulated performance	142
7.7. ZYGO schematics	144
7.8. Objective test 1: measured PSF	146
7.9. Objective test 1: measured encircled energy	147
7.10. Objective test 1: measured MTF	147
7.11. Schematic of the PSF measurement	148
7.12. Objective test 2: measured PSF on axis	150
7.13. Objective test 2: PSF peak intensity scan	151

7.14. Objective test 2: measured PSF at the maximal longitudinal displacement	152
8.1. Chip designs	155
8.2. Optical selection	158
8.3. New laser system	159

List of Tables

3.1. 2×2 array of probed quantities	37
7.1. List of commercial microscope objectives	132
7.2. Objective: surface data	141
8.1. Thermal and electrical properties of some materials	156

List of Acronyms

1D	one dimensional
2D	two dimensional
3D	three dimensional
AC	alternating current
AlN	Aluminium Nitride
BCB	benzocyclobutene
BEC	Bose-Einstein condensate
CCD	charge coupled device
DC	direct current
DDS	direct digital synthesis
GPE	Gross-Pitaevskii equation
He, He*	helium, metastable helium
HWHM	half width at half maximum
IBG	ideal Bose gas
LDA	local density approximation
LEnsE	Laboratoire d'Enseignement Expérimental
LL	Lieb-Liniger
MG	modulated guide
MOT	magneto-optical trap
MTF	modulation transfer function
MYY	modified Yang-Yang
NA	numerical aperture
OPD	optical path difference
PMMA	Poly(methyl methacrylate)
PSF	point spread function
PSN	photon shot noise
qBEC	quasi BEC <i>or</i> quasicondensate
QMC	quantum Monte-Carlo

Rb	rubidium
RF	radio frequency
RMS	root mean square
SGPE	stochastic Gross-Pitaevski equation
Si	silicon
SiC	silicon carbide
SiO ₂	silicon oxide
SSE	stochastic serial expansion
TA	tapered amplifier
TE	transverse excited (states)
TG	Tonks-Girardeau
TOF	time of flight
UHV	ultrahigh vacuum
YY	Yang-Yang

List of Symbols

A, B, τ_1, τ_2	fit parameters in Eq. (4.27)
\mathcal{A}	'effective spring constant' in Hertzian contact
a	3D scattering length
a_{\perp}	$\equiv \sqrt{\hbar/(m\omega_{\perp})}$
α	excitation strength
α_e	parameter used in the effective scattering cross section model
$b, b(\tau)$	length scale in the scaling solutions
$\dot{b}, \dot{b}(\tau), \ddot{b}, \ddot{b}(\tau)$	first and second time derivatives of b
β_T	isothermal compressibility
C_2, C_4	second and fourth order nested commutator with H_f
\mathcal{C}	$\simeq 1.4603$ (numerical constant)
c	speed of sound
\tilde{c}	$\equiv 1/l_g$
d, \dot{d}, \ddot{d}	(linear) displacement of a pendulum and its time derivatives
det	Slater determinant
Δ_p	pixel size in momentum space
Δ_z	pixel size in real space
ΔH	change in H
δ_p	RMS size of an atomic diffusion spot in momentum-space imaging
δ_z	RMS size of an atomic diffusion spot in real-space imaging
$\delta N(z)$	$\equiv N(z) - \langle N(z) \rangle$
δz	subsystem size in Ch. 2
$\delta(z)$	Dirac delta function in z
$\langle \delta N^2 \rangle$	variance of the atom number
$\langle \delta \rho^2 \rangle$	variance of the linear density
$\langle \delta z^2 \rangle$	mean-square width of an atomic diffusion spot
E	energy
E_g	energy scale of the LL model

E_j	elastic modulus of the j th pendulum
E^*	effective elastic modulus
$\epsilon(k)$	excitation spectrum
$\tilde{\epsilon}(y)$	$\equiv \epsilon(k)/(k_B T)$
F, F'	total angular momentum quantum number of hyperfine states
f	focal length of an optical element
f_0, ω_0	value of f_z before the f_z quench
f_{Bz}, ω_{Bz}	breathing frequency in real space
f_{Bp}, ω_{Bp}	breathing frequency in momentum space
f_D, ω_D	dipole frequency
f_{MG}, ω_{MG}	frequency of the (AC) current in the modulated guide
f_{RF}, ω_{RF}	frequency of the RF field
f_{ini}, f_{fin}	<i>initial</i> and <i>final</i> RF frequency during the final evaporation
f_{kick}, ω_{kick}	frequency of the (harmonic) focusing kick potential
f_{mod}, ω_{mod}	frequency of the g_{1D} modulation
$f_p(k), f_h(k)$	quasimomentum distribution for <i>particles</i> and <i>holes</i>
f_z, ω_z	longitudinal trapping frequency
$f_{\perp}, \omega_{\perp}$	transverse trapping frequency
$\tilde{f}_p(y)$	$\equiv f_p(k)$
$\phi_j(z_k)$	j th harmonic orbital as a function of z_k
g	gravitational acceleration
g_0	value of the 1D interaction strength before any modifications
g_{1D}	1D interaction strength
$g_{1/2}(x)$	$\equiv \sum_{j=1}^{\infty} x^j / j^{1/2}$
$g_2(z, \tau_{TOF})$	two-body correlation function at expansion time $\tau = \tau_{TOF}$
$\tilde{g}_2(z, \tau_{TOF})$	resolution broadened two-body correlation function
Γ	natural line width of an atomic transition
γ	interaction parameter of the LL model
γ_0	interaction parameter corresponding to ρ_0
γ_{co}	$\equiv t^{-2/3}$
H	Hamilton operator
H_f	final Hamilton operator after the f_z quench
H_{int}	interaction part of H
H_{LL}	Hamilton operator of the LL model
H_{pot}	(external) potential part of H
h	Planck's constant

\hbar	$\equiv h/(2\pi)$
I_{MG}	current in the modulated guide
I_{pr}	intensity of the probe beam
I_{sat}	saturation intensity
K	relative power of the second harmonic of the w_p oscillations
k	wave number of the excited phonons in Ch. 6
k, k'	quasimomenta in Ch. 2
k_{B}	Boltzmann's constant
κ	reduction factor due to the imaging resolution
L	(total) system size
l	length of a pendulum
l_{D}	$\equiv \sqrt{\hbar/(m\omega_{\text{D}})}$
l_{c}	correlation length
l_{g}	length scale of the LL model
λ	wavelength
λ_{dB}	de Broglie wavelength
M	magnification of an optical system
m	mass of a particle
m_{F}	spin angular momentum quantum number of hyperfine states
m_{pend}	mass of a pendulum
μ	(1D) chemical potential
μ_0	unshifted chemical potential (at $z = 0$ in a harmonic confinement)
μ_{3D}	(3D) chemical potential
$\mu(z)$	$= \mu_0 - V(z)$
$\bar{\mu}$	$\equiv \mu_{\text{3D}}/(\hbar\omega_{\perp})$
$\tilde{\mu}$	$\equiv \mu/(k_{\text{B}}T)$
N, N_{tot}	total atom number
$N(p), N(p, \tau)$	(measured) density profile in momentum space at time τ
$N(z), N(z, \tau)$	(measured) density profile in real space at time τ
N_{TE}	population in the transverse excited states
N_{at}	atom number
$N_{\text{calib}}(z)$	(measured) atom-number calibration profile
$N_{\text{fluct}}(z)$	(measured) individual fluctuation profile
N_{ph}	photon number
$N_{\text{prof}}(z)$	(measured and normalized) mean density profile
$\langle N \rangle$	mean atom number

$n(p), n(p, \tau)$	momentum distribution at time τ
$n_{\text{TG}}(p, \tau)$	momentum distribution at time τ of a TG gas
ν_j	Poisson ratio of the j th pendulum
ν^*	effective Poisson ratio
P	pressure
p	momentum
$p_0, p_0(\tau)$	center momentum
p_c	momentum corresponding to the speed of sound
$\langle p^2 \rangle$	mean square momentum
Q_{Bz}	quality factor of the breathing oscillations in real space
R	effective radius
R_j	radius of j th pendulum
R_S	Strehl ratio
r_{PSF}	point spread function radius
ρ	linear (number) density
ρ_0	peak density (at $z = 0$ in a harmonic confinement)
$\rho(z), \rho(z, \tau)$	longitudinal density profile at time τ
$\rho_{\text{TG}}(z, \tau)$	longitudinal density profile at time τ of a TG gas
$\langle \rho \rangle$	mean linear density
S	entropy
s	$\equiv I_{\text{pr}}/I_{\text{sat}}$, saturation parameter
σ_0	scattering cross section on resonance
σ_e	effective scattering cross section
T	temperature
$T(\tau)$	temperature as a function of time τ
T_{fluct}	temperature obtained from the atom-number fluctuation thermometry
T_{prof}	temperature obtained from the density-profile thermometry
t	reduced temperature of the LL model
τ	time
τ_{Bz}	lifetime of the breathing mode in real space
τ_{TOF}	time of flight
τ_c	time constant of the final RF evaporation
τ_{coll}	collision time
τ_{evap}	duration of the final RF evaporation
τ_{kick}	duration of the focusing kick

τ_{\max}	maximal evolution time recorded
τ_{pr}	duration of the probe pulse
$U_{\text{int}}(z)$	(1D) pseudo interaction potential
$u, u(z, \tau)$	displacement field at time τ
$V(z)$	longitudinal trapping potential
$v(\tau)$	velocity of a particle
w_p	half width at half maximum of $n(p)$ or $N(p)$
ω_k	energy of a phonon with wave number k (in units of \hbar)
x	(one) transverse direction of the atomic cloud in Ch. 3, or (one) transverse direction of the PSF in Ch. 7
$\tilde{\xi}$	healing length
y	$\equiv k/\tilde{c}$ in Ch. 2, or (one) transverse direction of the point spread function in Ch. 7
$\Psi_{\text{TG}}(z_1, \dots, z_N)$	TG wave function of N impenetrable bosons
z	(longitudinal) position
$z_0, z_0(\tau)$	center position
$\langle z^2 \rangle, \langle z^2 \rangle(\tau)$	mean square distance
$\langle \rangle$	ensemble average
$\langle \rangle_T$	thermal average

Acknowledgements

This thesis has been an exciting part of my intellectual journey. Many played a significant role in making it possible and enjoyable. I would like to express my deepest gratitude to them.

First of all, the atom chip team, i.e. 'PUCE' team:

- especially Aisling, our new PhD student, who is ever so energetic, and is now becoming the true mistress of the experiment. It's a great pleasure working with you, Aisling!
- Isabelle, the boss and mommy of the experiment, ever helpful, patient, supportive, and inspirational. Thank you for your guidance, Isabelle!
- Thibaut, the PhD student on our experiment before me, from whom I learnt everything about the current setup, and ever so gentle and kind to the ignorant new comer. Thank you, Thibaut!

Tarik, Laëtitia, Aurélien, Romain, and other past members who have built and improved the setup over the years.

Our colleagues who supported our experimental studies with theory insights:

- Tommaso, a strong force in QMC simulations;
- and Giuseppe, who single handedly developed the elegant model starting from the Heisenberg equation of motion, used in our breathing mode studies.

Next comes the atom optics (Optique Atomique) group led by Chris and Alain, to which our atom-chip experiment belongs. It has been a dynamic and stimulating environment, and I learnt a lot by discussing with all of you. Many thanks to Lynn, Guillaume, Raphael, and Kilian, my fellow PhD students and batch-mates, with whom I had many beers and discussed much physics. Also, the quantum optics group just next door, from which fellow colleagues and PhD students have

become friends, and in which I have met some of the most impressive experimentalists thus far.

The various engineers and technicians from the workshops. They not only deliver excellent pieces and instruments on demand, but also have been extremely open and helpful in sharing their technical expertise. It was through the countless discussions with them that I gathered some of the most valuable technical knowledge. Special thanks goes to Patrick, André, and Christian, who helped me a great deal in the construction of the imaging objective, which is reported in Ch. 7.

The teaching department at the institute, especially LEnsE, Laboratoire Enseignement Expérimental, where I did most of my teaching. Many thanks to Lionel, Thierry, Cédric, Fabienne, Nicolas, Margaux, François, Nathalie, ...

Members of my jury, who painstakingly read through the entire manuscript and provided me with constructive and critical comments. A good fraction of them came from far to my defense, and all participated actively during the lively and uncompromising discussion after my presentation. Thank you all for your effort!

Various institutions which have made this PhD possible: Ecole Doctorale Ondes et Matière, the doctoral school that funded my thesis, Institut d'Optique Graduate School, the hosting institute where my teaching and research took place, Thales and Laboratoire de Photonique et de Nanostructure, where the atom chip is made, Centre for Quantum Technologies Singapore, which provided valuable opportunities for visits and exchanges, just to name a few...

Last but not the least, my dearest and most precious friends and family, who supported me in the ways they know the best. Thank you!

Abstract

One-dimensional quantum many-body systems exhibit peculiar and intriguing behaviors as a consequence of the reduced dimensionality, which enhances the effect of fluctuations and correlations. The high degree of isolation and controllability of experiments manipulating ultra-cold atomic gases allows for the experimental simulation of text-book models, for which many theory tools are available for quantitative comparison. In this thesis, I present instances of such efforts carried out during my PhD thesis, namely, the studies performed to investigate the behavior of 1D Bose gas (Lieb-Liniger gas) at equilibrium and beyond. An overview of the experimental setup and of the toolbox available to date to characterize the equilibrium thermodynamics of a Lieb-Liniger gas is shown, followed by detailed studies of the breathing mode of such a system, the long-lived nonequilibrium state often observed, and the system's response to strong excitations via interaction tuning. I also report the technical advances of the experiment, i.e. the new imaging objective with an improved spatial resolution, and the current state of affairs of the atom chip and the laser system.

Introduction

Physics in reduced dimensions can be very different from that in the common three dimensional (3D) world. In particular, a one-dimensional (1D) system exhibits strong intrinsic fluctuations and dynamics, and promises the possibility to realize integrable models. The theoretical understanding of 1D systems at thermal equilibrium has been fairly well established [31], enabling quantitative characterization of the experimental realization.

On the other hand, the understanding of the dynamics of an isolated quantum many-body system is of interest in both statistical physics and quantum physics. For a system brought far away from its equilibrium state, no generic frame work exists to describe when and how does the system relax, or the complex transient states exhibited. Despite significant efforts in theory [119], experimental quantum simulations [149] appear to be useful.

Ultracold atomic gases constitute a prime candidate for such investigations. The high degree of isolation and control available enables the engineering of textbook models. Also, collisions take place on a time scale accessible by the experiment, giving hopes for probing the relaxation dynamics. As a result, there have been a myriad of activities in the community of ultracold atomic gases to study nonequilibrium dynamics [34, 66, 75, 94, 100, 101, 125, 133, 149, 154].

The experiments I performed during the course of my doctoral work make use of an atom-chip setup to manipulate ultracold gases of rubidium - 87 (^{87}Rb), and are precisely centered around the theme of the equilibrium and nonequilibrium behavior of 1D systems. For the equilibrium behavior, new tools such as the momentum distribution and momentum correlations have been and are still being developed in order to quantitatively characterize the experimental system. For the nonequilibrium dynamics, various means have been used to bring the system away from equilibrium and the subsequent evolution investigated. In addition, technical improvements are made in order to ensure the relevance and versatility of the experimental set up in the long run.

This thesis is a documentation of my scientific activities from September 2011 to September 2014. It is divided into three parts. Part I introduces the toolbox developed for the quantitative characterization of our experimental system, a single tube of 1D Bose gases with repulsive contact interaction in a harmonic trap. In Part II, I present the experimental investigations aimed at probing the nonequi-

librium behavior of harmonically confined 1D Bose gases. Part III details the technical improvements of the experimental setup. A general conclusion is given at the end.

Part I.

1D Tool Box

This part aims to introduce the toolbox developed in the past years to quantitatively characterize the experimental realizations of 1D Bose gases. Such efforts have not only enhanced our understanding of the equilibrium characteristics of the system of interest, but also laid down the foundation for the study of nonequilibrium phenomena.

I organize this part as follows. Chapter 1 introduces the atom-chip setup used on our experiment to realize single samples of 1D Bose gases. The underlying Lieb-Liniger model as well as its extensions and modifications relevant to its experimental realizations are discussed in Ch. 2. I then give an overview of various tools that can be used to characterize the equilibrium behavior of single samples of 1D Bose gases in Ch. 3.

1. Atom Chip at Palaiseau

Contents

1.1. Reaching 1D regime	10
1.2. Experimental setup	11
1.3. Typical preparation sequence	17

An atom chip is a surface mounted device that miniaturizes and integrates the experimental setup for matter-wave optics, in a manner not unlike photonics to optics, or integrated circuits to conventional electrical circuits. The early activities leading to the conception of atom chips started in 1990s, when attempts were made to guide atoms along free-standing wires and trap them in simple geometries [40]. After two decades of intense development, this device not only routinely produces Bose Einstein condensate (BEC) [74], a crucial ingredient in studying macroscopic quantum phenomena, but also realizes many aspects of the early visions [51, 52]. For instance, it can investigate matter-wave optics in versatile potentials [43, 72, 122], perform interferometric measurements [37] (and reference therein), and study physics of low-dimensional systems [5, 9, 10, 19, 39, 44, 76, 83, 84, 98, 105, 141, 147, 150]. It can also integrate other devices, such as fiber optics [36], nanostructures [55, 62, 71], permanent magnetic materials [89, 136], and superconductors [16, 32, 80, 130].

The experiments performed during the course of my doctoral work make use of an atom-chip setup to manipulate ultracold gases of ^{87}Rb in highly anisotropic potentials. This ‘BEC machine’ was first constructed in the early 2000s, and underwent various stages of upgrade meanwhile. Details can be found in previous theses [11, 12, 45, 82, 137, 148]. In particular, all experiments described in this thesis are carried out using this fully functional machine, whose most recent status of affairs up to 2012 is recorded in [82].

For completeness, however, I will first discuss about the realization of 1D systems with ultracold atoms in Sec. 1.1, then give a brief description of the experimental setup in Sec. 1.2 and the typical sequence used to prepare a 1D cloud of ultracold Rb on our experiment in Sec. 1.3. A conclusion is given at the end.

1.1. Reaching 1D regime

Achieving a 1D geometry requires that the energy scales associated with both thermal excitation and change of particle number to be small compared to the transverse energy spacing, i.e.,

$$k_B T, \mu \ll \hbar f_{\perp}, \quad (1.1)$$

so that strongly prolate trapping configurations are necessary. Here, k_B is the Boltzmann constant, T is the absolute temperature, μ is the chemical potential, \hbar is the Planck's constant, and f_{\perp} is the transverse trapping frequency¹, assuming a harmonic confinement that is isotropic in the transverse direction. This is illustrated in Fig. 1.1. Typical realizations also satisfy $k_B T, \mu \gg \hbar f_z$, where f_z is the longitudinal trapping frequency, so that many longitudinal states are occupied.

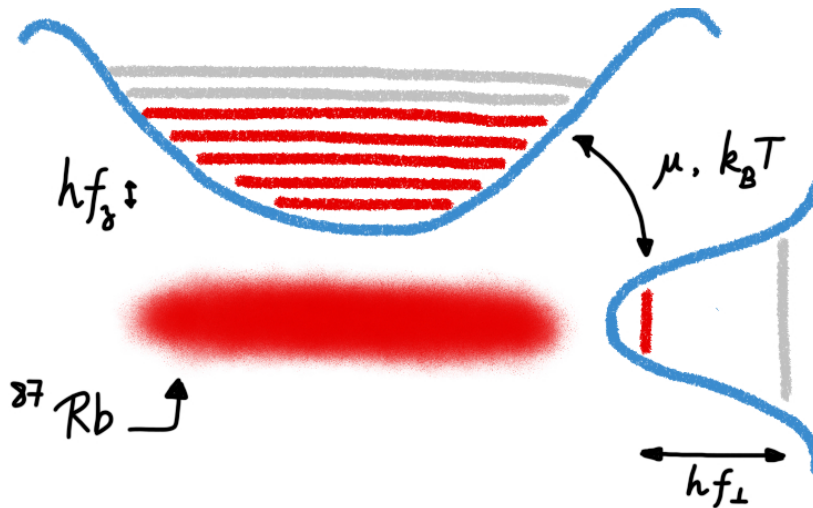


Figure 1.1.: An illustration of the 1D criterion, Eq. (1.1).

There are in general two strategies to achieve such a geometry:

¹Note that f and ω will be used interchangeably in this manuscript. Symbols with the same subscript ' γ ' are always related by $\omega_{\gamma} = 2\pi f_{\gamma}$.

1. by loading a precooled gas into an array of tubes [73, 95, 110, 153], corresponding to attaining low T , μ and increasing f_{\perp} ;
2. by starting with a relatively hot gas in a single tube and evaporating down into the 1D regime, corresponding to fixing² a high f_{\perp} and decreasing T , μ [44, 76, 150].

Both strategies have been demonstrated to be viable, though methods used for characterization depends on the choice, for each has its own advantages and disadvantages. The first method allows for the characterization of the system prior to loading the tubes using standard techniques developed earlier for 3D BEC experiments, and certain thermodynamic properties such as temperature, entropy per particle, etc. are carried over to the subsequent 1D systems by adiabaticity arguments, for which the applicability becomes unclear sometimes. This strategy also ensures ensemble averaging (over the tubes) automatically, allowing for an acceptable integrated signal in measurements even if the signal from individual tubes is low. For the latter, newer and more precise calibration schemes had to be developed, and the absence of ensemble averaging allows for novel probes such as fluctuation measurements that give direct access to a whole new range of characteristics of the system (see Ch. 3 for further discussions).

We use the second strategy on our experiment. The next section gives an overview of the setup that enables this implementation.

1.2. Experimental setup

Atom chip

The atom chip itself is the central component of the setup. The current generation is a single-layer³ chip that makes use of aluminium nitride (AlN) substrate for its excellent thermal properties [8, 53, 121]. Gold microwires are fabricated using optical lithography and physical vapor deposition. A planarization process is then employed to cover the wires with an insulating resist, forming a surface that

²with the possibility of increasing it further at a later stage.

³that is to say all wires rest on the same plane, not to be confused with various layers of material that is added to the chip during the fabrication process.

is sufficiently smooth⁴ for light at 780 nm. This surface is then coated with a thin layer of gold for high reflectivity. Details of this process are available in Ref. [11].

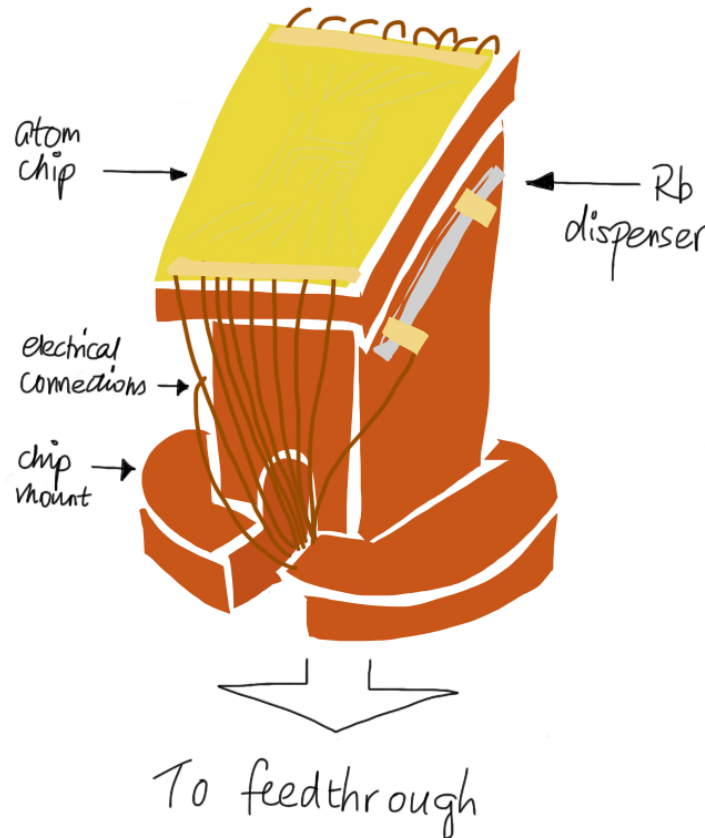


Figure 1.2.: An illustration of the mounted chip.

The chip on our setup is mounted on a copper piece that acts as a heat sink and adapter to a vacuum flange (see Fig. 1.2). In order to achieve strong magnetic confinement, high current densities in small wire structures are favorable [57], implying significant heating, which in turn results in deformation or damage of the chip structure. For a given current density, heating of the chip can be reduced by improving thermal dissipation, mostly via conduction through the substrate to the chip mount and eventually the environment. It is achieved on this experiment by soldering the AlN substrate onto the mount. Indium is used as the soldering agent for its low melting point, so that the delicate structure on the chip can be preserved. It is also compatible with an ultrahigh vacuum (UHV). Since the implementation of the soldering process in January 2012, we have qualita-

⁴Trenches due to underlying wires are below 500 nm deep.

tively observed significantly less thermal deformation of the chip⁵. We plan to perform a quantitative study of the thermal characteristics.

Using a bulk AlN wafer, as is done presently on our experiment, is however not ideal due to its grainy structure, which translates into the shape irregularities of the surface-mounted wires. The grain size depends on the manufacturing process and varies from one batch to another. Considerations of substitute materials and processes will be discussed in Ch. 8, where a vision of an improved experiment is given.

Magnetic fields

The wires on the atom chip are powered by stabilized direct current (DC) sources, which are in turn powered by batteries to minimize technical noise induced by ground loops. Surface magnetic fields produced by the wires are supplemented by those produced by external coils. Most of the power supplies in use now have been designed and constructed by an in-house electronic engineer, Mr. Frederic Moron.

Vacuum system

The vacuum system of this experiment is fairly simple and monolithic (see Fig. 1.3). It consists of a small stainless steel chamber that houses the atom chip, connected to a Titanium sublimation pump and an ion getter pump. The small total volume (~ 1 L) ensures efficient pumping and bake-out. The cold cathode vacuum gauge typically measures 4×10^{-11} mbar without the Rb dispenser in operation. Little functional changes have been made since 2004. I refer interested readers to Ref. [12, 45, 137] for details.

Laser system

The laser system used for cooling and probing the atoms is entirely home made. Two external cavity diode lasers (the Master and Repumper) at 780 nm are frequency locked 6.8 GHz apart. The Master is spectroscopically locked on the level crossing between the $|F = 2\rangle \rightarrow |F' = 2\rangle$ and $|F = 2\rangle \rightarrow |F' = 3\rangle$ transitions of the ^{87}Rb D2 line⁶, and injection locks another laser diode (the Slave). The Re-

⁵compared to previous generations where the chip was glued using an epoxy with high thermal conductivity, Epotek H77.

⁶This terminology originates from the sodium doublet (D1 and D2) in the Fraunhofer lines in

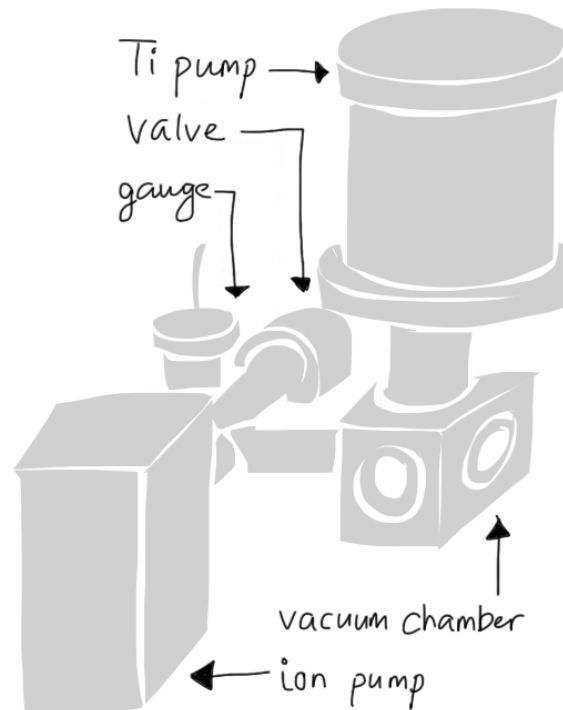


Figure 1.3.: A drawing of the essential components of the vacuum system.

pumper injects a tapered amplifier⁷ (TA). A schematic is shown in Fig. 1.4. Compared to the system presented in [82], the only addition is the TA, which amplifies the Repumper since the diode itself does not give out sufficient power⁸. This solution is certainly an overkill and temporary. A new scheme will be implemented for the next generation of experiments, in conjunction with a new chip design and more powerful imaging optics. This will be discussed again in Ch. 8.

Experimental control

Experiments manipulating ultracold atoms require precise synchronization in their control. This is achieved on our experiment by a homemade sequencer, designed and constructed by an in-house electronic engineer, Mr. André Villing, together with a control software running on Matlab 6, developed by Dr. Jérôme Estève and Dr. David Stevens. Details of the architecture can be found in [45].

the solar absorption spectrum. Both terms meanwhile are used for all alkali transitions from the ground state to the first excited state [2].

⁷Eagleyard EYP-TPA-0780-00500-3006-CMT03-0000.

⁸Eagleyard EYP-RWE-0790-04000-0750-SOT01-0000, giving barely above 10 mW before a fiber injection, compared to easily 50 mW at the same point using the TA.

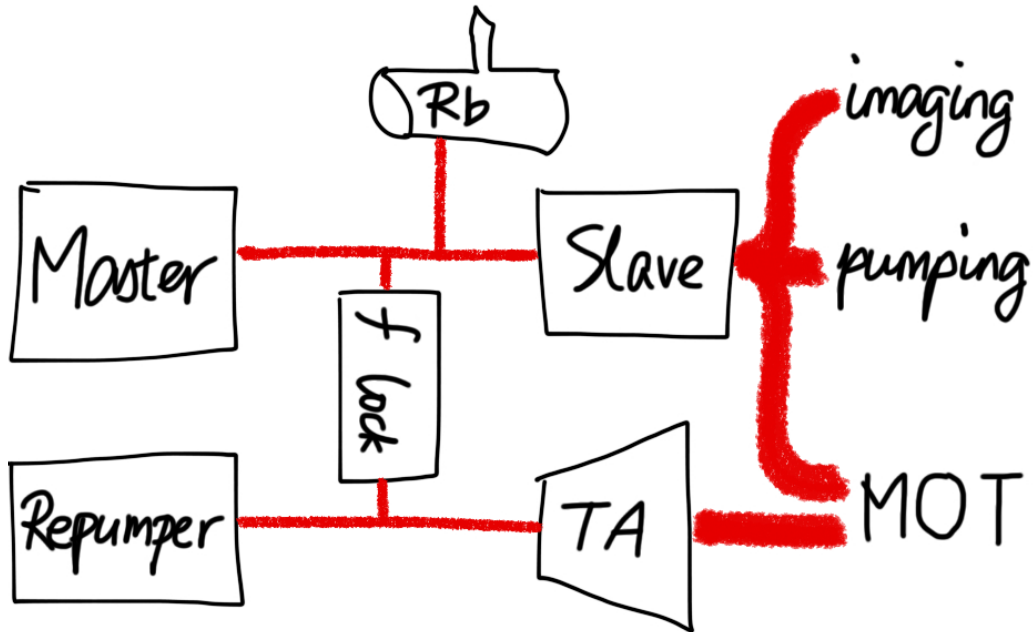


Figure 1.4.: A schematic of the current laser system.

For the purpose of book keeping, I mention below the upgrades that have taken place up to this point:

- Digital cards with 16 (instead of 8) output channels are in use, while the number of points per channel per sequence remains at 32;
- A homemade direct digital synthesis (DDS) card has been integrated. It generates a smooth oscillatory signal according to an externally specified amplitude (amplitude input) and an internally specified (programmed) frequency. The frequency reference may be external (local oscillator input) or internal (using the sequencer clock). The output signal is triggered by a digital input, and it is possible to suspend (gate input) the rest of the sequencer during its operation. This card is responsible for generating the radio frequency (RF) signal needed for evaporative cooling, and a photo is included in Fig. 1.5 as an illustration.
- The prototype of analog cards with 256 (instead of 32) points per channel per sequence is now available. The number of output channels remains 4 for the time being, but instances with 8 channels should arrive the a near future.

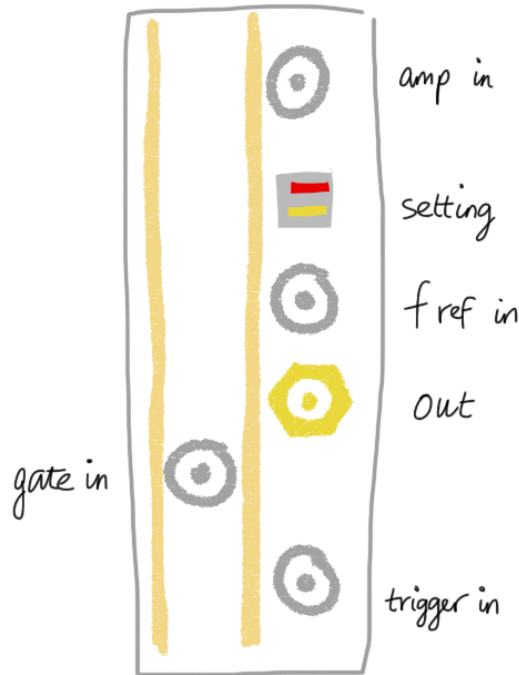


Figure 1.5.: An illustration of the front view of the DDS card with its various input/output ports.

Imaging system

The atoms are imaged on a charge-coupled-device (CCD) camera⁹. We perform a standard (destructive) absorption imaging of the atoms. A treatment according to and beyond the Beer-Lambert law can be found in [11, 45, 82, 137, 148]. The imaging system is illustrated in Fig. 1.6. It consists of a laser collimator¹⁰ (objective) in focus to infinity conjugation, and a doublet¹¹ that projects the image on the CCD chip.

Such a setup is diffraction limited with a point spread function (PSF) for which the radius of the central Airy disc $r_{\text{PSF}} = 2.4 \mu\text{m}$. A magnification of ~ 5 gives a pixel size $\Delta_z = 2.7 \mu\text{m}$. The resolution in practice limited by the atomic diffusion during the imaging pulse, and the root-mean-square (RMS) radius for typical *in situ* imaging parameters (probe pulse duration and saturation) is $\delta_z \simeq 3 \mu\text{m}$ in the object plane. Given that the signal-to-noise ratio (SNR) for detecting small num-

⁹Princeton Instruments PIXIS 1024, operating in frame-transfer mode. The quantum efficiency is $\sim 80\%$ at 780 nm.

¹⁰Melles Griot GLC-50.0-20.0-830.

¹¹Melles Griot LAO-250.0-30.0.

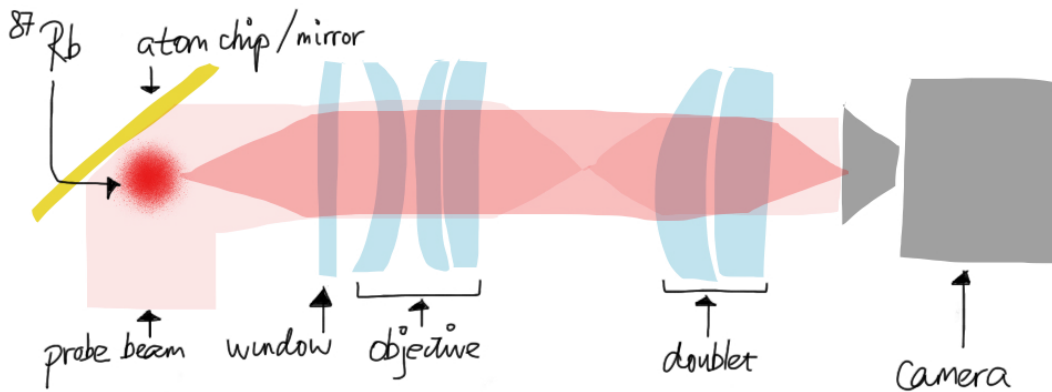


Figure 1.6.: An illustration of the current imaging system.

ber of atoms improves with better resolution (see Sec. 7.1.1), there is an interest in installing an imaging objective with a larger numerical aperture (NA). To take advantage of the expertise in optics available at Institut d'Optique, I carried out the design, assembly, and preliminary characterization in house¹², with the help of various people from the institute, including but not limited to Dr. Yvan Sortais, Mr. André Guilbaud, the staff at the mechanical workshop, and Mr. Lionel Jacubowicz. Ch. 7 acts as a documentation of the new objective.

1.3. Typical preparation sequence

Since the first realization of BEC in 1995 [6, 20, 38], the field of ultracold atomic gases has been growing rapidly, with an abundance of collaborative efforts and synergy. As a result, procedures to cool and trap ^{87}Rb , by far the most common candidate in such experiments, have become a fairly standard operation procedure, with small variations¹³ from one experiment to another. Even the complication of limited optical access due to the atom chip has been satisfactorily overcome [57, 77].

¹²Only the production of the optics were out-sourced to Lens Optics (URL: <http://www.lens-optics.de/>).

¹³in terms of the implementation of the same strategy. Of course, different strategies may be available to achieve the same purpose, and would require corresponding implementations. For instance, the loading of a magneto-optical trap (MOT) can be carried out via constant background pressure, modulated background pressure, a two-dimensional (2D) MOT, or a Zeeman slower, with increasing efficiency. Implementation of each of these strategies is well established.

This experiment takes advantage of the experience gathered in the community, and implements the following steps in order to produce cold samples of 1D quantum gases:

- An external¹⁴ mirror¹⁵ magneto-optical trap (mirror MOT) loads $\sim 10^8$ atoms and cools them down to $\sim 200 \mu\text{K}$ at a few mm from the chip surface [see Fig. 1.7(a)];
- The atoms are then transferred to a surface¹⁶ MOT $\sim 200 \mu\text{m}$ from the chip and compressed [see Fig. 1.7(b)];
- The optical molasses cool $\sim 10^7$ atoms down to $\sim 10 \mu\text{K}$ [see Fig. 1.7(c) for a mock-up of the image registered on the camera];
- The atoms are optically pumped into the $|F = 2, m_F = 2\rangle$ state [see Fig. 1.7(d) for an illustration];
- A magnetic trap provided by H-shaped wires and an external bias field is loaded with $\sim 5 \times 10^6$ atoms at several hundred μm from the chip. The atomic cloud is then compressed transversely into a prolate trap provided by a Z-shaped wire and an external bias field [see Fig. 1.7(e)];
- Radio-frequency evaporation is carried out for 2.4 s to yield $\sim 3 \times 10^5$ atoms at $\sim 1 \mu\text{K}$ [see Fig. 1.7(f)];
- $\sim 8 \times 10^4$ atoms are then transferred to the alternating-current (AC) magnetic trap $\sim 4 \mu\text{m}$ from the chip, and a second RF evaporation produces the final sample of $500\text{-}10^4$ atoms at $20\text{-}200 \text{ nK}$ [see Fig. 1.7(g) and (h)].

Only the final step above is particular to our setup due to the finite depth of the AC magnetic trap. Details can be found in Ref. [82]. By tuning the parameters of this final cooling stage, we can achieve a range of values for the temperature as well as the total number of atoms. In addition, the transverse trapping frequency can be tuned in order to change the strength of the repulsive interaction¹⁷, so that

¹⁴The magnetic field is provided by the coils outside the vacuum chamber, as opposed to the on-chip wires.

¹⁵The chip surface.

¹⁶The magnetic field is generated by on-chip wires.

¹⁷See Sec. 2.2.1 and references therein for further discussions.

different thermodynamic regimes¹⁸ can be probed.

The atomic ensemble obtained at the end of the steps outlined above is then the starting point of all experiments performed in this thesis. Unless specified otherwise, this preparation stage will not be repeated in the experimental sequences discussed later.

Conclusions

In this chapter, we have seen that different strategies can be used to experimentally achieve a 1D scenario. Our atom-chip setup works with ^{87}Rb atoms that are loaded and cooled in a highly anisotropic magnetic trap, so that a single sample of 1D Bose gas can be obtained at the end of the preparation sequence.

¹⁸discussed in Sec. 2.1.3.

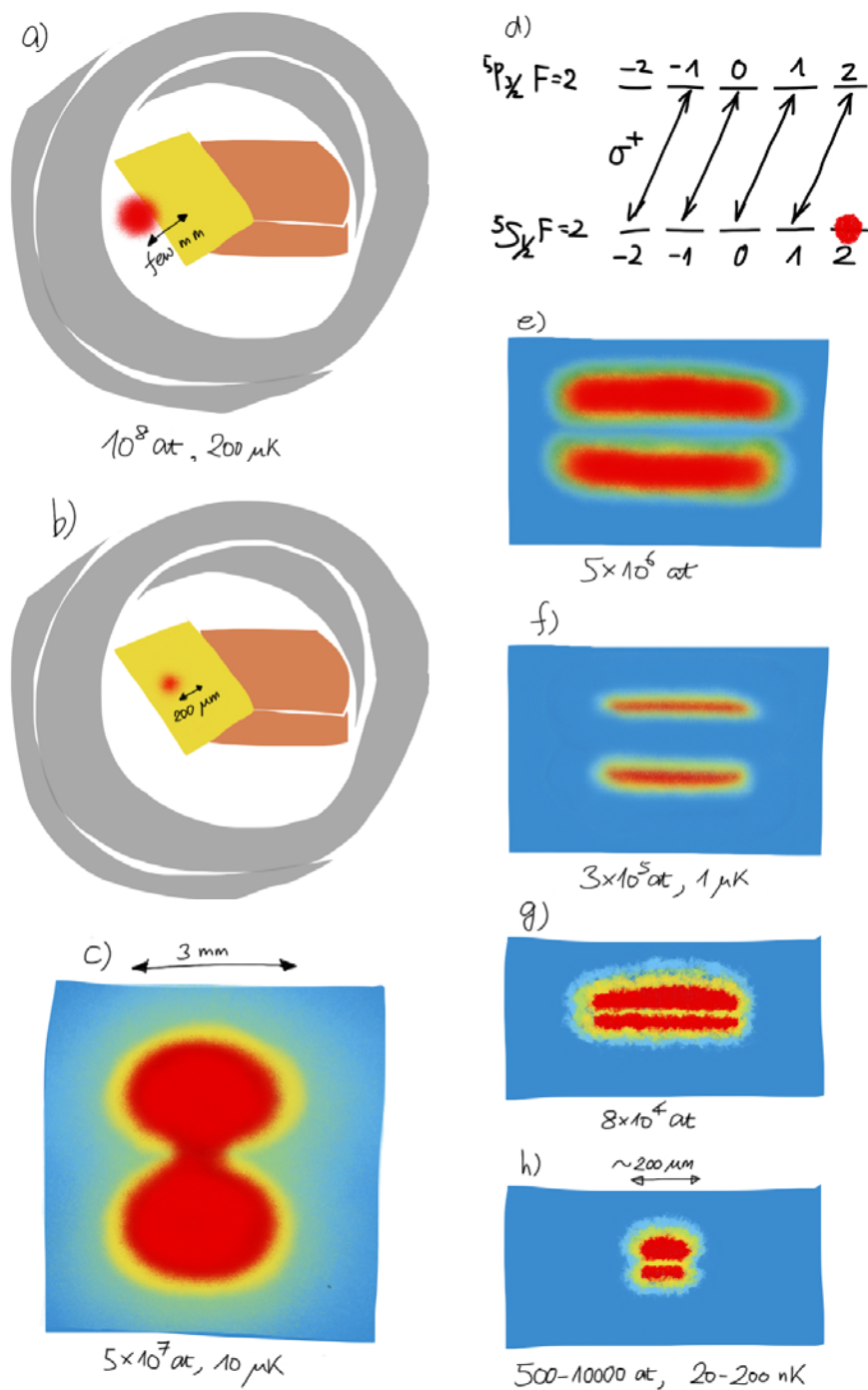


Figure 1.7.: Various stages of the preparation sequence. a) and b) are illustrations of the view from the spy camera, allowing visual inspections of MOT loading. d) is an illustration of the optical pumping scheme. c) and e) to f) are mock-ups of the images captured by the camera at various stages: optical molasses, static magnetic trap before and after the evaporation, and modulated guide before and after the evaporation. These images display both the atomic ensemble and its reflection in the chip-mirror.

2. Theory Overview

Contents

2.1. 1D Bose gas in a continuum	22
2.1.1. Lieb-Liniger model	22
2.1.2. Exact thermodynamics	23
2.1.3. 1D phase diagram	27
2.1.4. Beyond equation of state	28
2.2. 1D Bose gases in real life	29
2.2.1. Transverse trapping	29
2.2.2. Longitudinal trapping	31

This chapter will give an overview of the theoretical foundation necessary for the characterization of 1D Bose gases at thermal equilibrium. Its purpose is to set the stage for Ch. 3, which will demonstrate direct comparisons between theory results and experimental data that yield important information about the experimental systems.

Since the main focus of our discussion will be single tubes of 1D (or nearly 1D) Bose gas in harmonic confinement, I will restrict the discussion to exclude Bose gases in dimensions higher than one, for which a vast literature is available elsewhere, see e.g. [15] and references therein. Also, I will not discuss about lattice models, nor provide an exhaustive list of all theory tools available to describe the continuum case. Interested readers should look into a recent review by Cazalilla *et al* [29] and references therein in order to gain better insights of the matter.

Therefore, I organize this chapter as follows. In Sec. 2.1, I will introduce the Lieb-Liniger model and its finite temperature equation of state with a few notes concerning the computation. Different regions of the interaction-temperature phase

diagram are briefly discussed. In Sec. 2.2, a connection between the 1D homogeneous model and its experimental realization is established, accounting for both the transverse and longitudinal confinement typical of ultracold atomic experiments.

2.1. 1D Bose gas in a continuum

2.1.1. Lieb-Liniger model

Bosonic particles interacting via a Dirac-delta potential of finite strength in 1D can be described by the Lieb-Liniger (LL) model [102, 103]. It was in fact inspired by Girardeau's impenetrable boson model [64], also known as the Tonks-Girardeau (TG) gas or hard-core bosons so to speak, which takes the limit of infinite interaction strength, and is therefore essentially a zero-parameter model¹. By the introduction of a finite interaction strength g_{1D} , the LL model acquires an intrinsic length scale, corresponding to, very loosely speaking, the interparticle distance for which the interaction and kinetic energy per particle become comparable. More precisely, given the Hamilton operator

$$H_{LL} = \sum_j \frac{p_j^2}{2m} + g_{1D} \sum_{j < k} \delta(z_j - z_k), \quad (2.1)$$

where m is the particle mass, z_j and p_j are the position and momentum of the j th particle, the relevant length scale is given by

$$l_g = \frac{\hbar^2}{mg_{1D}}, \quad (2.2)$$

and the corresponding energy scale is

$$E_g = \frac{mg_{1D}^2}{2\hbar^2}, \quad (2.3)$$

where $\hbar = h/(2\pi)$.

¹Despite its peculiarity, the TG model serves as an instructive example of a strongly interacting system. More on this matter in Ch. 4.

With these scales in mind, we need two dimensionless intensive variables in order to describe a LL gas at thermal equilibrium: the interaction parameter,

$$\gamma = \frac{1}{\rho l_g} = \frac{mg_{1D}}{\hbar^2 \rho}, \quad (2.4)$$

where ρ is the linear (number) density, and the reduced temperature,

$$t = \frac{k_B T}{E_g} = \frac{2\hbar^2 k_B T}{mg_{1D}^2}. \quad (2.5)$$

The former was already introduced in the original paper by Lieb and Liniger [103], where the authors focused on the *ground state* of the model. In particular, it was shown that the Bethe Ansatz² can be applied to construct the ground-state many-body wave function, from which properties of the system can be computed numerically. Although the knowledge of the wave function in principle warrants the computation of arbitrary observables, their practical implementation differ in complexity and efficiency [59, 96, 97]. In the thermodynamic limit, where both the particle number N and the size of the system L approach infinity, while preserving the linear density ρ ($\equiv N/L$), the ground-state properties such as the energy per particle, chemical potential, etc. can be computed via the quasimomentum distribution, which is a solution of an integral equation of the Fredholm type [3]. For the exact procedures of such computation, I refer the interested reader to the original manuscript by Lieb and Liniger [103], where the authors meticulously detailed the solution.

2.1.2. Exact thermodynamics

The finite-temperature case was fully worked out a few years later, when Yang and Yang (YY) established the fact that *all* states of the LL model can be given by the Bethe Ansatz [155]. In the thermodynamic limit, the minimization of the free energy and the continuity of the many-body wave function at particle contact yield two integral equations for the quasimomentum distribution of the particles and holes, from which the equation of state can be evaluated.

²which is a prescription to construct the eigenstates (with their respective wave function and energy) of a certain class of quantum many-body problems. See e.g. Refs. [90–92] for an introduction.

As I will show in Ch. 3, the *finite-temperature* equation of state is a powerful tool to characterize experimental realizations of the LL model. However, direct application has only been reported in a few experimental setups [9, 150, 153], and neither the equation of state as numerical database nor a routine to perform such calculations has been openly accessible. I have so far constructed a set of functional programmes, and it is my intention to make it available to the public once the documentation is complete³. Meanwhile, I outline the key equations necessary for the computation, and list a few tips about its numerical implementation. It is mostly summarized from my own experience as well as many stimulating discussions with Dr. Giuseppe Carleo⁴, who has supplied some of the numerical data for the computation used in Ch. 4.

Key equations

Consider the quasimomentum⁵ distribution for the particles $f_p(k)$ and the holes $f_h(k)$, which are related via the excitation spectrum $\epsilon(k)$, defined by

$$\frac{f_h(k)}{f_p(k)} = e^{\frac{\epsilon(k)}{k_B T}}. \quad (2.6)$$

Minimization of the free energy⁶ gives

$$\epsilon(k) = -\mu + \frac{\hbar^2 k^2}{2m} - \frac{k_B T}{2\pi} \int_{-\infty}^{\infty} dk' \frac{2\tilde{c}}{\tilde{c}^2 + (k - k')^2} \ln \left(1 + e^{\frac{\epsilon(k')}{k_B T}} \right), \quad (2.7)$$

where $\tilde{c} = 1/l_g = mg_{1D}/\hbar^2$ is the interaction strength in the same dimension as the quasimomentum⁷ k , μ is the Lagrange multiplier of the constraint that preserves the linear density, and has the physical meaning of the chemical potential,

³Such a task however does not take precedence over the writing of the current manuscript, and would most likely make a nice summer project once the thesis is submitted.

⁴Laboratoire Charles Fabry, Institut d'Optique, CNRS, Université Paris Sud 11, 2 Avenue Augustin Fresnel, F-91127 Palaiseau Cedex, France.

⁵The k 's are *quasimomenta* since they are used to construct a many-body wave function in a restricted coordinate space, and have multiplicity with period $2\pi/L$, where L is the system size, so that their physical meaning differs from the true momenta p 's. A more detailed discussion can be found in [103]. In the literatures dealing with Bethe Ansatz, the k 's are known as rapidities.

⁶The derivation of this result can be found in the original paper of Yang and Yang [155].

⁷The notation of c appeared in the early papers [102, 103, 155] where the authors implicitly worked with dimensionless variables. The use of c remains convenient in the context of the integral equations discussed here, and its relation with g_{1D} establishes the connection with physical units [93].

while the particle quasimomentum distribution is given by

$$2\pi f_p(k) \left(1 + e^{\frac{\epsilon(k)}{k_B T}}\right) = 1 + \int_{-\infty}^{\infty} dk' \frac{2\tilde{c}}{\tilde{c}^2 + (k - k')^2} f_p(k'). \quad (2.8)$$

For the ease of numerical routines, it is convenient to work with dimensionless intensive quantities. Let us introduce

$$y \equiv \frac{k}{\tilde{c}}, \quad \tilde{\mu} \equiv \frac{\mu}{k_B T}, \quad \tilde{\epsilon}(y) \equiv \frac{\epsilon(k)}{k_B T}, \quad \tilde{f}_p(y) \equiv f_p(k), \quad (2.9)$$

and re-write Eqs. (2.7) and (2.8) as

$$\tilde{\epsilon}(y) = -\tilde{\mu} + \frac{y^2}{t} - \frac{1}{\pi} \int_{-\infty}^{\infty} \frac{dy'}{1 + (y - y')^2} \ln(1 + e^{\tilde{\epsilon}(y')}), \quad (2.10)$$

$$\tilde{f}_p(y) = \frac{1}{2\pi(1 + e^{\tilde{\epsilon}(y)})} \left(1 + 2 \int_{-\infty}^{\infty} \frac{dy'}{1 + (y - y')^2} \tilde{f}_p(y')\right), \quad (2.11)$$

where t is defined in Eq. (2.5). These equations can be solved iteratively as proven in [155], so that the linear density ρ , total energy E , entropy S , and pressure P can be computed using

$$(\rho l_g =) \frac{1}{\gamma} = \int_{-\infty}^{\infty} dy \tilde{f}_p(y), \quad (2.12)$$

$$\frac{E}{N k_B T} = \frac{\gamma}{t} \int_{-\infty}^{\infty} dy y^2 \tilde{f}_p(y), \quad (2.13)$$

$$\frac{S}{N} = \gamma \int_{-\infty}^{\infty} dy \tilde{f}_p(y) \left(e^{\tilde{\epsilon}(y)} \ln(1 + e^{-\tilde{\epsilon}(y)}) + \tilde{\epsilon}(y) \right), \quad (2.14)$$

$$\frac{P}{\rho k_B T} = \frac{\gamma}{2\pi} \int_{-\infty}^{\infty} dy \ln(1 + e^{-\tilde{\epsilon}(y)}). \quad (2.15)$$

Programme

Therefore, the programme that computes the YY equation of state consists of the following steps:

1. For each given pair of $(t, \tilde{\mu})$, solve iteratively Eq. (2.10) to obtain $\tilde{\epsilon}(y)$;
2. Substitute $\tilde{\epsilon}(y)$ into Eq. (2.11) and solve iteratively for $\tilde{f}_p(y)$;

3. Compute the thermodynamic quantities using Eqs. (2.12) - (2.15).

Given the iterative nature of the solutions, it is computationally economical to obtain them as numerical lists covering a substantial region in the parameter space of (γ, t) once, and use these lists as the basis of interpolation later. Since the analyticity is proven by Yang and Yang [155], the derivative of the equation of state can be evaluated to yield further information about the system, e.g. the isothermal compressibility β_T can be evaluated via $\beta_T = \left. \frac{1}{\rho} \frac{\partial \rho}{\partial p} \right|_T$, etc.

Tips for computation

Before concluding on this subsection, however, a few remarks regarding the practical implementation of the above is in order.

First, the logarithmic term in the integral of Eq. (2.10) gives a relatively large contribution for $\tilde{\epsilon}(y) > 0$, which happens for $\tilde{\mu} \gtrsim 0$. This prevents fast convergence of the iteration if one starts from the 0th order approximation $\tilde{\epsilon}_0(y) = -\tilde{\mu} + y^2/t$. To circumvent this problem, one may use an adaptive approach to choose the starting point of the iteration. Namely, for a given t , sort the list of $\{\tilde{\mu}_j\}$ of interest in increasing order, such that

$$\tilde{\mu}_1 < \tilde{\mu}_2 < \dots < \tilde{\mu}_j < \tilde{\mu}_{j+1} < \dots \quad (2.16)$$

Starting from the most negative⁸ $\tilde{\mu} = \tilde{\mu}_1 < 0$, where the 0th order approximation warrants a fairly fast convergence, the solution $\tilde{\epsilon}(y)$ for $\tilde{\mu} = \tilde{\mu}_j$ can then be used as the starting point of the iteration for $\tilde{\mu} = \tilde{\mu}_{j+1}$.

Second, to approximate the integrals in Eqs. (2.10) and (2.11), an appropriate grid of y should be chosen. Two cases exist:

Case 1: $\tilde{\mu} < 0$. Here, the step size should be chosen such that there are enough points to sample both the Lorentzian $1/(1 + (y - y')^2)$ of unity half width at half maximum (HWHM), and the Gaussian $\exp(-y^2/t)$ of width $\propto \sqrt{t}$ (from the 0th order approximation), while the range of relevant y is essentially cut off by the Gaussian-like tail of $\exp(\tilde{\epsilon}(y))$ that is present in both Eqs. (2.10) and (2.11), so that sampling up to $\sim 3\sqrt{t}$ suffices.

⁸ $\tilde{\mu} < 0$ is necessary in order to probe the regime where γ is large.

Case 2: $\tilde{\mu} \gtrsim 0$. $\tilde{\epsilon}(y)$ is negative for small $|y|$ up to $\sim \sqrt{t\tilde{\mu}}$, and it is essential to sample up to values of $|y|$ such that $\tilde{\epsilon}(y)$ is sufficiently positive. The step size, on the other hand, is imposed by the condition that there are enough samples in both the negative region of $\tilde{\epsilon}(y)$ and the Lorentzian kernel.

Hence, as one adapts the starting $\tilde{\epsilon}(y)$, the grid should be updated (expanded assuming increasing values of $\tilde{\mu}$) accordingly in order to ensure that the correct result is obtained.

2.1.3. 1D phase diagram

Now we are in the position to discuss different regions in the parameter space of (γ, t) for homogeneous systems, as illustrated in Fig. 2.1.

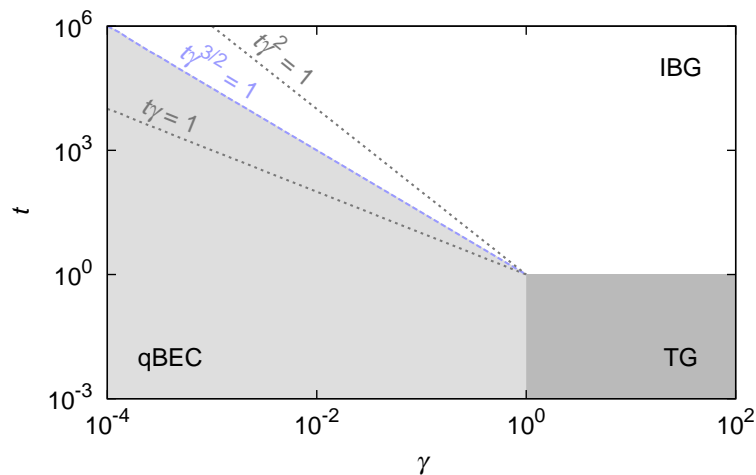


Figure 2.1.: Phase diagram of the Lieb-Liniger gas, spanned by the dimensionless interaction parameter γ and the reduced temperature t . All lines are to be understood as smooth crossover from one asymptotic regime to another.

Three asymptotic regions exist. The strongly interacting regime (dark grey area, bottom right in Fig. 2.1), marked by TG *à la* Tonks-Girardeau, is the region in the phase diagram where the typical energy of the particles is smaller than E_g . This takes place when $t \ll 1$ and $\gamma \gg 1$.

The rest of the phase diagram is subdivided into the quasicondensate (qBEC) regime (light grey area, bottom left in Fig. 2.1) and the ideal Bose gas (IBG) regime (white area, top right in Fig. 2.1).

The qBEC regime is characterized by weak and yet significant interparticle interactions such that the system is coherent with respect to two-body correlations (suppressed density fluctuations) and incoherent with respect to one-body correlations (surviving phase fluctuations). Two subregimes can be identified: the quantum coherent qBEC ($t\gamma \ll 1$) for which quantum fluctuations dominates, and the thermal qBEC ($t\gamma \gtrsim 1$) where thermal fluctuation dominates. The boundary in between takes place around $t\gamma \simeq 1$ (grey dotted line on the left).

The IBG regime can be described by the ideal gas law with Bose-Einstein statistics, and approximated by the Maxwell-Boltzmann equation of state for sufficiently high temperature and low density. Quantum degeneracy is reached when the de Broglie wavelength of the particles becomes comparable to the interparticle distance, corresponding to $t\gamma^2 \simeq 1$ (grey dotted line on the right). This degeneracy crossover, relevant for large t , separates the degenerate ($t\gamma^2 \lesssim 1$) and nondegenerate ($t\gamma^2 \gg 1$) IBG.

The transition between the qBEC and IBG regimes, known as the quasicondensation crossover, takes place when the interaction starts to play an important role in two-body correlation, while the system remains dominated by thermal excitations and fluctuations. In terms of the dimensionless parameters, this corresponds to $t\gamma^{3/2} \simeq 1$, shown as the blue dashed line in Fig. 2.1.

Note that these boundaries are smooth crossovers and one does not find order parameters that undergo abrupt changes that are characteristic of a phase transition. Further details of the discussion above can be found in [19].

Given that our experimental setup is capable of producing samples of nearly 1D Bose gases, the thermodynamic regimes probed by the samples used for the experiments will be illustrated in such a phase diagram whenever possible.

2.1.4. Beyond equation of state

Finally, we remark that despite the elegance and universal applicability in the entire phase diagram of the YY thermodynamics, not all quantities of interest can be computed in a straight forward manner by this method. Instead, special tech-

niques valid in one or another asymptotic limit become handy depending on the regime of interest. For instance, bosonization is a powerful method to describe low-energy excitations; computational methods such as the density matrix renormalization group and quantum Monte-Carlo (QMC) techniques can be used to numerically simulate the system, *albeit* at a substantial computational cost. As it is not the purpose of this section to review all available theory tools to treat 1D Bose gas, I refer interested readers to a recent review [30] which discusses the subject matter in great eloquence and detail.

2.2. 1D Bose gases in real life

As mentioned in Sec. 1.1, a 1D system is realized in ultracold-atom experiments by trapping gaseous atoms in an elongated confinement, so that the effects of both transverse and longitudinal trapping need to be understood and taken into account.

2.2.1. Transverse trapping

The transverse confinement has essentially two effects on the system: the modification of the effective interaction strength, and the population of the transverse excited states.

Olshanii treated the problem of atomic scattering in a wave guide in his seminal work [113], which concludes that in the low-energy scattering regime, relevant to experiments using ultracold atomic gases, the presence of a confining wave guide essentially modifies the strength of the zero-range (pseudo) interaction potential that can be written as

$$U_{\text{int}}(z) = g_{1\text{D}}\delta(z), \quad (2.17)$$

where the 1D interaction strength $g_{1\text{D}}$ is related to the 3D s-wave scattering length a by

$$g_{1\text{D}} = \frac{2\hbar^2 a}{ma_{\perp}^2} \left(1 - C \frac{a}{a_{\perp}}\right)^{-1}. \quad (2.18)$$

Here, $C \simeq 1.4603\dots$, and $a_{\perp} = \sqrt{\frac{\hbar}{m\omega_{\perp}}}$ is the harmonic length scale associated with the transverse confinement $\omega_{\perp} = 2\pi f_{\perp}$.

Since we work with ^{87}Rb in the $|F = 2, m_F = 2\rangle$ hyperfine ground state, we have $a = 5.238(1)$ nm [140], and we realize a typical transverse trapping frequency in the range of several to tens of kHz, so that $a_{\perp} \sim 10^2$ nm, and $a \ll a_{\perp}$. Eq. (2.18) can then be approximated by

$$g_{1D} \simeq 2\hbar\omega_{\perp}a. \quad (2.19)$$

This formula will be used throughout the data treatment in this thesis.

Transverse excited states are relevant in most experiments that realize a single sample of 1D Bose gas. In the qBEC regime at low temperature, i.e. $k_B T \ll \hbar\omega_{\perp}$, this amounts to the so called ‘transverse swelling’, in the sense that when the 3D density is integrated over the transverse directions, the resulting linear density ρ obeys a modified equation of state [58, 60],

$$\frac{\mu}{\hbar\omega_{\perp}} = \sqrt{1 + 4\rho a} - 1, \quad (2.20)$$

instead of the usual $\mu = \rho g_{1D}$, which is the low density limit of Eq. (2.20) with g_{1D} given by Eq. (2.19), and is in good agreement with the YY equation of state in this regime. For the purpose of disambiguation, I mention in passing that μ consistently denotes the 1D chemical potential in this thesis, hence the shift by $\hbar\omega_{\perp}$ in Eq. (2.20), corresponding to the ground-state harmonic oscillator energy in the transverse directions. Literature such as [60] often deals with the 3D chemical potential, for which the qBEC equation of state reads $\mu_{3D} = \hbar\omega_{\perp}\sqrt{1 + 4\rho a}$.

For temperatures on the order of transverse trapping frequency, i.e. $k_B T \simeq \hbar\omega_{\perp}$, the system is in the 1D-3D dimension crossover. One may then treat the transverse ground state using the YY equation of state $\rho_{YY}(\mu, T)$, and the excited states as an ideal Bose gas with shifted chemical potential, i.e. for the j th excited state, the chemical potential is given by

$$\mu(j) = \mu - j\hbar\omega_{\perp}, \quad (2.21)$$

and the corresponding equation of state is

$$\rho_{\text{TE}}(\mu(j), T) = \frac{1}{\lambda_{\text{dB}}} g_{\frac{1}{2}}\left(e^{\frac{\mu(j)}{k_{\text{B}}T}}\right), \quad (2.22)$$

where $\lambda_{\text{dB}} = \sqrt{\frac{2\pi\hbar^2}{mk_{\text{B}}T}}$ is the de Broglie wave length, $g_{\frac{1}{2}}(x) = \sum_{j=1}^{\infty} x^j/j^{1/2}$ is the Bose-Einstein function [150], so that the total linear density is given by

$$\rho(\mu, T) = \rho_{\text{YY}}(\mu, T) + \sum_{j=1}^{\infty} (j+1) \rho_{\text{TE}}(\mu(j), T). \quad (2.23)$$

This is the so called *modified* Yang-Yang (MYY) equation of state, pioneered by van Amerongen *et al* [150], and has been instrumental in characterizing cold atomic samples in the relevant parameter regime [9, 39].

2.2.2. Longitudinal trapping

In a spirit not unlike the modified Yang-Yang formalism above, the longitudinal inhomogeneity may also be accounted for by appropriately shifting the chemical potential. Typically, the confinement in the longitudinal direction is considered harmonic, i.e. $V(z) = \frac{1}{2}m\omega_z^2 z^2$. Depending on the value of the frequency ω_z and the total atom number N , the quantization of the energy levels may or may not need to be taken into account [118].

However, in order to make use of results obtained for homogeneous systems such as the YY equation of state, it is crucial to stay within the framework of *quasiuniform* approximation [93], so that the entire system can be seen as a composition of subsystems that are *locally* homogeneous, and in thermal equilibrium with each other, and there is a single value of the chemical potential for the entire system. This loosely translates into the condition that the characteristic short-range correlation length l_c should be small compared to the size of the subsystem δz , which is in turn smaller than the size of the entire system L , i.e.

$$l_c \ll \delta z \ll L. \quad (2.24)$$

The choice of l_c (density correlation length or phase correlation length) depends on the observable of interest, while ω_z determines the typical length scale over

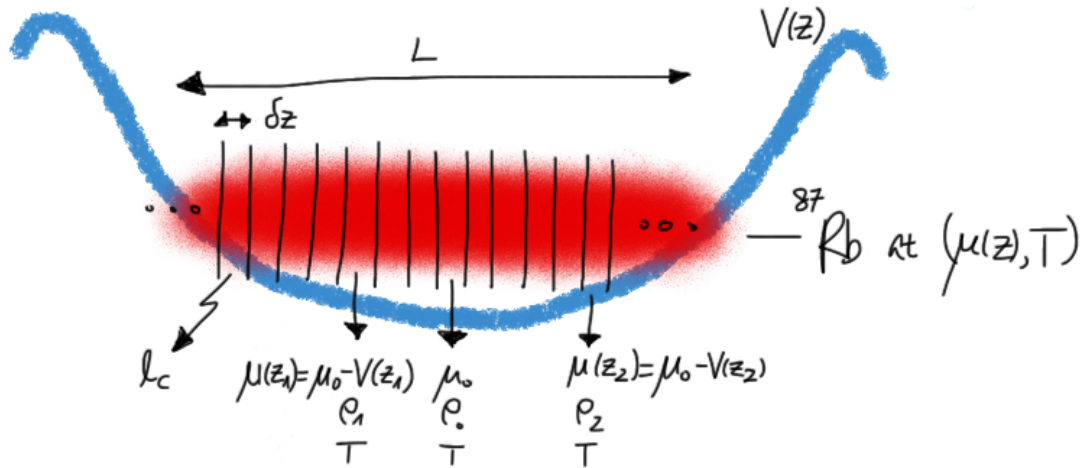


Figure 2.2.: Illustration of LDA. Each realization of a trapped 1D Bose gas can be approximated as a composition of locally homogeneous subsystems at a shifted chemical potential $\mu(z) = \mu_0 - V(z)$, and in thermal equilibrium with each other at temperature T . Such an approximation is valid if the relevant correlation length l_c , the subsystem size δz , and the total system size L satisfies $l_c \ll \delta z \ll L$.

which the density varies, and thus controls δz and L . Depending on the thermodynamic regime, one may derive explicit expressions that bound ω_z [18, 93, 118], all with the common message that the longitudinal trap has to be sufficiently weak in order for the sample to be *quasiuniform*, as one would intuitively expect, so that the local density approximation (LDA),

$$\mu(z) = \mu_0 - V(z) = \mu_0 - \frac{1}{2}m\omega_z^2 z^2, \quad (2.25)$$

correctly yields the local chemical potential at position z . Note that $\mu_0 \equiv \mu(z = 0)$ denotes the central (unshifted) chemical potential.

Consequently, each experimental realization of a trapped 1D Bose gas in fact probes different values of densities, allowing the verification of a finite range of the equation of state with a single sample.

Conclusions

In this chapter, we have seen that 1D Bose gases with repulsive contact interactions is a prototypical example of the Lieb-Liniger model, which constitutes perhaps the only known example where a unified description from weak to strong interaction is available. Plenty of theoretical tools are available, enabling quantitative characterizations.

On the other hand, the experimental realization of such a model with ultracold atomic gases requires a proper treatment of the confining potentials. The transverse confinement induces an effective interaction strength, and the population in the transverse excited states can be taken into account to a certain extent. The longitudinal confinement calls for the local density approximation, and therefore gives access to the homogeneous equation of state for various values of the local linear density simultaneously.

3. Tools in the Box

Contents

3.1. Absorption imaging	38
3.2. In real space	38
3.2.1. Mean density profile	39
3.2.2. Atom-number fluctuations	41
3.2.3. Density ripples	45
3.3. In momentum space	48
3.3.1. Momentum distribution	50
3.3.2. Momentum correlations	52

This chapter surveys a number of tools intended for quantitative characterization of 1D Bose gases developed over the past few years. It is by no means an exhaustive list, and the selection is simply based on its direct applicability to our experimental setup. Each ‘tool’ constitutes a particular kind of experimental measurement and its corresponding analysis, and independently characterizes the experimental system to yield information about the thermodynamics of the system, such as the temperature T and central chemical potential μ_0 . In our studies of nonequilibrium dynamics of 1D Bose gases discussed in the later part of this thesis, this tool box has been the workhorse to characterize the system before it is perturbed.

In experiments dealing with ultracold atomic gases, it is common to derive the information of the system from images of the atomic density distribution¹, which is related to the spatial density distribution at the time when the image is taken. Integration along the line of sight of the camera is inevitable in this case, and

¹Imaging methods may differ, but the resulting density distribution can be analyzed in a similar manner.

should be properly accounted for during data treatment. For an ideal 1D system which does not possess transverse degrees of freedom, fortunately, the line of sight can be placed perpendicular to the system, so that the integration due to imaging does not alter the density distribution along the (longitudinal) direction of interest, denoted by z in this thesis. In fact, the resulting 2D image (see Fig. 3.1 top) should be further integrated along the remaining transverse direction to yield a *linear* density distribution (see Fig. 3.1 bottom) that can be compared directly with theory, i.e.,

$$N_{\text{at}}(z) = \sum_x N_{\text{at}}(x, z), \quad (3.1)$$

where $N_{\text{at}}(z)$ denotes the atom number in a pixel at position z , and $N_{\text{at}}(x, z)$ denotes that at position (x, z) in a 2D image. Note that the density distributions in this thesis will always be those after transverse integration unless specified otherwise, so that only one spatial variable (denoted by z) is relevant.

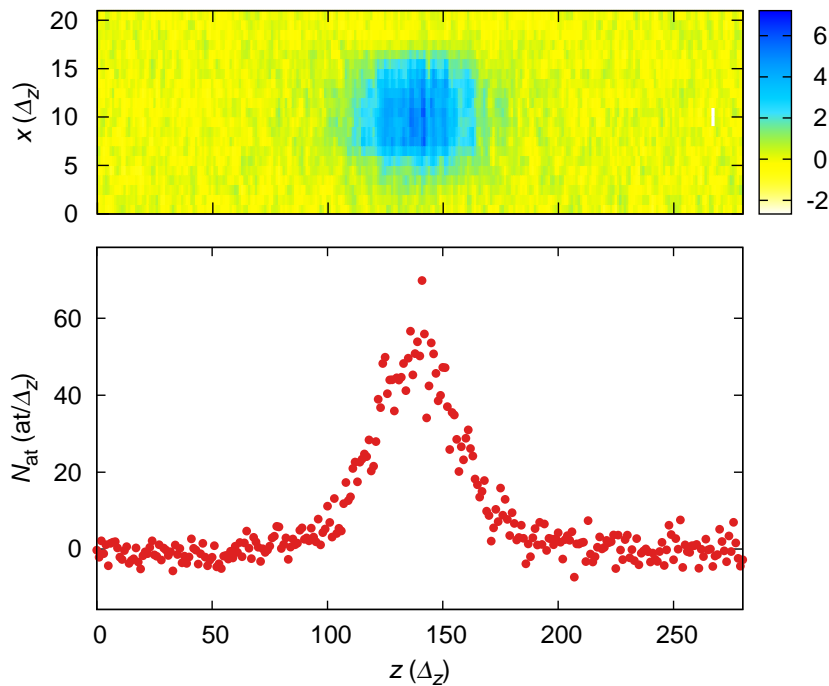


Figure 3.1.: Illustration of transverse integration. The top panel shows a single shot of raw atomic distribution recorded on the camera. The color scale are in units of atoms/pixel. After transverse integration according Eq. (3.1), the resultant linear atomic density is displayed in the bottom panel. The pixel size is $\Delta_z = 2.7 \mu\text{m}$.

A side remark: it goes without saying that one may also image a 2D system without integrating along the line of sight if it is perpendicular to the plane of the

system. However, no further discussion is given along this line, simply for the lack of relevance to our current setup. Interested readers may find information in e.g. Refs. [41, 79].

Still, depending on the exact sequence used to obtain the images, paired with appropriate analysis procedures, different pieces of information can be obtained. Since our experimental setup, together with others mentioned before [105, 150], deals with the motional degrees of freedom of 1D quantum gases, it is interesting to collect information in both *real* space and *momentum* space, and to treat the resulting collection of data to obtain the statistical *mean* and *fluctuations*. Tab. 3.1 summarizes the 2×2 array of independent probes² that can be used to characterize the system. All but the momentum correlations, for which the development is ongoing, have been shown to yield quantitative information about the system.

	real space	momentum space
mean	density profile	momentum distribution
fluctuations	atom-number fluctuations, density ripples	momentum correlations

Table 3.1.: 2×2 array of probed quantities, classified according to real- or momentum-space imaging, and the information yielded by the mean or fluctuations of the measurements.

I organize this chapter as follows. I first recall a few key points about absorption imaging, common to all probes, in Sec. 3.1. Sec. 3.2 is dedicated to the three probes in real space, whereas Sec. 3.3 is dedicated to the two probes in momentum space. The discussion of each probe is further divided into experimental procedures, analysis, and remarks. Since the extent of development for each probe differs, I only include quantitative analysis when possible. A conclusion will be given at the end of the chapter.

²I prefer to include the density ripples [105] as a probe in real space even though a finite time-of-flight is needed. Such a choice is motivated by the fact that the time-of-flight is not sufficiently long to reach the far field regime, and the information obtained but such measurements yields directly the two-body correlations in real space (see Sec. 3.2.3 for more details).

3.1. Absorption imaging

Only simple absorption imaging is carried out on our current setup. Since it is common to the measurements in both real and momentum space, I list a few key points to set the stage.

At the time when the desired atomic distribution is to be recorded, a nearly resonant probe beam is shone on the atoms and the first image is taken. A second image is taken 60 ms later in the absence of the atoms. The electronic signal registered in a pixel is converted to the photon number $N_{\text{ph}}^{(j)}$, with $j = 1, 2$ labelling the pictures, so that the atom number in the corresponding pixel can be obtained by

$$N_{\text{at}} = \frac{\Delta_z^2}{\sigma_e} \ln \left(\frac{N_{\text{ph}}^{(2)}}{N_{\text{ph}}^{(1)}} \right), \quad (3.2)$$

where $\Delta_z = 2.7 \mu\text{m}$ is the pixel size in the object plane, and σ_e denotes the effective scattering cross section, taking into account the saturation, the atomic level structure, and the Zeeman shift in the presence of a magnetic field [123]. More details will be presented in the discussions below.

Note that the subscript ‘at’ will be omitted from now on. N without specification will unambiguously denote the atom number, while the photon number will carry the subscript ‘ph’.

3.2. In real space

In order for the imaged density distribution to truthfully reflect the single-particle spatial distribution (density profile) of the system, one ideally needs to perform *in situ* imaging, so that no free evolution of the many-body wave function is allowed. This can be achieved by imaging the atoms while they are still trapped, or after a short³ time of flight (TOF). We implement the latter, as the rapid transverse expansion reduces the optical thickness of the sample and thus the resultant underestimation of atomic density due to both the effects of saturation and multiple

³compared to the typical longitudinal velocity.

scattering and the concavity of the logarithm in Eq. (3.2).

3.2.1. Mean density profile

Experimental procedures

Density profiles. At the end of the preparation, all traps are turned off abruptly. The atoms fall under gravity, and the cloud expands in the transverse direction for a duration of τ_{TOF} . The absorption imaging procedure described in Sec. 3.1 is then carried out with a low-intensity ($I_{\text{pr}} \sim 5\%I_{\text{sat}}$) probe beam so that saturation effects are negligible. A fairly long probe pulse $\tau_{\text{pr}} \simeq 150 \mu\text{s}$ is used here. Typically, $\tau_{\text{TOF}} \simeq 1 \text{ ms}$, allowing for sufficient transverse expansion.

Since the purpose of such images is to record the *shape* of the sample, in the event of high atomic density (and high optical thickness), the probe beam is detuned by a few MHz in order to reduce σ_e and therefore the absorption signal.

The resulting density distribution is however insufficient to yield the total number of atoms independently. First, the fact that the probe beam on our setup has a much larger spatial extent than the chip-to-atoms separation ($\sim 4 \mu\text{m}$) prevents an *ab initio* evaluation of σ_e . This is due to the change of probe polarization upon reflection on the (gold) chip surface. Second, a multiplicity occurs due to the double image of the atomic cloud and its reflection in the chip-mirror. Therefore, a different type of image is necessary to calibrate the total atom number.

Atom-number calibrations. This can be achieved by performing resonant absorption imaging at a longer $\tau_{\text{TOF}} \simeq 13 \text{ ms}$, by which time the transverse expansion ensures sufficiently low optical thickness at typical parameters explored, and the reflected probe beam does not pass through the atomic cloud again. A magnetic field is used to polarize the atoms, and a resonant probe beam of σ^+ polarization is used, so that $\sigma_e \rightarrow \sigma_0 = \frac{3\lambda^2}{2\pi}$. By integrating the resulting linear density distribution $N_{\text{calib}}(z)$, we obtain the total atom number $N_{\text{tot}} = \sum_z N_{\text{calib}}(z)$, which is then used to normalize the measured density profile to yield $N_{\text{prof}}(z)$ before further analysis is carried out. This method also allows to determine that $\sigma_e \simeq 0.8\sigma_0$ in the density profile measurements, provided the probe light is on resonance.

Typically, 30 shots of each kind of images are taken and their average is obtained. We verified experimentally that such a statistics gives sufficient signal to noise ratio for the minimization routine described below to be functional.

Analysis

Assuming thermal equilibrium and LDA, the density profile of the system is determined by the control parameters (f_z, f_\perp) , which are independently calibrated, and the thermodynamic parameters (μ_0, T) . Therefore, with the knowledge of (μ_0, T) , one can construct $(\mu(z), T)$, and obtain the corresponding $\rho(z)$ according to the MYY equation of state (see Sec. 2.2.1), so that a density profile $N_{\text{MYY}}(z) = \rho_{\text{MYY}}(z) \times \Delta_z$ can be found and compared with measurements $N_{\text{prof}}(z)$. See Fig. 3.2 as an illustration of such a computation routine.

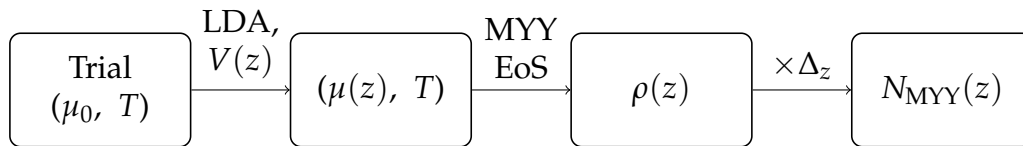


Figure 3.2.: Flow chart illustrating the routine to compute the density profile from the trial value of (μ_0, T) . EoS: equation of state.

A search for the (μ_0, T) that minimizes the Euclidean distance between $N_{\text{MYY}}(z)$ and $N_{\text{prof}}(z)$ then yields the central chemical potential and the temperature of the system.

As an example, I partially reproduce Fig. 3 of [83] in 3.3, where the measured density profile (points) and YY prediction⁴ (solid lines) in (b). The same figure also illustrates the agreement between the temperature obtained from the density profile and that from the atom-number fluctuations.

Remarks

This procedure has been reported applicable in different experiments [9, 83, 150, 153], and works as a method of thermometry particularly well for systems that are not too far into the qBEC regime. Indeed, since a 1D qBEC has a temperature-independent equation of state,

$$\mu = \rho g_{1D}, \quad (3.3)$$

⁴The low temperature of the sample renders the treatment of the transverse excited states unnecessary here.

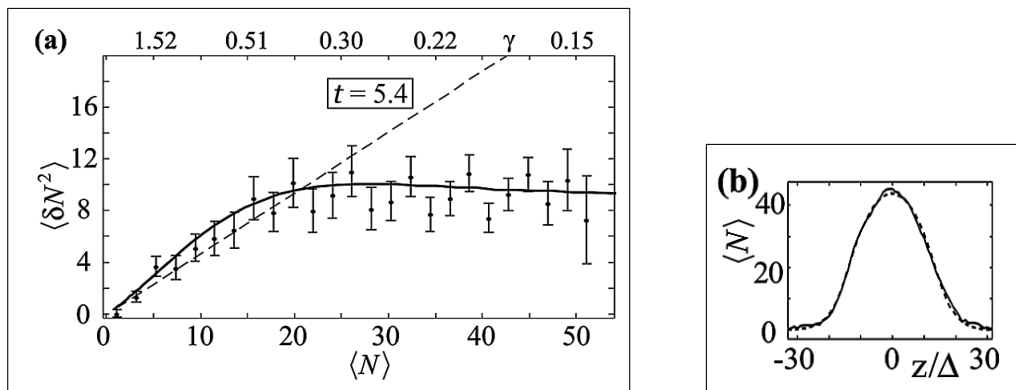


Figure 3.3.: Partial reproduction of Fig. 3 of [83]. For a sample with reduced temperature $t = 5.4$ (see Sec. 2.1.1), (a) compares the measured atom-number fluctuations (points) with YY prediction (solid line). Poissonian fluctuations (dashed line) are included as a reference. The top scale shows the values of the interaction parameter γ for the corresponding linear density (mean atom number/pixel), so that the central interaction parameter $\gamma_0 \simeq 0.15$. (b) compares the measured *in situ* density profile (solid line) with YY prediction (dashed line). Note that this data set was taken with an older imaging system, where the pixel size $\Delta = 4.5 \mu\text{m}$. Also, the low temperature renders transverse excited states irrelevant, and hence the use of the YY model.

the information about the temperature of a confined 1D gas is concealed in the outer regions of the trap, where the atomic density is sufficiently low for the equation of state to depart from Eq. (3.3) and to become temperature-dependent. However, the associated low signal makes it tedious and prone to inaccuracy to use such a thermometry for a sample deep inside the qBEC regime. In addition, MYY model does not take transverse smelling [recall Eq. (2.20)] into account, so that for samples in the 1D-3D crossover a with high linear density, the profile thermometry using MYY model is inaccurate [9]. Therefore, alternative methods such as the atom-number fluctuations are preferred.

3.2.2. Atom-number fluctuations

In analogy with the thermometry based on the measurements of Johnson noise across a resistor, it is also possible to measure the temperature of a cold atomic sample by probing the atom-number fluctuations.

Experimental procedures

Fluctuation profiles. The procedures used to obtain the density profiles for the fluctuation analysis, $N_{\text{fluct}}(z)$, is in fact similar to that discussed in Sec. 3.2.1. Only the differences are highlighted below:

1. τ_{TOF} is reduced to $50 \mu\text{s}$ in order to minimize the effect of longitudinal motion of the atoms;
2. A short and intensive probe pulse maximizes the signal: so that these profiles are taken with the probe intensity $I_{\text{pr}} \simeq 0.15I_{\text{sat}}$ and pulse duration $\tau_{\text{pr}} = 80 \mu\text{s}$. Such parameters fall within the validity⁵ of an effective scattering cross section model used in [123],

$$\sigma_e = \frac{\alpha_e \sigma_0}{1 + \alpha_e \frac{I_{\text{pr}}}{I_{\text{sat}}}}, \quad (3.4)$$

where the parameter $\alpha_e \simeq 0.8$ is found experimentally.

3. By contrast to the density-profile measurements, the probe detuning for the fluctuation profiles is often set to null despite a large optical thickness in order to maintain a high SNR [82]. Instead, a correction procedure is used in the analysis.

For sufficient statistics, 200 to 300 of such images are recorded.

Analysis

The fluctuation profiles are first corrected for the underestimation of the atom number due to large optical thickness. This is achieved by fitting a second order polynomial to map the average fluctuation profile onto the mean density profile as explained in [11, 82]. This map is then applied to all fluctuation profiles.

Next, we obtain the atom-number fluctuations⁶ $\delta N(z)^2 = (N(z) - \langle N(z) \rangle)^2$ by

⁵Ref. [82] verifies the validity by a comparison with the optical Bloch equations.

⁶the variance in this case. Off-diagonal terms of the fluctuation matrix $\langle \delta N(z) \delta N(z' \neq z) \rangle$ is not easily accessible, since it is difficult to optically resolve the typical values of correlation length (submicron for typical linear density and interaction strength on our experiment). It is however possible to measure higher moments of the fluctuations. For instance, the measurement of the third moment $\langle \delta N^3 \rangle$, which yields information about three-body correlations, is reported in [10].

comparing the individual profile $N(z)$ with a running average $\langle N(z) \rangle$. Note that the 'fluct' subscript is omitted in this section for brevity. About 30 profiles bracketing the current profile are used in the running average to reduce the sensitivity towards slow experimental drifts. Photon shot noise $(\Delta_z^2/\sigma_e)^2 \sum_x (1/N_{\text{ph}}^{(1)}(x, z) + 1/N_{\text{ph}}^{(2)}(x, z))$ is irrelevant and subtracted for each integrated pixel at position z . The resulting values of $\delta N(z)^2$ is binned according to its associated $\langle N(z) \rangle$ and the unbiased estimate of the variance $\langle \delta N^2 \rangle$ is obtained. Note that binning removes the initial position dependence, which is irrelevant under LDA.

The finite resolution amounts to a reduction of the measured fluctuations compared to theory by a factor κ . We determine κ by computing the correlations between the atom-number fluctuations in neighboring pixels. Details can be found in [82].

According to the fluctuation dissipation theorem, the fluctuations of the atomic density obeys,

$$\langle \delta \rho^2 \rangle = \frac{k_B T}{\Delta_z} \left. \frac{\partial \langle \rho \rangle}{\partial \mu} \right|_T, \quad (3.5)$$

so that a single pair of (μ_0, T) can be obtained by minimizing the Euclidean distance between the measured $\langle \delta N^2 \rangle$ and $\kappa k_B T \Delta_z \left. \frac{\partial \langle \rho \rangle}{\partial \mu} \right|_T$ predicted by equation of state for each bin of $\langle N \rangle$.

The example in Fig. 3.3 illustrates the measurement with a sample that approaches the strongly interacting regime ($t = 5.4$). The repulsive interactions result in the suppression of atom-number fluctuations below the shot-noise level.

Such a measurement can also be done for hotter samples in the dimensional crossover. I reproduce Fig. 1 of [9] in Fig. 3.4 as a demonstration. Here, saturation of the atom-number fluctuations (above shot-noise level) is absent in (a) the (3D) sample of IBG with $t = 2500$, but clearly visible for the qBEC samples shown in (b) $t = 790$ (nearly 1D) and (c) $t = 52$ (1D).

Several options exist to use the atom-number fluctuation measurement as a thermometry. Either the entire curve of $\langle \delta N^2 \rangle$ vs $\langle N \rangle$ can be fit to the numerical prediction of MYY equation of state, or the saturated level of $\langle \delta N^2 \rangle$ at high density can be compared with the asymptotic equation of state of qBEC. The choice of strategy eventually depends on the thermodynamic regime of the gas.

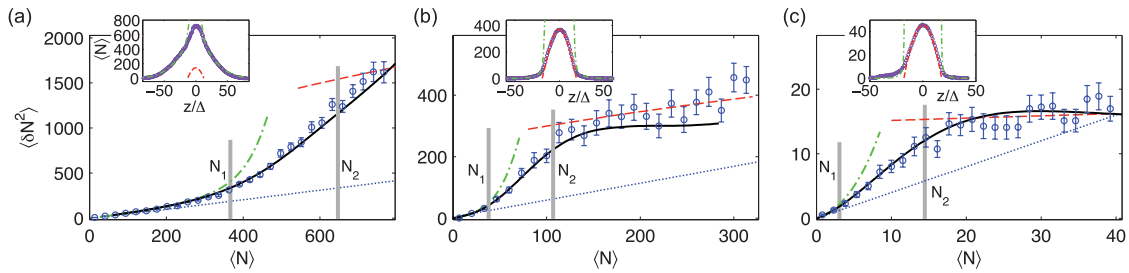


Figure 3.4.: Reproduction of Fig. 1 of [9]. Atom-number fluctuations (main graphs) and *in situ* density profile (insets) are shown for three data sets. Samples differ in their dimensionality: $k_B T / (\hbar \omega_\perp) =$ (a) 3.6, (b) 1.0, and (c) 0.09. Data (points) are compared with MYY prediction (solid lines), IBG prediction (dash-dotted lines), and qBEC prediction (dashed lines). Shot-noise level (dotted lines) are shown as a reference. The insets show the corresponding *in situ* density profiles with the same convention as the main graphs. Here, the pixel size $\Delta = 4.5 \mu\text{m}$, and the labels N_1 and N_2 are related to the discussion about the dimensional crossover (see [9] for more details). For a reference, I also include the values of the dimensionless parameters: $(t, \gamma_0) = (2500, 0.0015)$, $(790, 0.0039)$, and $(52, 0.0395)$ respectively.

Remarks

As discussed in [9], this method is complementary to the thermometry based on the measurements of *in situ* density profile, and their agreement in the quasicondensation crossover has been demonstrated.

The atom-number fluctuation thermometry is also applicable to the experiment of (quasi-) 1D Bose gas in Oberthaler's group in Heidelberg [88], although the analysis procedures differ. Namely, it does not explicitly use an equation of state, but relies on the LDA and profile smoothing, i.e.

$$\langle \delta N^2 \rangle = \kappa k_B T \Delta_z \frac{\partial z}{\partial \mu} \frac{\partial N}{\partial z}, \quad (3.6)$$

where $\frac{\partial z}{\partial \mu} = -\frac{\partial z}{\partial V(z)}$ is determined by the longitudinal potential $V(z)$, and $\frac{\partial N}{\partial z}$ can be obtained from smoothed profiles $N(z)$, so that the atom-number fluctuations remain as a function of position, and the temperature can be obtained from the flat regions (in white) of $\langle \delta N^2 \rangle \frac{\partial N}{\partial z}$ (see Fig. 3.5). Such an analysis procedure is more applicable on the Heidelberg experiment for the following reasons:

1. There, the atoms are trapped in an optical dipole trap, which gives a better

characterized potential compared to our surface magnetic trap that is prone to imperfections caused by fabrication and surface adsorption;

2. The better resolution ($\Delta_z/L \simeq 1/250$) makes it possible to identify substantial regions where the temperature signal is constant and is not overwhelmed by noise. The contrary is true when attempts were made to apply the same procedure on our setup where $\Delta_z/L \simeq 1/100$.

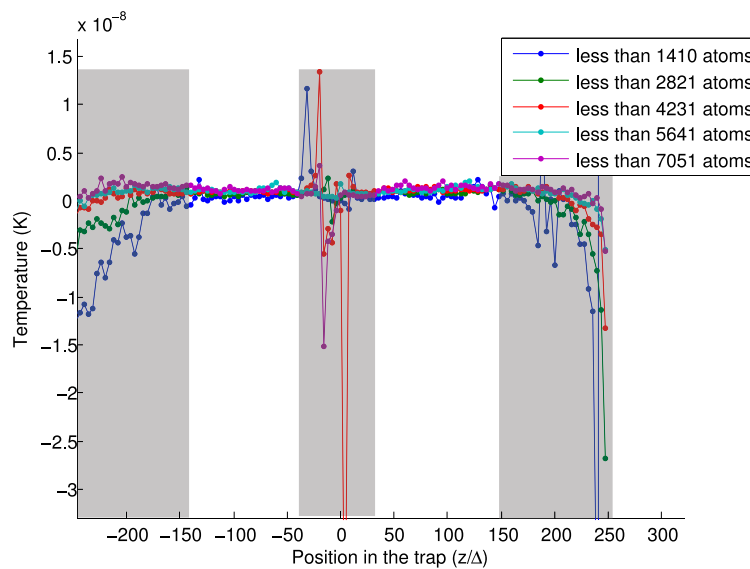


Figure 3.5.: Reproduction of Fig. 8 of [88], courtesy of Ms. Aisling Johnson. The temperature is evaluated from the atom-number fluctuations in a pixel at position z . Due to the finer grid ($\Delta_z/L \simeq 1/250$), substantial regions (in white) with nearly constant temperature signal can be identified. The measured temperature is $T = (1.1 \pm 0.4)$ nK.

3.2.3. Density ripples

Density fluctuations develop during the near-field free expansion of a trapped low-dimensional system as a signature of the thermal and quantum phase fluctuations initially present. Such variations, poetically nicknamed ‘density ripples’, have a spectrum that is directly related to the two-body correlation functions of the trapped system. 1D qBECs constitute an ideal system to observe these ripples, since the near absence of the radial dynamics permits an elegant analytic theory description [81]. The amplitude of the observed density variations is shown to be

a thermometry [105].

Experimental procedures

An intermediate value of τ_{TOF} is necessary for density ripples to manifest. On our experiment, coincidentally, the imaging procedures described under ‘Atom-number Calibration’ (recall $\tau_{\text{TOF}} \simeq 13$ ms and is kept as a controlled parameter) is ideal for this purpose, though significantly larger statistics (about 400 images) are necessary for an acceptable thermometry.

Analysis

We follow the procedures described in [105]. Only key points are listed below.

Starting from the integrated profiles $N_{\text{calib}}(z)$, we obtain the normalized two-body correlation function

$$\tilde{g}_2(z, \tau_{\text{TOF}}) = \frac{\langle \sum_u N_{\text{calib}}(u) N_{\text{calib}}(u+z) \rangle}{\sum_u \langle N_{\text{calib}}(u) \rangle \langle N_{\text{calib}}(u+z) \rangle}, \quad (3.7)$$

where $\langle \rangle$ denotes ensemble averaging. Note that the technical noise is uncorrelated and contributes only to the autocorrelation $\tilde{g}_2(0, \tau_{\text{TOF}})$. This can be evaluated independently and removed before the ensemble averaging and normalization [105]. Also, the $\tilde{g}_2(z, \tau_{\text{TOF}})$ obtained from experimental measurements is necessarily broadened by the finite imaging resolution. The unbroadened two-body correlation function, denoted as $g_2(z, \tau_{\text{TOF}})$, can be obtained from theory.

Depending on the thermodynamic regime of the system, different options exist for quantitative comparison with theory:

- In the qBEC regime, both density and phase fluctuations behave like Gaussian random variables, so that the spectrum of the density ripples and the two-body correlation function after expansion can be worked out analytically [81]. Alternatively, numerical methods such as the Ornstein-Uhlenbeck process [63] can be used to simulate the initial phase profile. The expanded density profile and $g_2(z, \tau_{\text{TOF}})$ can then be computed;
- In the qBEC to IBG crossover, since thermal fluctuations are expected to dominate, a classical field approximation [26, 28] can be used to simplify

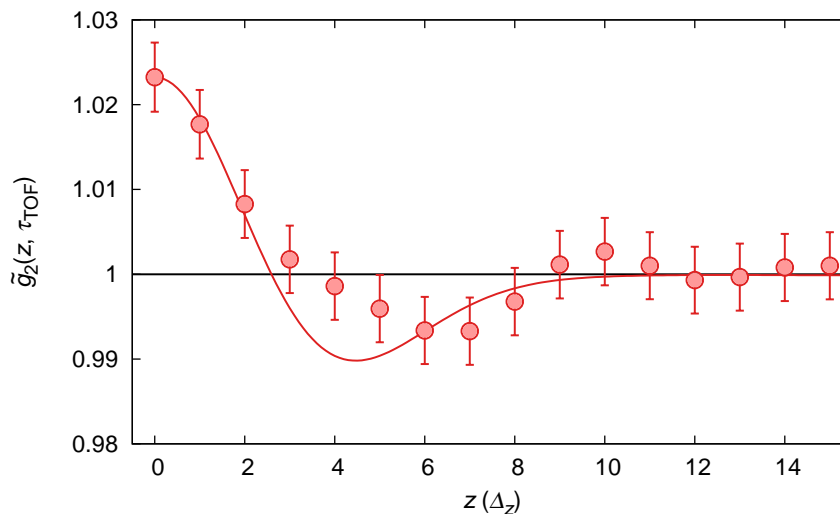


Figure 3.6.: Demonstration of the $\tilde{g}_2(z, \tau_{\text{TOF}})$ measurement on our experiment. Data (points) deduced from about 400 shots of atom-number calibration scans (see Sec. 3.2.1) are compared with trial SGPE calculations (solid line, courtesy of Mr. Wolfgang Rohringer) carried out for our experimental parameters. The error bars account for statistical errors only.

the full quantum-many-body problem. Numerical methods such as the stochastic Gross-Pitaevskii equation (SGPE) or QMC simulation can be used to compute the expanded profile and thus the two-body correlation.

The temperature T is kept as a variable and the above options are to be evaluated over a range of T values. The computed $g_2(z, \tau_{\text{TOF}})$ should be convolved with the imaging resolution in order to yield a fair comparison with the experimental data [127]. Here, we demonstrate the second option in Fig. 3.6, where data (points) are compared with the SGPE calculations (solid line, courtesy of Mr. Wolfgang Rohringer⁷) carried out for our experimental parameters. As a first trial, the comparison is rather satisfactory, although the quantitative difference of the position of the minimum calls for finer adjustments.

Finally, since for any given τ_{TOF} , $g_2(0)$ varies monotonously with T , the measurement of $\tilde{g}_2(0)$ constitutes yet another a thermometry. Figure 3.7 places our trial measurement (point) on the SGPE calculations (solid line, again, courtesy of Mr. Wolfgang Rohringer). Note that the temperature is an input for the *ab initio* cal-

⁷Vienna Center for Quantum Science and Technology, Atominstitut, TU Wien, 1020 Vienna, Austria.

ulation, while the data are placed according to the density-profile thermometry [$T_{\text{prof}} = (110 \pm 10) \text{ nK}$] discussed in Sec. 3.2.1. Again, the fair agreement in this trial prompts further verification.

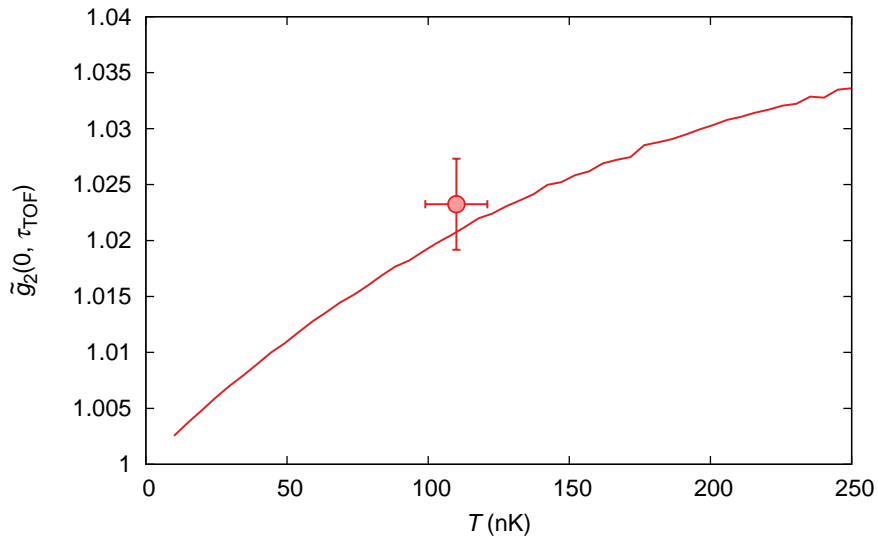


Figure 3.7.: Demonstration of the density-ripple thermometry on our experiment. Data (point, with temperature obtained by density-profile thermometry explained in Sec. 3.2.1) and SGPE calculation (solid line, courtesy of Mr. Wolfgang Rohringer) show fair agreement. Fine adjustments and further verifications are needed for confirmation.

Remarks

This method was pioneered by the Vienna group [105], and has been only recently implemented on our setup as a demonstration. Its accuracy depends strongly on sufficient statistics, more than that required by the atom-number fluctuation thermometry.

Within this exercise, there seems to be fair agreement between the profile thermometry and density ripple measurements. Fine adjustments in the calculation and further verification with more data sets are necessary for confirmation.

3.3. In momentum space

Imaging a 1D ultracold atomic gas in momentum space is a feat. The conventional TOF technique employed in higher dimensions becomes problematic due

to the elongated geometry of the 1D sample, in the sense that too long a τ_{TOF} is necessary to reach far field, where the imaged density distribution is homothetic to the momentum distribution if interaction energy is properly removed at the start of the flight. This however requires an imaging setup and parameters vastly different from a usual *in situ* imaging system, unless special schemes such as magnetic levitation [99] is employed to prevent the atoms from falling under gravity.

Two alternative solutions have been realized in the community: Bragg spectroscopy [46, 47, 61, 78, 124] and the focusing technique [39, 84, 150], each with its own merits. The former probes the population of individual momentum component, while the latter gives access to the entire distribution at the same time, and is implemented on our experiment. Technical details can be found in [82]. I only list a few key points below.

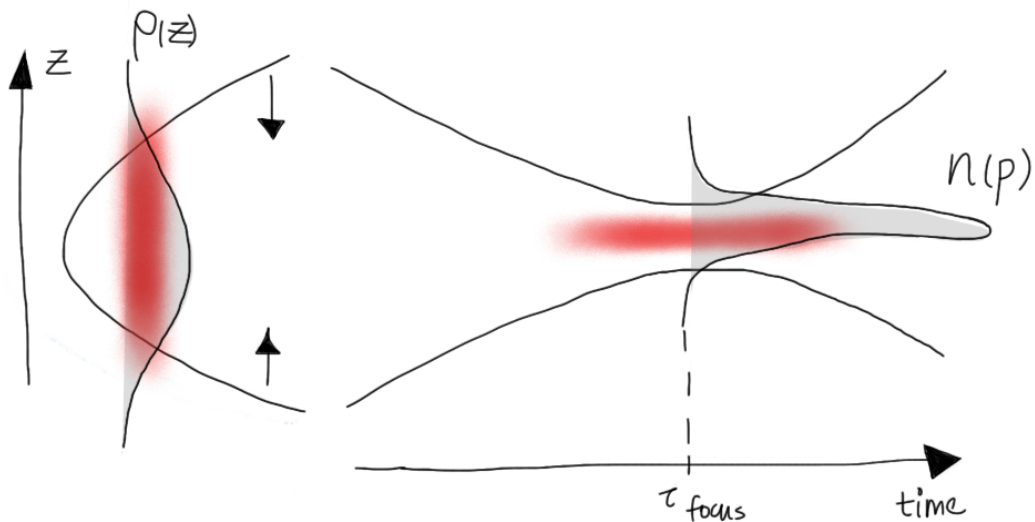


Figure 3.8.: An illustration of the focusing technique. The atoms are focused by a parabolic magnetic field. After a focusing time τ_{TOF} , the spatial distribution corresponds to the initial momentum distribution of the atoms.

- The process is analogous to focusing light with a lens (see Fig. 3.8). We focus the atoms using a parabolic magnetic field generated by four (instead of two) current-carrying wires in order to minimize aberration, as the anharmonic terms in the focusing potential up to the fifth order are cancelled over a spatial region much larger than that of the 1D cloud.
- A short ($\tau_{\text{kick}} \simeq 0.7$ ms) pulse of the focusing potential ($\omega_{\text{kick}} \simeq 2\pi \times 40$ Hz)

is applied in the longitudinal direction, followed by a two-step transverse deconfinement, removing the interaction energy ($\propto g_{1D} \propto \omega_{\perp}$).

- The focusing time $\simeq 1/(\omega_{\text{kick}}^2 \tau_{\text{kick}}) \simeq 25$ ms corresponds to the time of flight τ_{TOF} , before an absorption image is taken. This corresponds to a pixel size in momentum space $\Delta_p = \Delta_z m / \tau_{\text{TOF}} \simeq 0.14 \hbar \mu\text{m}^{-1}$, and is true for all measurements described in Part II.
- A guiding technique [82] consisting of holding the atoms in a weak transverse wave guide, between the two stages of deconfinement, allows to prolong the focusing time (now the sum of τ_{TOF} and the holding duration), and thus to improve the momentum-space resolution. This is however not used in experiments described in Part II, and will not be elaborated further. Technical details concerning this technique can be found in [82].

3.3.1. Momentum distribution

Experimental procedures

Approximately 30 pictures are taken using the focusing technique outlined above and their mean is computed.

Analysis

Assuming LDA, the measured momentum distribution can be seen as a weighted sum of momentum distributions, each of them being associated to an homogeneous system with different linear density (in real space). Since the computation of the momentum distribution requires the full knowledge of the one-body correlation function in real space, it is beyond the capability of the YY (or MYY) equation of state. Instead, we compare our measurement with QMC calculations, obtained by using the Stochastic Series Expansion (SSE) algorithms [145], and taking the continuous limit of the lattice Boson model [134, 135]. Note that the longitudinal confinement can be accounted for in the calculation directly, although for practical purposes⁸ we use the numerical data for homogeneous systems at different (μ, T) in conjunction with LDA and interpolate to obtain T .

⁸In particular, the asymptotic momentum distribution is known for *homogeneous* qBEC and IBG, so that having QMC data on the same footing simplifies interpolation and fit routines.

The finite imaging resolution due to the optical response and the atomic diffusion broadens the observed momentum distribution. Assuming a Gaussian PSF, we have the RMS width in momentum space $\delta_p \simeq 2\Delta_p$ typically. This is determined by fitting the momentum distribution of a sample that is clearly below resolution to a Gaussian distribution. Such a PSF is then used to broaden the QMC calculations in the fit routine.

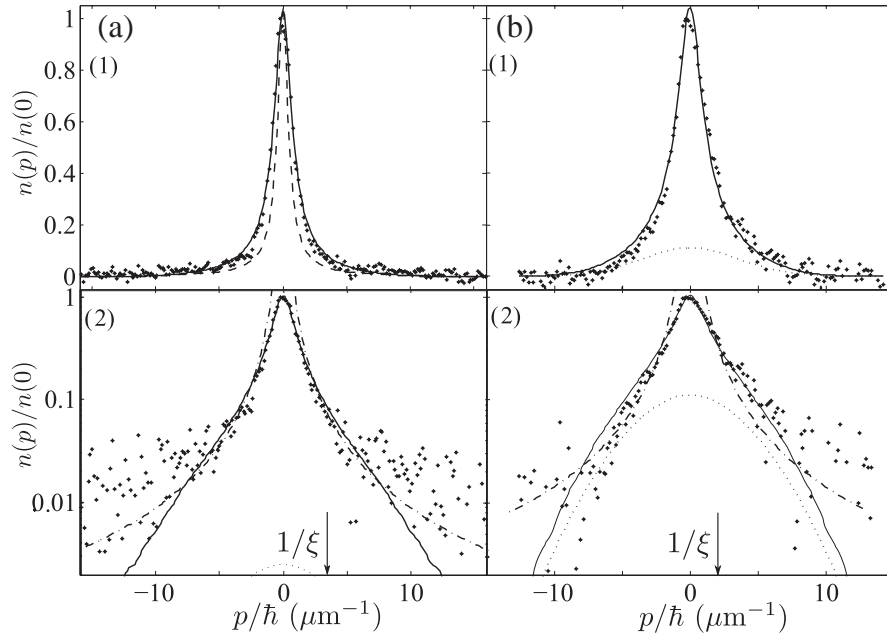


Figure 3.9.: Reproduction of Fig. 5 (partial) of [84]. The normalized momentum distribution $n(p)/n(0)$ is shown for two sets of data in both (1) linear and (2) log scale. Samples differ in their thermodynamic regime: (a) the sample is further in the qBEC regime, with $f_{\perp} = 6.4$ kHz and $T = 72$ nK determined from the QMC fit; (b) this sample is further in the degenerate IBG regime, with $f_{\perp} = 2.1$ kHz and $T = 84$ nK. Data (points) are compared to a QMC fit (solid lines) and a qBEC Lorentzian prediction [dashed line in (a,1)]. The contribution from transverse excited states (dotted lines) and the $1/p^2$ behavior (dash-dotted lines) are included as reference. The inverse healing length $1/\xi$ is also indicated for both samples.

As a demonstration, I reproduce Fig. 5 (partial) of [84]. (a) shows a sample further in the qBEC regime, for which the momentum distribution is narrow compared to $1/\xi$ (the inverse healing length), (b) shows a sample further in the degenerate IBG regime, for which the momentum distribution is broad compared to $1/\xi$. Data (points) are compared to QMC fit (solid lines), yielding $T =$ (a) 72 nK, and (b) 84 nK.

Remarks

Momentum profile as a thermometry has been demonstrated on our experiment in [84], where the agreement with the atom-number fluctuation thermometry is shown. In the earlier implementation of the focusing technique in Amsterdam [39, 150], on the other hand, the authors obtained the total kinetic energy from the momentum distribution, and showed agreement with MYY equation of state. We remark that this strategy is applicable to hotter samples with significant populations in the transverse excited states, so that the momentum distribution displays fast decaying tails at high momenta (see Fig. 3.10), enabling a double Gaussian fit (dashed lines). The stochastic projected GPE calculations (solid lines in Fig. 3.10) also confirms this feature. On the contrary, our measurement for colder samples and the corresponding QMC calculations give $n(p) \propto p^{-2}$ (see Fig. 3.9), rendering the direct measurement of kinetic energy ($\propto p^2$) problematic⁹. Note that a finite kinetic energy is ensured by $n(p) \propto p^{-4}$ for large p in this case, but it is not observed for the signal-to-noise ratio¹⁰ of about 50 of our experiment, nor is it visible on the calculation.

3.3.2. Momentum correlations

Experimental procedures

Similar to the case in real space, more statistics are necessary for fluctuation measurements in momentum space. A typical set of data for this purpose contains about 150 images taken with the focusing technique described at the beginning of this Sec. 3.3.

Analysis

The raw data are analyzed using a similar post selection procedure as detailed in [82] to reject bad shots due to technical issues. Next, the momentum fluctuations $\delta N(p) \equiv N(p) - \langle N(p) \rangle$ is obtained by a comparison with the running average $\langle N(p) \rangle$, similar to the procedure used to analyze the fluctuation data *in situ* (see Sec. 3.2.2). We also observe a technical fluctuation of the total atom

⁹Direct evaluation of $\langle p^2 \rangle = \Delta_p \sum_p p^2 n(p)$ is sensitive to the noise present in the region where there is little atomic signal.

¹⁰simply defined as the maximal atomic signal divided by the RMS noise signal.

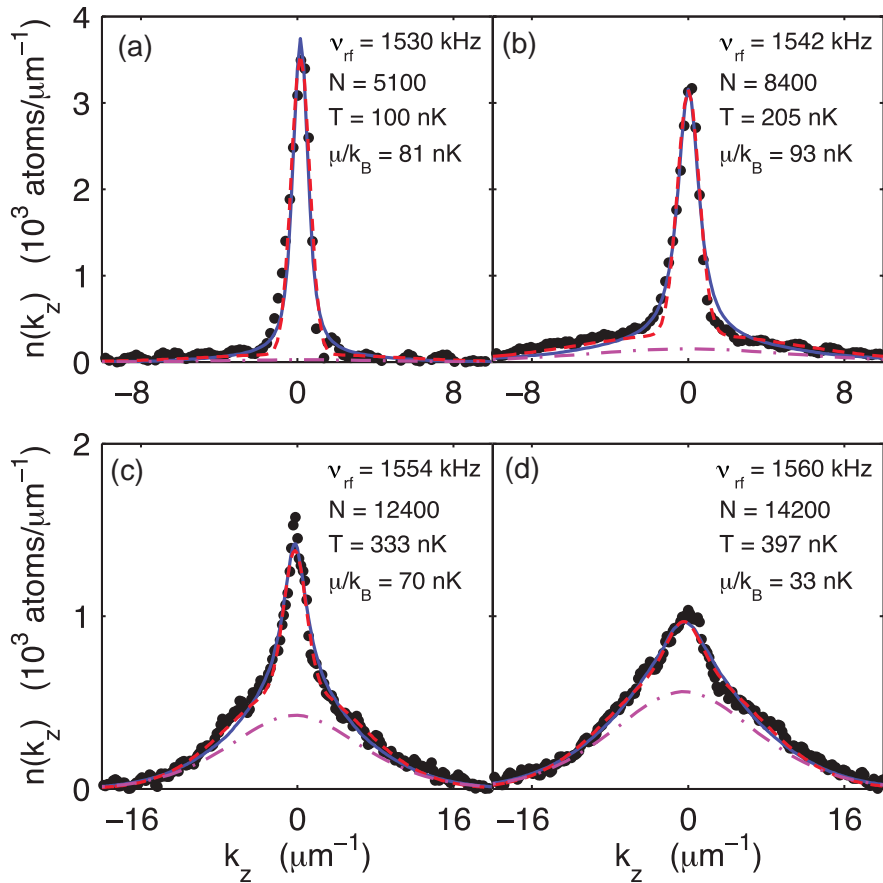


Figure 3.10.: Reproduction of Fig. 2 of [39]. The momentum distribution is shown for samples of different temperatures controlled by the final trap depth, which is fixed by the RF assisted evaporation (ν_{rf} in the labels). Data (points) are compared with double Gaussian fit (dashed lines) and stochastic projected GPE calculation (solid lines). Both theories are hardly distinguishable. Contributions from the transverse excited states (dash-dotted lines) are also shown.

number on the order of 15% to 20%, which is beyond the expected fluctuations based on the grand canonical ensemble. Data are thus renormalized according to the atom-number calibration scans and treated as a system in the canonical ensemble for consistency¹¹. Finally, the ensemble average of the correlation map $\langle \delta N(p) \delta N(p') \rangle$ is computed, and the photon shot noise, which is uncorrelated and therefore only contributes to the diagonal $p = p'$, is subtracted.

The computation of the correlation map depends on the thermodynamic regime of the system. To start with, we consider homogeneous systems. In qBEC, the

¹¹We verify that the renormalization procedure does not change the qualitative behavior of the momentum correlations obtained. Such a choice places the data and analysis (canonical ensemble treatment) at equal footing, and would hopefully facilitate quantitative comparisons.

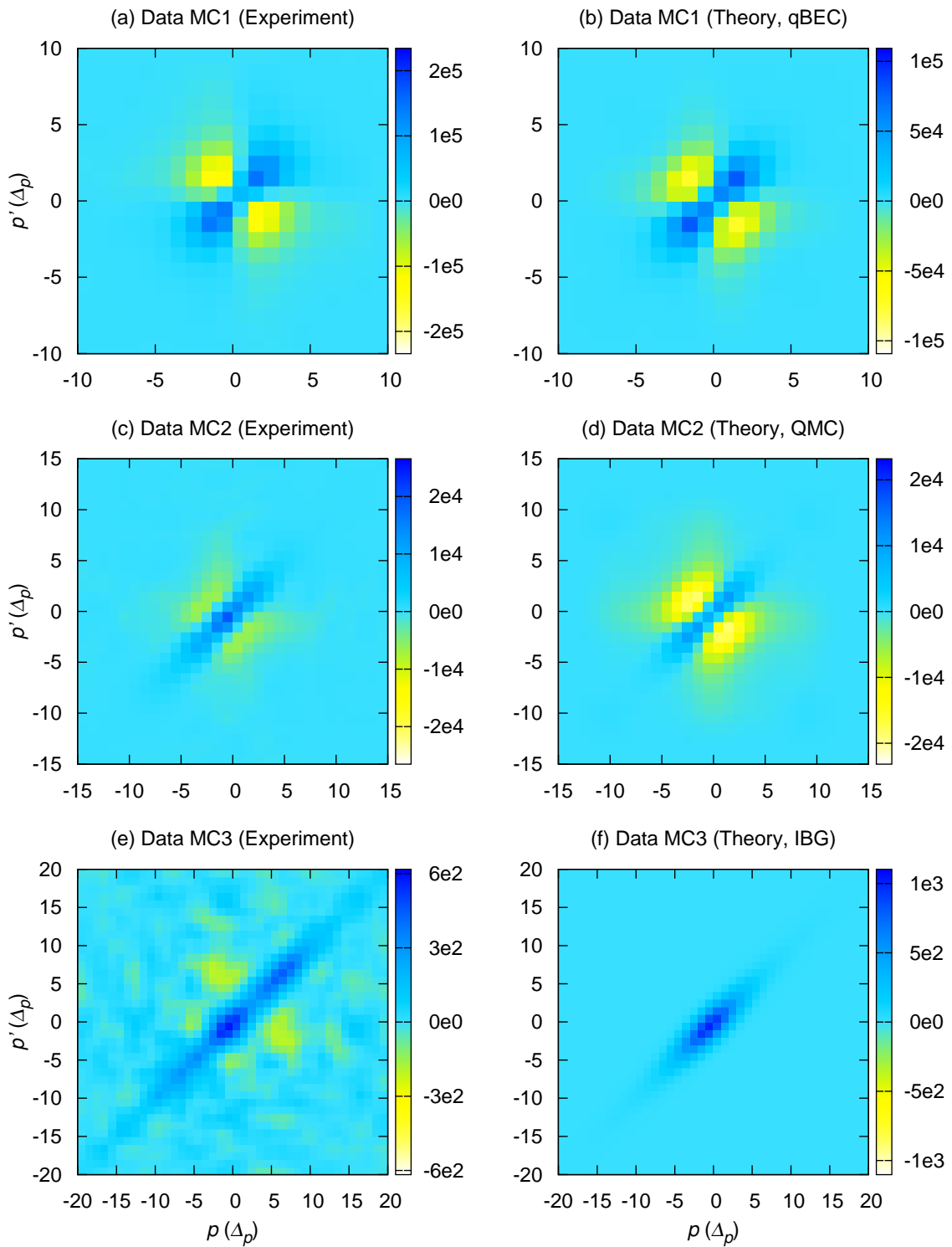


Figure 3.11.: The momentum correlations of three samples in the qBEC to IBG crossover. Data (left) are compared with *ab initio* theory (right). The zero crossing of the color map is kept the same throughout.

Luttinger liquid theory yields an analytic expression [17], predicting strong correlations due to bunching along the $p = p'$ diagonal, and strong *anticorrelations* along the $p = -p'$ diagonal. This is in stark contrast with an elongated BEC in 3D, where positive correlations are expected in both diagonals. In the IBG limit, since interactions are absent, the single-particle eigenstates have well-defined momenta, giving rise to the shot noise. A system approaching degeneracy also exhibits bunching in momentum space. The overall correlation is therefore only present in the $p = p'$ diagonal. Numerical methods such as the QMC can be used for systems in the qBEC to IBG crossover, and a smooth variation from one limiting behavior to the other is expected.

Figure 3.11 shows a comparison of the measured and computed momentum correlations for sample sets of data of a qBEC (MC1), a system in the qBEC to IBG crossover (MC2), and a degenerate IBG (MC3). The zero crossing of the color map is kept the same throughout in order to give a fair visual comparison. T_{prof} of the data sets are around 100 nK, and further consistency checks across different thermometries are ongoing. There seems to be a good agreement between the measurements and theory. The slight difference in the absolute magnitude of the correlation is currently under investigation.

Remarks

The measurement of momentum correlations has been realized recently on our experiment. In order to apply such a probe as a quantitative characterization of 1D Bose gases, a single meaningful quantity should be established. This is not a trivial task as the experimental resolution (effective PSF modeled as a Gaussian with RMS width $\simeq 2\Delta_p$) has a strong impact on the extreme values of the correlation map. Also, given that f_{\perp} and the focusing parameters have been held constant so far, the thermodynamic regimes are probed by tuning the linear density.

Conclusions

In this chapter, we have first seen how simple absorption imaging can be carried out in both real and momentum space on our setup. Next, five experimental probes have been presented, each allowing an independent char-

acterization of the 1D system. The mean density profile, the atom-number fluctuations, the density ripples, and the momentum distribution can all be used as thermometry methods, and their equivalence is demonstrated to a certain extent, although further verification would be helpful. The application of the momentum correlations as a quantitative characterization tool is currently under development.

Part II.

Probing Nonequilibrium Systems

Having established a comprehensive understanding of the equilibrium behavior of harmonically confined 1D Bose gases and their experimental realizations, I document in the following part the experiments I performed in order to investigate the nonequilibrium behavior of 1D Bose gases. Various means of excitation have been attempted, and the subsequent evolution is studied.

I organize this part as follows. Chapter 4 details the study of the breathing mode of 1D Bose gases, for which both frequency and lifetime are probed experimentally and theoretically. In Ch. 5, an experimental study about a long-lived nonequilibrium state is presented. Such a state has been obtained repeatedly on our experiment, and a detailed characterization helps to understand the initial conditions before the system is brought out of equilibrium by other means. Chapter 6 then details a few attempts made to deliberately bring the system far from equilibrium by means of modifying the interaction strength. Such a study is however on going, and only the efforts up to March 2014 are recorded here.

4. Breathing Modes

Contents

4.1. Motivation	62
4.2. Experimental procedures	63
4.2.1. Considerations	63
4.2.2. Procedures	64
4.2.3. Quantities of interest	65
4.3. Frequency study	67
4.3.1. Limiting cases	67
4.3.2. Crossovers	82
4.4. Lifetime studies	91

We study here the breathing modes of a harmonically confined 1D Bose gas. This subject has been investigated on various occasions in both theory [58, 107, 144] and experiments [73, 94, 110], mostly focusing on the frequency shift as the system traverses different thermodynamic regimes. With the capability of imaging in momentum space, however, we experimentally demonstrate for the first time a phenomenon of momentum-space frequency doubling [48]. We discuss its physical origin and explore the regimes of occurrence in the 1D phase diagram. The lifetime of the breathing mode is also probed experimentally.

I organize this chapter as follows. I discuss the motivation behind such a study in Sec. 4.1. Sec. 4.2 outlines the considerations, the procedures as well as the quantities of interest. The study of the frequency signature is presented in Sec. 4.3, where both the limiting cases and the crossovers are explored. The study of the lifetime is presented in Sec. 4.4, and is limited to some preliminary data. A conclusion is given at the end.

4.1. Motivation

Collective excitations are a valuable source of information for the understanding of the physics that governs interacting many-body systems, e.g. the nucleus of an atom [131], or an ultracold atomic gas in external confinement [21, 35, 56, 69, 70, 86, 106, 108, 114, 115, 142, 143]. The breathing mode, which is an oscillatory motion where the system varies in size and sometimes in density, is among the simplest form of such excitations. These modes lie directly above the center-of-mass oscillations, and are the lowest-lying nontrivial collective oscillations of the system. In higher dimensions, there exist both the monopole oscillations [35] for a spherically symmetric trap, where both the size and the density oscillate in time, and the quadrupole oscillations [21], where the atomic density is preserved during the size oscillations of the ensemble. The latter however relies on the availability of more than one translational degree of freedom, and is therefore impossible in 1D.

Existing studies of the breathing mode in 1D have demonstrated that the oscillation frequency of the size and of the density in real space is directly related to the thermodynamic regime of the systems [58, 107, 144], but a quantitative comparison taking finite-temperature effects into account has yet to be established [73, 110]. Moreover, momentum-space imaging has only been carried out in the strongly interacting regime [94], with an initialization that depletes the low-momenta states and hence the investigation of breathing mode *per se* is questionable. What is interesting in that work is perhaps the very first demonstration of the connection between the degree of integrability ('1D-ness' in this context) and the lack of thermalization of the system.

With the possibility to image in both real and momentum space, as well as the thermometries available on our set up, we wish to investigate the breathing mode as a first step towards the experimental studies of the evolution dynamics of nonequilibrium systems in 1D.

4.2. Experimental procedures

4.2.1. Considerations

The breathing mode is in fact rather accessible experimentally. On one hand, the sum rules [107] tell us that a system in a harmonic confinement would respond to a sudden jump in the trapping frequency with oscillatory mean-square width. On the other hand, the notion of a well defined ‘mode’ suggests parametric excitation.

For the experiments that I performed, the first option was chosen for two reasons:

1. The implementation is simple: the longitudinal harmonic confinement is provided by running stabilized currents through the wires on the atom chip, so that a jump in the trapping frequency can be achieved by a fast¹ ramp of the current values;
2. Assuming the ramp is infinitesimally short, modelling the change of the trapping frequency as a step function in time becomes rather realistic, and is used in our analysis.

In addition, the following technical constraints are taken into account:

1. The typical longitudinal trap has a frequency $f_z \simeq 7$ Hz, for which the preparation procedure outlined in Sec. 1.3 is optimized, so that all samples start in such a trap.
2. The final trapping frequency should not be too low to avoid possible anharmonicity of the trap and to ensure sufficiently many oscillation periods are observed within a given period of time. This suggests that a direct downward quench in f_z is not desirable.

¹compared to the oscillation period $1/f_z$ associated with the trap.

4.2.2. Procedures

With these considerations in mind, we carry out the experiment as follows. We first use the preparation sequence (see Sec. 1.3) to produce 1D samples of ^{87}Rb of desired temperature and density. Next, we excite the breathing mode by means of a quench in the longitudinal potential: we slowly compress the samples from $f_z = f_D \simeq 7$ Hz to $f_z = f_0 \simeq 9$ Hz in 50 ms, and then release them back into the final trap $f_z = f_D$ in 1 ms. The samples are allowed to evolve for a variable duration τ before an image is taken, either in real space² or in momentum space³. Figure 4.1 gives an illustration of f_z as a function of time.

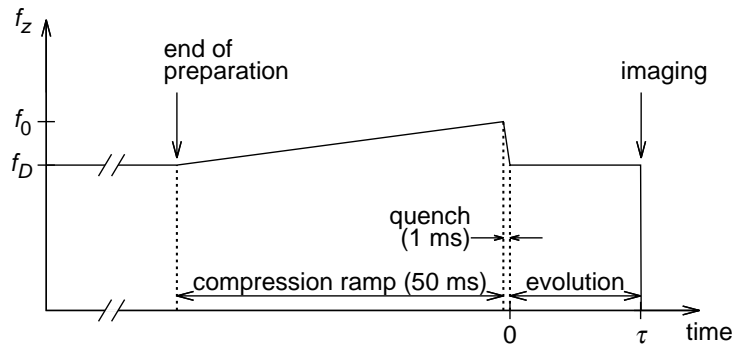


Figure 4.1.: Sequence of f_z quench.

Since $1/f_D \simeq 140$ ms, the 1 ms quench is nearly instantaneous. The slowness of the 50 ms compression is justified experimentally. Assuming a simple trap opening, the subsequent evolution of the breathing mode has a well defined phase, which is what we observe on the experiment. We also compare the $\rho(z)$ and $n(p)$ measured at $\tau = 1$ ms (see Fig. 4.2), when there is little time for significant changes to take place, to the computed equilibrium profiles for $f_z = f_0$, and for the temperature T_{prof} given by an independent calibration⁴ using the density-profile thermometry (see Sec. 3.2.1) in the absence of the quench sequence. The good agreement between the measured and computed profiles provides grounds

²using the imaging parameters of ‘Density profile’ described in Sec. 3.2.1, and detuned when necessary, so that the atomic density is always proportional to the registered absorption signal, up to a numerical factor. This way, profile distortion is avoided and the width can be obtained by a simple fit routine.

³using the focusing technique (see Sec. 3.3). Only one set of imaging parameters is developed here.

⁴We emphasize that the profile temperature is used for this comparison. A discrepancy between the density-profile thermometry and the atom-number fluctuation thermometry has been observed here. This will be discussed later in further details in Sec. 4.3.2.1.

for neglecting the effect of the compression.

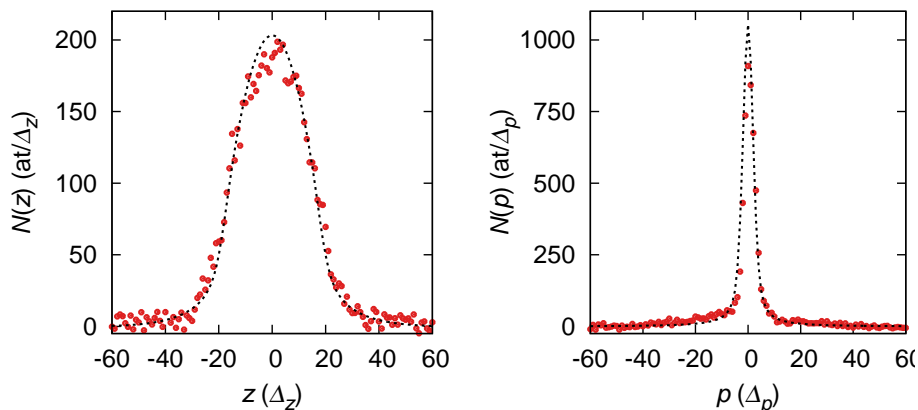


Figure 4.2.: Profiles *in situ* $N(z) = \rho(z)\Delta_z$ and at focus $N(p) = n(p)\Delta_p$ at $\tau = 1$ ms. Data (points) are compared with calculations (dotted lines) using the MYY model for $\rho(z)$ and QMC simulations for $n(p)$, both evaluated at $f_z = f_0$ and a temperature T_{prof} obtained from an independent calibration using the density-profile thermometry (see Sec. 3.2.1) in the absence of the quench sequence. The computed momentum distribution is convolved with a Gaussian PSF of RMS width $\sim 2\Delta_p$ to account for the imaging resolution at focus. The numerical QMC data are a courtesy of Dr. Tommaso Roscilde^a.

^aLaboratoire de Physique, CNRS UMR 5672, Ecole Normale Supérieure de Lyon, Université de Lyon, 46 Allée d'Italie, Lyon, F-69364, France.

4.2.3. Quantities of interest

As for any oscillations, we are interested in both the frequency and the amplitude of the motion. The frequency signal allows to identify the mode itself, and the thermodynamic properties of the quantum many-body system. It has received more attention in the literature so far, both in theory [58, 107, 144] and in experiments [73, 110]. The amplitude could yield the response of the system to the excitation, and its evolution gives the lifetime of the mode [35, 70].

We have performed experiments to investigate both quantities. In addition to the usual trap geometry $(f_{\perp}, f_z) \simeq (2000, 7)$ Hz, the following parameters are controlled:

- The quench strength $\alpha \equiv f_0/f_D \simeq 1.3$ is fixed. This value is chosen so that

there is sufficient oscillation signal in the widths of the profiles measured. We verify experimentally that the measured breathing frequency hardly depends on α for up to $\alpha \sim 3$. Large values of α are less favorable due to strong expansion and weak absorption signal.

- The longest evolution time τ_{\max} is kept at 500 ms for the frequency study and up to 900 ms for the lifetime study. This is motivated by the accuracy of the fit which yields both quantities. Ideally, the longer τ_{\max} (or the more oscillations, whichever is the limiting factor), the more accurate the fit becomes. However, compromises have to be made since the isolation of the system is imperfect and a residual (small) loss in the total atom number would eventually render measurements impossible at long times.

We vary the thermodynamic regime of the 1D atomic samples by tuning the final evaporation step so that samples of desired temperature and density are obtained.

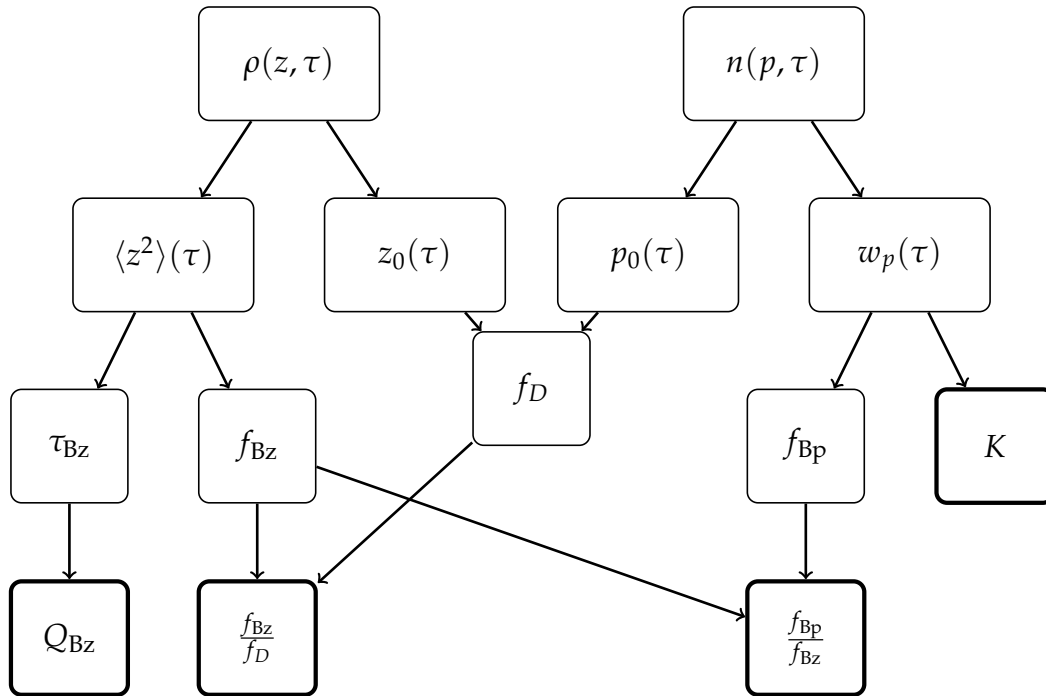


Figure 4.3.: Chart illustrating the relationship of various quantities in the study of the breathing mode. The bold boxes highlight the final quantities of interest.

The frequency (the f 's, with various subscripts), the amplitude [K , see Eq. (4.27) and related discussion], and the lifetime (τ_{Bz} , and thus the quality factor Q_{Bz}) are

obtained from the width and the center of the observed atomic distributions. One could in principle obtain the breathing frequency by analyzing the density variation over time, as done in [146]. However, since the width and density are necessarily coupled in 1D, we prefer to analyze the widths as they are less susceptible to noise registered in the image, be it technical or due to density fluctuations. The mean square width in real space $\langle z^2 \rangle$ is obtained by fitting the averaged density profile by an inverted parabola or a Gaussian, depending on the thermodynamic regime of the sample (see discussion in Sec. 4.3.2.1). The square is kept for the convenience of modeling (see also Sec. 4.3.2.1). In momentum space, however, the equivalent $\langle p^2 \rangle$ cannot be obtained experimentally for the reasons discussed in Sec. 3.3.1. Instead, a fit to a Lorentzian distribution yields the half width at half maximum (HWHM) w_p , which carries the information of a similar kind. Distinction between $\langle p^2 \rangle$ and w_p is made for the case of a Tonks gas, where the exact solution allows the computation of both quantities. The evolution of the centers $z_0(\tau)$ and $p_0(\tau)$ yields the dipole oscillation frequency f_D . Figure 4.3 illustrates the relations of the various quantities explained in this paragraph.

4.3. Frequency study

Here, we focus on the frequency signature of the breathing mode. A combination of theoretical and experimental approaches are used in order to explore various regions of the 1D phase diagram (recall Fig. 2.1). I will first present the limiting cases, and then the crossovers between them.

4.3.1. Limiting cases

Let us look at the breathing dynamics of the limiting cases. Four of these will be covered: the qBEC, IBG, TG gas, and exceptionally, two classical hard spheres. The first two cases are studied experimentally whereas the last two theoretically.

4.3.1.1. Quasicondensate (qBEC)

Sample characteristics

The first sample presented here lies in the qBEC regime, characterized by an equilibrium density profile of an inverted parabolic shape, with little wings in the outer region. Quantitatively, we have

$$N_{\text{tot}} \simeq 7000, \quad (4.1)$$

$$T_{\text{prof}} = 102 \text{ nK}, \quad (4.2)$$

where T_{prof} denotes the temperature obtained from fitting the density profile (see Sec. 3.2.1). Note that the statistical uncertainty on N_{tot} is about 15%, and the convergence of T_{prof} due to the fit routine is typically 10%, although interpolation of numerical MYY equation of state may result in a larger error. The peak density is around 66 atoms/ μm . Therefore, in terms of the dimensionless parameters, we have

$$(t, \gamma_0) = (1220, 0.00309). \quad (4.3)$$

Breathing behavior

We show the measured real- and momentum-space profile evolution in Fig. 4.4 (a) and (c). The color scale corresponds to the measured (relative) number of atoms in a pixel, consecutive snapshots are taken 10 ms apart, and we recall that the real (momentum) pixel size is $\Delta_z = 2.7 \mu\text{m}$ ($\Delta_p = 0.14 \hbar \cdot \mu\text{m}^{-1}$).

The apparent mismatch in periodicity prompts further investigation. We plot in Fig. 4.5, as a function of time τ , $\langle z^2 \rangle$ obtained from an inverted-parabola fit of the density profile, and w_p obtained from a Lorentzian fit of the momentum distribution. The statistical error is shown for the first 100 ms.

Fitting each width with a damped sinusoid (see Fig. 4.5, the solid line in the top panel) yields $f_{\text{Bz}} = 12.0 \text{ Hz}$ and $f_{\text{Bp}} = 24.1 \text{ Hz}$. Together with the dipole frequency $f_D = 6.95 \text{ Hz}$, independently obtained by fitting the center-of-mass oscil-

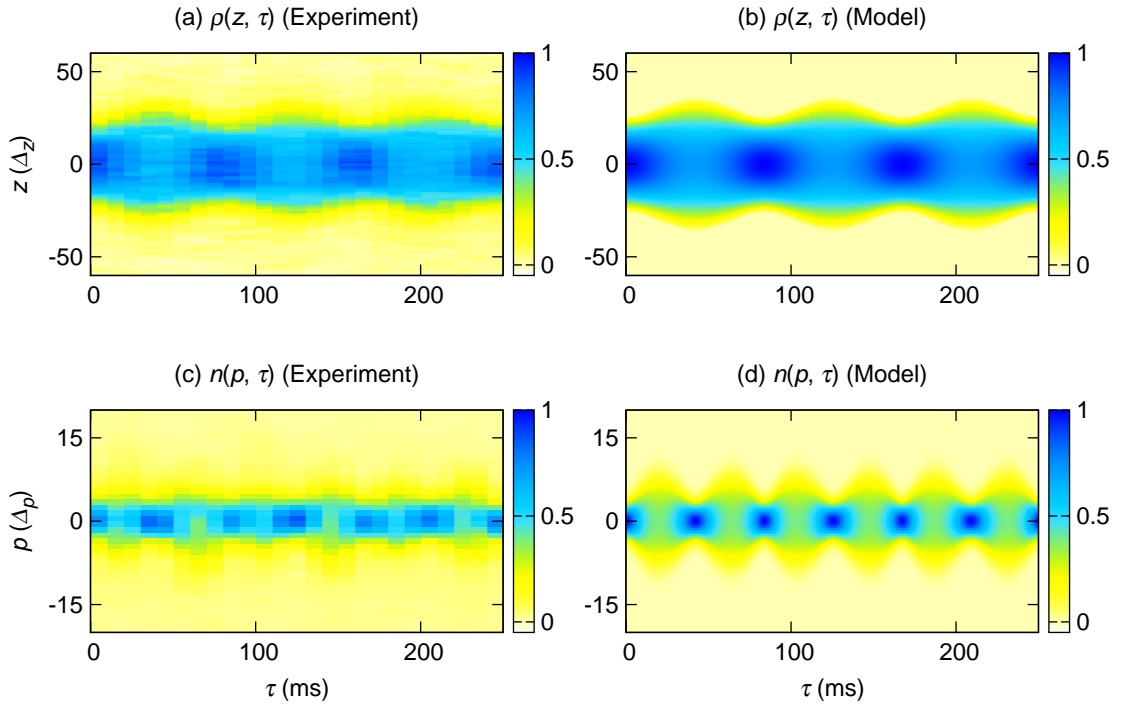


Figure 4.4.: Breathing dynamics in real (top) and momentum (bottom) space. Data (left) and the scaling solution (right) are shown. The momentum distribution according to the scaling solution in (d) is broadened by the experimental imaging resolution. Each picture is normalized to the corresponding maximal signal per pixel.

lations, we obtain

$$\frac{f_{Bz}}{f_D} = 1.73 \pm 0.03, \quad (4.4)$$

$$\frac{f_{Bp}}{f_{Bz}} = 2.00 \pm 0.02. \quad (4.5)$$

Note that the uncertainty only accounts for the fitting error.

Model

A hydrodynamic analysis predicts the frequency of the breathing mode of a 1D qBEC to be $f_{Bz} = \sqrt{3} f_D \simeq 1.732 f_D$ [107]. It was soon verified experimentally [73, 110], and our measurement again confirms this prediction. We note that the authors of [73] in fact used such a measurement to identify the qBEC regime.

On the other hand, the frequency expected in momentum space has barely been discussed in literature, possibly as a consequence of a naïve intuition that the col-

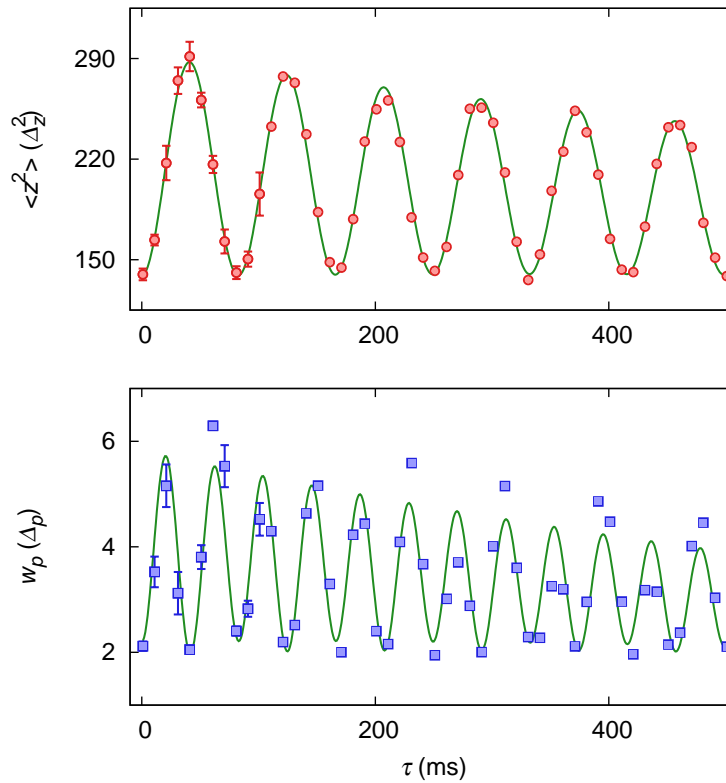


Figure 4.5.: Width variations of a qBEC. Data (points) are compared with fits (lines): $\langle z^2 \rangle$ is fitted with a damped sinusoid, whereas w_p is fitted with a two-frequency model [see Eq. (4.27) and related discussion]. The statistical error is shown for the first 100 ms.

lective behavior *should* manifest itself in the same way regardless of whether the observation takes place in real or momentum space. Indeed, the seminal work of Haller *et al* [73] simultaneously claims the measurement of momentum distribution and $f_B = \sqrt{3} f_D$. As it turns out, given the published experimental parameters, the finite TOF used in their work indicates a *near-field* expansion, with the atomic cloud expanding in the longitudinal direction by approximately a factor of 3. Therefore, the measured breathing frequency reflects the value in real space.

Yet, it is possible to show that $f_{Bp}/f_{Bz} = 2$ from the much celebrated scaling solution [27]. Namely, starting from the steady-state inverted parabolic density profile, a sudden stepwise change in external potential results in an oscillatory behavior of the density profile that is completely summarized in a single scaling

parameter $b(\tau)$, i.e.

$$\rho(z, \tau) = \frac{1}{b(\tau)} \rho\left(\frac{z}{b(\tau)}, \tau = 0\right), \quad \text{with } \ddot{b} + \omega_D^2 b = \frac{\omega_0^2}{b^2}, \text{ and } b(0) = 1, \dot{b}(0) = 0. \quad (4.6)$$

Linearizing b around its initial value of unity, one recovers the hydrodynamic prediction that b oscillates at a frequency $\sqrt{3} f_D$, and so does the width of the density profile that is linear in b . What is more interesting is that the authors of [27] observed that the scaling solution is equivalent to assuming that each particle has a well defined classical trajectory $v(\tau) = \frac{\dot{b}(\tau)}{b(\tau)} z(\tau = 0)$, so that the (hydrodynamic) velocity field is linear in position, and its width follows the time dependence of $\left|\frac{\dot{b}(\tau)}{b(\tau)}\right|$. The linearization of b implies \dot{b} is sinusoidal, and $\left|\frac{\dot{b}(\tau)}{b(\tau)}\right|$ has a periodicity half that of b , and thus $f_{Bp}/f_{Bz} = 2$ exactly. I include the evolution of the density profile and momentum distribution according to the scaling solution in Fig. 4.4 (b) and (d).

Note that the model above remains imperfect. The assumption that only the hydrodynamic velocity field contribute to $n(p)$, corresponding to neglecting thermal fluctuations in our case, leads to a vanishing momentum width whenever \dot{b} crosses 0. This is certainly not the case in a quantum many-body system. The samples that we prepare are dominated by thermal fluctuations. Our measurement of the momentum width is in addition affected by the finite resolution of the imaging. The calculation shown in Fig. 4.4 (d) only shows the scaling solution broadened by the finite resolution. The agreement with the measured distributions is remarkable.

Also, one could in principle take thermal fluctuations into account using numerical methods (see the discussion in Sec. 3.2.3). Assuming a qBEC behavior, a trial simulation is carried out using an Ornstein-Uhlenbeck process [63] for $\alpha = 1.3$, $t\gamma_0^{3/2} = 0.06$, and $\frac{\mu_0}{\hbar\omega_\perp} = 1670$ (see Fig. 4.6). The computed momentum distribution is then fitted with a Lorentzian, from which we obtain $\left|\frac{\dot{b}(\tau)}{b(\tau)}\right|$. Here the thermal fluctuations indeed prevent the momentum width from vanishing as expected, and the agreement with the scaling solution is otherwise good.

Discussions

Comparing our experiment with theory, the origin of the momentum-space frequency doubling becomes clear. In each breathing cycle, the momentum distribu-

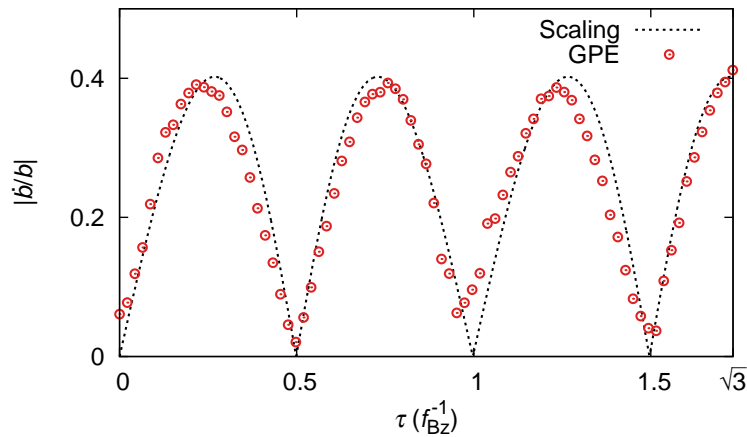


Figure 4.6.: Comparison of the scaling solution (line) with GPE simulations (points). The thermal fluctuations indeed prevent the momentum width from vanishing at every half a breathing period ω_{Bz}^{-1} , and the agreement between the two models is otherwise good. Note that the oscillations are shown for one dipole period, ending at $\tau = \sqrt{3}/\omega_{Bz}$, so that $f_{Bz}/f_D = \sqrt{3}$ is implicit.

tion narrows twice: at the classical turning point when the *in situ* density profile is the broadest, and at the *compression* point when the density profile is the narrowest. The former is expected in any system, as the atoms climb the (external) potential hill and the population in low momenta becomes high. The latter corresponds to a self-reflection of the atomic ensemble, and the interaction potential is responsible for slowing down the atoms. In addition, the timescales over which the momentum distribution narrows in both scenarii are comparable, leading to the observation that the oscillation of the momentum width takes place twice as fast as that of the *in situ* width.

The scaling solution is also valid in higher dimensions [27, 116], so that in principle, the momentum-space frequency doubling is expected in these systems. There is however no experimental proof to our knowledge, possibly because the early experiments using simple TOF techniques did not measure the true momentum distribution due to the contribution of interaction energy.

In addition, the understanding of the origin of such a momentum-space frequency doubling allows us to improve further the experimental control. Namely, due to energy considerations, the maximal value of w_p should remain constant as a function of time in case of *undamped* breathing oscillations, or decreases mono-

tonically with time otherwise. We observed irregularities that can be attributed to the imperfect implementation of the focusing technique, i.e., the focusing pulse and τ_{TOF} are mismatched, analogous to making an observation slightly away from the focal point in optics. By monitoring the maximal value of w_p while fine tuning the duration of the focusing pulse, we are able to determine the duration of the focusing pulse within $\pm 20 \mu\text{s}$.

4.3.1.2. Ideal Bose gas (IBG)

Sample characteristics

Next, we present a sample in the (degenerate) IBG regime, characterized by an equilibrium density profile with a significant population in the outer region of the longitudinal potential, and the shape can be well described by a Gaussian. Quantitatively, we have

$$N_{\text{tot}} \simeq 2000, \quad (4.7)$$

$$T_{\text{prof}} = 105 \text{ nK}. \quad (4.8)$$

The notation and uncertainty are similar to before. The peak density is around 18 atoms/ μm . Therefore, in terms of the dimensionless parameters, we have

$$(t, \gamma_0) = (1130, 0.0099). \quad (4.9)$$

Breathing behavior

Again, we plot $\langle z^2 \rangle$ and w_p as a function of time τ . The shape of the density profile prompts a Gaussian fit to obtain $\langle z^2 \rangle$ instead. The statistical error is significantly larger than before due to the reduced density signal, despite the fact that more shots are used for averaging.

Fitting each width with a damped sinusoid (see Fig. 4.14, the solid line in the top panel) yields $f_{\text{Bz}} = 13.5 \text{ Hz}$ and $f_{\text{Bp}} = 13.9 \text{ Hz}$. Together with the dipole

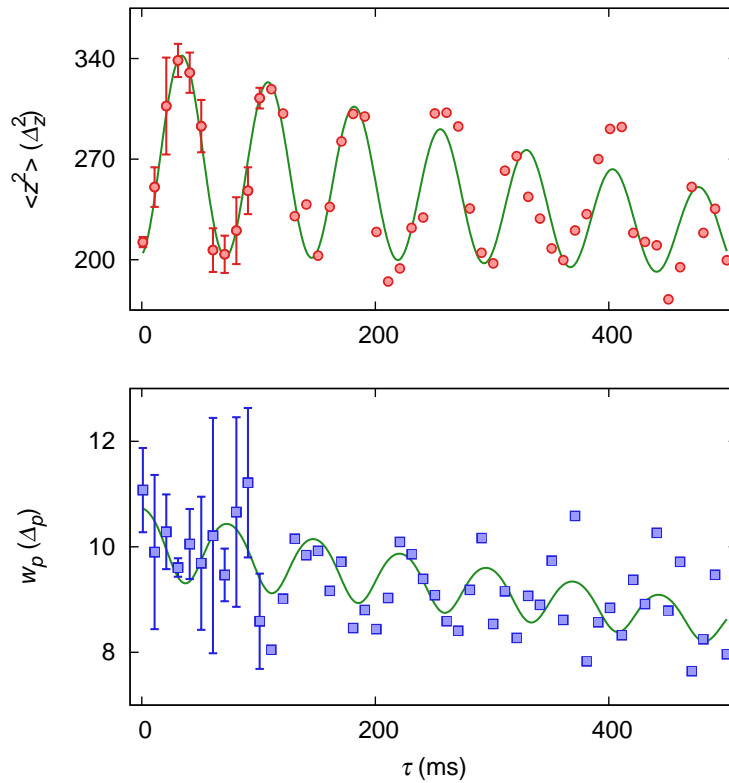


Figure 4.7.: Width variations of an IBG. Data (points) are compared with fits (lines): $\langle z^2 \rangle$ is fitted with a damped sinusoid, whereas w_p is fitted with a two-frequency model [see Eq. (4.27) and related discussion]. The statistical error is shown for the first 100 ms.

frequency $f_D = 7.35$ Hz, we obtain

$$\frac{f_{Bz}}{f_D} = 1.84 \pm 0.04, \quad (4.10)$$

$$\frac{f_{Bp}}{f_{Bz}} = 1.03 \pm 0.04. \quad (4.11)$$

Again, the uncertainty only accounts for the fitting error.

Model

The ideal Bose gas consists of noninteracting particles, so that a single-particle description is sufficient. Consider the Schrödinger equation of a simple harmonic oscillator. Again, for a sudden change in trapping potential, a scaling solution exists (for all eigenstates), with the scale $b(\tau)$ now obeying

$$\ddot{b} + \omega_D^2 b = \frac{\omega_0^2}{b^3}, \text{ and } b(0) = 1, \dot{b}(0) = 0. \quad (4.12)$$

The solution is analytic, namely,

$$b(\tau) = \sqrt{1 + (\alpha^2 - 1) \sin^2(\omega_D \tau)}, \text{ such that} \quad (4.13)$$

$$b^2(\tau) = \frac{\alpha^2 + 1}{2} - \frac{\alpha^2 - 1}{2} \cos(2\omega_D \tau). \quad (4.14)$$

Therefore, $\langle z^2 \rangle$, being quadratic in b , would also oscillate at $f_{Bz} = 2f_D$ exactly. Note that Eq. (4.12) also applies to a TG gas, as discussed in the next subsection.

It also follows that the width of the momentum distribution would scale as $1/b(\tau)$, so that the same frequency $f_{Bp} = f_{Bz} = 2f_D$ applies in both real and momentum space, even though the evolution of the momentum width is no longer purely sinusoidal. On the other hand, by energy conservation arguments, $\langle p^2 \rangle$ oscillates sinusoidally at $2f_D$.

A side remark. Pictorially, the breathing motion can be described by a rotation of the phase-space density, so that the widths in real and momentum space, obtained by projecting the phase-space density onto the real and the momentum axis, oscillate out of phase at the same frequency.

Discussions

Although the measured ratio f_{Bz}/f_D has yet to reach the IBG limit, a single frequency is seen in both real and momentum space. The antiphase between the oscillations in the *in situ* and momentum width is also clearly observed.

4.3.1.3. Tonks-Girardeau gas (TG gas)

The Tonks-Girardeau (TG) gas is a system of impenetrable (hard-core) bosons [64], i.e. a system that can be described by the LL model in the limit of $g_{1D} \rightarrow \infty$, so that it is a prototypical system with strong interaction.

Even though it has not been possible to reach this regime on our experiment, some theoretical analysis appears instructive to the understanding of the subject at hand.

Model

Using the celebrated Bose-Fermi mapping, which treats the infinitely strong interaction as a boundary condition, one can construct the many-body ground-state wave function of N harmonically trapped impenetrable bosons as

$$\Psi_{\text{TG}}(z_1, \dots, z_N) = \frac{1}{\sqrt{N!}} |\det \phi_j(z_k)|, \quad (4.15)$$

where ϕ_j denotes the j th harmonic orbital. The Slater determinant gives the anti-symmetric wave function of N fermions, and the absolute value arises from a unit antisymmetrizer that repairs the boson symmetry. Such prescription is proven to be accurate on many occasions, see e.g. [30] and references therein, and can be extended to treat other systems with the same boundary conditions [65].

Since the Hamilton operator now contains no interaction terms, the scaling law is the same as that of a single particle in a harmonic trap, see Eq. (4.12). We then have all the ingredients needed to compute the density evolution in real and momentum space after a quench of the longitudinal potential:

$$\begin{aligned} \rho_{\text{TG}}(z, \tau) &= \frac{1}{b(\tau)} \int dz_2 \dots dz_N \left| \Psi_{\text{TG}}\left(\frac{z}{b(\tau)}, \dots, z_N; \tau = 0\right) \right|^2, \\ n_{\text{TG}}(p, \tau) &= \frac{1}{b(\tau)} \int dz_2 \dots dz_N \left| \int dz e^{\frac{ipz}{\sqrt{2\pi\hbar}}} \Psi_{\text{TG}}\left(\frac{z}{b(\tau)}, \dots, z_N; \tau = 0\right) \right|^2. \end{aligned} \quad (4.16)$$

Given the special structure of harmonic orbitals and determinants, mathematical simplifications exist so that the multivariable integral of the determinant reduces to a determinant of special functions [54], and the computation for up to at least $N = 11$ can be performed efficiently using Matlab.

Breathing behavior

We show $\rho_{\text{TG}}(z, \tau)$ and $n_{\text{TG}}(p, \tau)$ for one dipole period in Fig. 4.8 (a) and (c). Here, we recover a momentum-space frequency doubling⁵, which has been implicit in [109]. More quantitatively, we plot $b^2(\propto \langle z^2 \rangle)$ in Fig. 4.8 (b) and w_p in Fig. 4.8 (d) as a function of time τ , with w_p obtained by directly computing the *exact* HWHM of the instantaneous momentum distribution. b^2 oscillates at $f_{\text{Bz}} = 2f_D$ exactly,

⁵The argument used to show that the momentum width of IBG scales as $1/b(\tau)$ does not hold because of the absolute value in Eq. (4.15).

whereas $f_{Bp} = 4f_D$ dominates in the oscillations of w_p . $|\dot{b}/b|$ (normalized to the maximal value of w_p) is included in Fig. 4.8 as a reference. We see that similarly to the case of a qBEC (see Fig. 4.6), the assumption of classical trajectory again fails at small w_p .

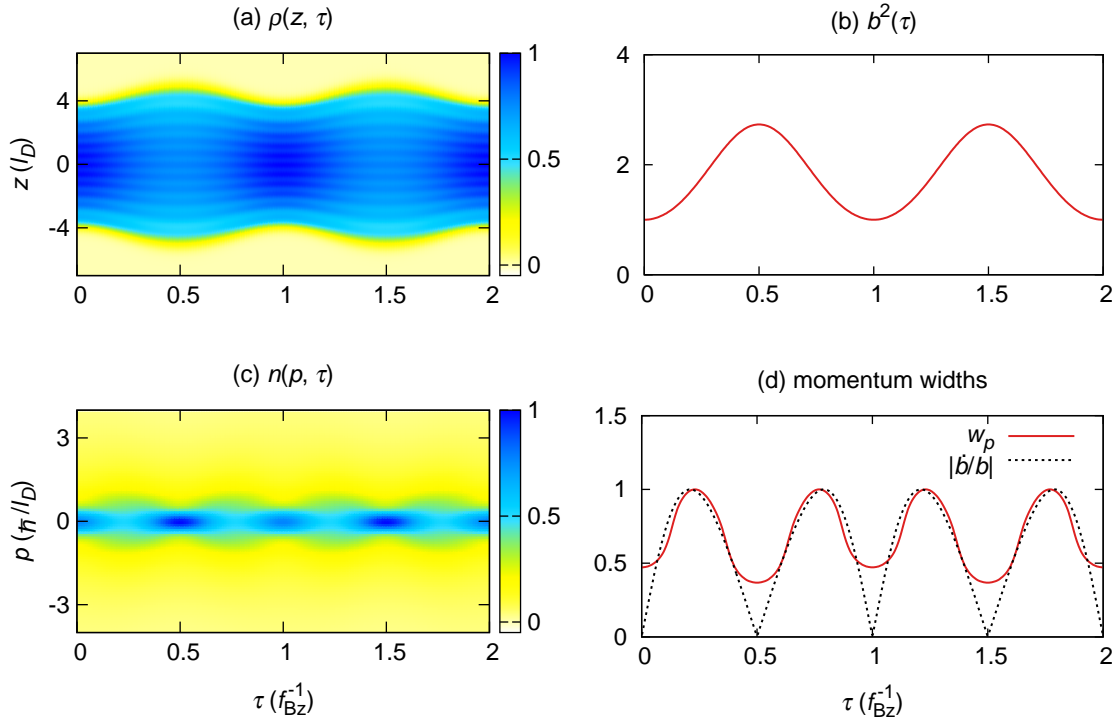


Figure 4.8.: Breathing dynamics in real (top) and momentum (bottom) space. Full profiles (left) and widths (right) are shown. The momentum width predicted by the classical-trajectory assumption ($\propto |\dot{b}/b|$) is included in (d) as a reference. Each picture is normalized to the corresponding maximal signal per pixel. z and p are given in units of their corresponding harmonic length scale $l_D = \sqrt{\hbar/(m\omega_D)}$ and \hbar/l_D respectively. τ is given in units of ω_{Bz}^{-1} . Since the calculation has been performed for one dipole period only, corresponding to a total time of $2/f_{Bz}$, $f_{Bz} = 2f_D$ is implied.

Note however that the spectrum of $w_p(\tau)$ also has a finite contribution at the fundamental harmonic ω_{Bz} , supported by the fact that the local minimal value of w_p is larger at compression points ($f_{Bz}\tau = \text{integers}$) than that at classical turning points ($f_{Bz}\tau = \text{half-integers}$), see Fig. 4.8 (c) and (d). We compute the relative power of the fundamental mode [K in Eq. (4.27), see discussion later] and obtain 0.004 for $\alpha = 1.3$.

One more comment. The time evolution of the kinetic energy ($\propto \langle p^2 \rangle$) in fact

oscillates *sinusoidally* at $2f_D$. This comes naturally from energy conservation arguments, since the interaction energy of a TG gas is *identically* zero. In this sense, the existence of the momentum-space frequency doubling depends on the choice of the oscillatory quantity.

Discussions

A similar collective excitation of a strongly interacting gas has been studied experimentally in [73, 94]. However, neither reports the expected momentum-space frequency doubling. In [94], a different excitation scheme is used, strongly depleting the low-momenta population at the beginning of the oscillations, possibly diminishing the frequency doubling phenomenon. Also, the finite resolution in time may have played a role in this case. In [73], as explained earlier, the measurement is simply not in the far field to access the signature in momentum space.

4.3.1.4. Classical hard spheres: two colliding pendulums

“All models are wrong, but some are useful.” – George Box

At first glance, it may appear difficult to justify the discussion of two colliding pendulums in the context of quantum many-body physics. Yet, learning by analogy has been arguably the most intuitive way for one to grasp a larger, more complex idea. Also, the popular work of [94] precisely makes the analogy between the breathing-like oscillations of cold atomic gases and Newton’s cradle. Thus, a quick look at the motion of two pendulums bouncing off each other may help in our understanding of the breathing motion of a 1D Bose gas.

Physical picture

The crudest analogy of the breathing motion of a 1D Bose gas in the classical world is perhaps the motion of two pendulums in the Newton’s cradle configuration, repeatedly colliding at the lowest point and swinging free when separated. See Fig. 4.9 for an illustration.

A Newton’s cradle usually comes with two strings of equal length per pendulum for suspension, ensuring the motion of the pendulum is confined in a vertical plane. Superposing such planes for each pendulum ensures that the collisions

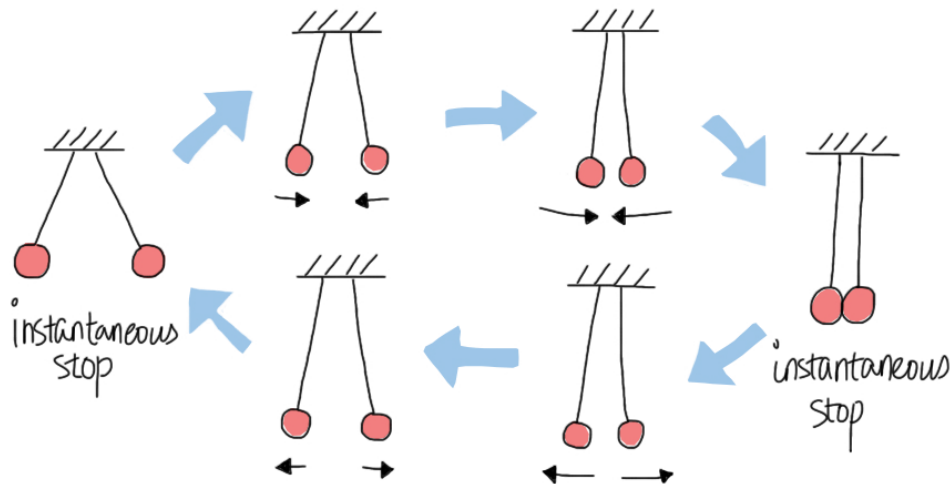


Figure 4.9.: An illustration of the breathing-like motion of two colliding pendulums.

are head on and the trajectories of the pendulums are indeed one dimensional.

Model

To describe such motions, it is crucial to assume the contact takes place over a finite duration of time, otherwise the collision becomes simply a boundary condition in displacement and there is little to learn.

A small amplitude of swing is assumed to recover the motion of a simple harmonic oscillator, whose (Newtonian) equation of motion is well known. Motivated by the fact that the experimentally observed breathing motion does not damp easily, I further assume a conservative interaction potential, e.g. Hertzian elastic contact [1], between the pendulums during the collisions. Such a contact, with the pendulums approximated by solid spheres of uniform material, gives rise to the equation of motion

$$\ddot{d} = -\mathcal{A}d^{3/2}, \quad (4.17)$$

where $d (> 0)$ denotes the linear displacement, while the ‘effective spring constant’⁶ \mathcal{A} depends on the dimensions as well as the material⁷ of the pendulum.

⁶figuratively speaking, since the contact force resembles the restoring force of a displaced spring but obeys a (not too) different power law.

⁷ $\mathcal{A} = \frac{4}{3} \frac{E^* \sqrt{R}}{m_{\text{pend}}}$, where m_{pend} is the mass of a pendulum, R is the effective radius obeying $\frac{1}{R} =$

For a steel pendulum of 1 cm radius, $\mathcal{A} \simeq 3.13 \times 10^{11} \text{ m}^{-1/2}\text{s}^{-2}$, clearly of a drastically different order of magnitude compared to the gravitation-equivalent spring constant $g/l \simeq 196 \text{ s}^{-2}$, where gravitational acceleration is $g \simeq 9.81 \text{ m}\cdot\text{s}^{-2}$, and the length l of the pendulums is (arbitrarily) set to 5 cm. Of course, it is forbidden to even compare quantities of different dimensions, strictly speaking⁸. On the other hand, the disparity in the order of magnitude is essentially the reason why there is no classical analogue of the frequency doubling seen for qBEC and TG gas.

The full trajectories can be computed by stitching up the solution of Eq. (4.17) during the contact and that of a simple harmonic oscillator during the free swing, so that both displacement and velocity of each pendulum are accessible.

Breathing behavior

I plot the trajectories of the two pendulums in real and momentum space in Fig. 4.10 (a) and (c). In order to complete the analogy, I need to define quantities that are equivalent to $\langle z^2 \rangle$ and w_p . This is fortunately easy. Since there are only two pendulums, their trajectories are identical except for the direction, so that d^2 would be equivalent to $\langle z^2 \rangle$ up to an irrelevant constant, and $|d|$ would be equivalent to w_p . I also plot their time evolution in Fig. 4.10 (b) and (d) respectively.

Applying Fourier analysis on d^2 and $|d|$, we measure the equivalent frequencies, $f_{\text{Bz}} = 4.47 \text{ Hz}$, $f_{\text{Bp}} = 4.47 \text{ Hz}$ (of the most dominant frequency component), together with $f_D = \sqrt{g/l}/(2\pi) = 2.23 \text{ Hz}$, we have

$$\frac{f_{\text{Bz}}}{f_D} = 2.00, \quad (4.18)$$

$$\frac{f_{\text{Bp}}}{f_{\text{Bz}}} = 1.00, \quad (4.19)$$

i.e. the momentum-space frequency doubling is absent here. Note that although

$\frac{1}{R_1} + \frac{1}{R_2}$, and E^* is the effective elastic modulus satisfying $\frac{1}{E^*} = \frac{1-\nu_1^2}{E_1} + \frac{1-\nu_2^2}{E_2}$. Here, R_j , E_j and ν_j denote the radius, elastic modulus, and Poisson ratio of each pendulum, with $j = 1, 2$. Both E_j and ν_j are properties of the bulk material, and can be found in standard database. Taking $R_j = 1 \text{ cm}$, $\nu_j = 0.3$, and $E_j \simeq 200 \text{ GPa}$, we obtain $\mathcal{A} \simeq 3.13 \times 10^{11} \text{ m}^{-1/2}\text{s}^{-2}$.

⁸Alternatively, one could preserve the dimension of g/l and consider the combination of $\mathcal{A}d^{1/2}$. Since d is on the order of a few mm, $\mathcal{A}d^{1/2}$ will remain on the order of 10^{10} s^{-2} , and the same arguments follow.

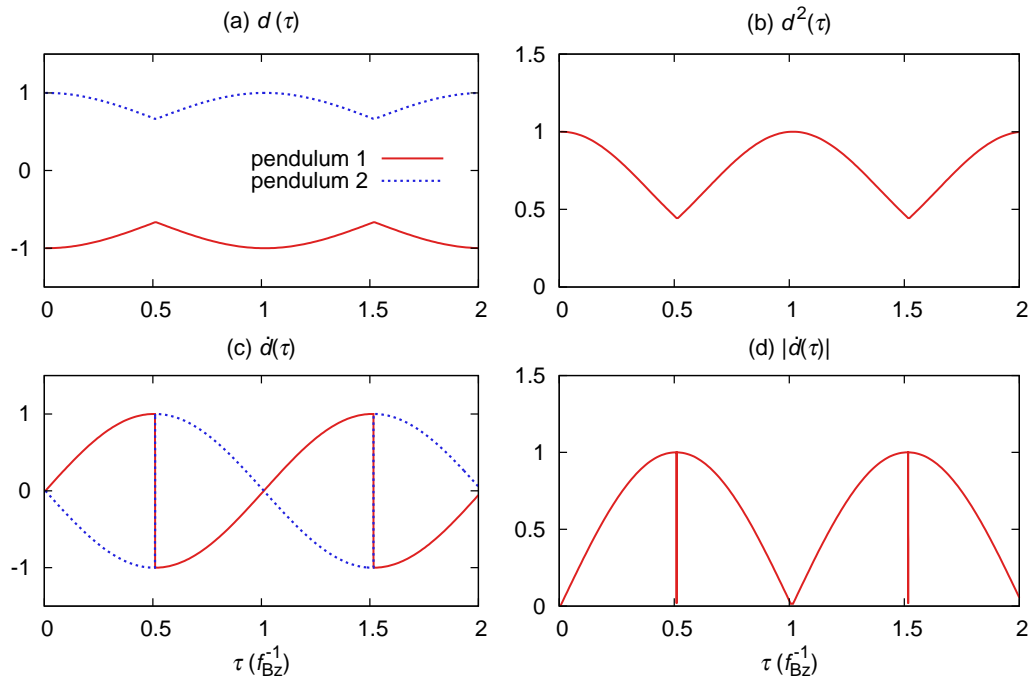


Figure 4.10.: Breathing dynamics of two colliding pendulums. The trajectories in (a) real and (c) momentum space. Both trajectories are normalized to their respective maximal values. I also plot (b) d^2 (equivalent to $\langle z^2 \rangle$) and (d) $|d\dot{d}|$ (equivalent to w_p). Again, one ‘dipole’ period is shown, while the time is shown in units of $1/f_{Bz}$, so that $f_{Bz} = f_{Bp} = 2f_D$.

the properties of materials may differ from one to another, the outcome of the computation does not change much for commonly available materials of decent dimensions.

Discussions

This is a case when despite $|d\dot{d}|$ hits zero twice per ‘breathing’ cycle, the dominant frequency component gives $f_{Bp}/f_{Bz} = 1$, since the ‘self-reflection’ takes place much faster than the gravity-driven classical turning point. There is no reasonable material that would give a bulk contact force that can have a comparable effect as gravity. In other words, the observed self-reflection of ultra-cold atomic gases is a true interaction effect of a microscopic quantum many-body system.

4.3.2. Crossovers

Back in the world of quantum many-body physics, the three limiting cases, namely, qBEC, IBG, and TG gas, are connected by three crossovers. Since no abrupt behavior is expected to occur, it is interesting to investigate quantitatively how variations take place. More precisely, we would like to know,

- How the real-space frequency shift takes place, and
- How the self-reflection mechanism that gives rise to the momentum-space frequency doubling disappears.

Due to the technical limitations on our experiment, only the qBEC to IBG crossover has been accessible, so that the discussions on the other two crossovers are limited to key results summarized from existing studies, as well as possible future developments.

4.3.2.1. Quasicondensate to ideal Bose gas crossover

We probe the qBEC to IBG crossover experimentally by varying the total atom number. The final samples contain about 800 to 8000 atoms typically. For each set of data, an interleaved calibration scan measuring the atom number N_{tot} , the density profile, the fluctuation profile, as well as the momentum distribution are carried out without perturbing the system. The *in situ* density profile thermometry⁹ indicates a temperature of about 100 nK, corresponding to a central chemical potential $\mu_0 \in [0.04, 0.5] \times k_B T$ in a trap of $(f_{\perp}, f_z) \simeq (2000, 7)$ Hz. According to Eq. (1.1), the samples are nearly 1D, while the difference in atom number ensures a range of central interaction parameter γ_0 . $\gamma_0 = 0.004$ is used as a heuristic bound¹⁰ to determine whether $\langle z^2 \rangle$ is obtained by a fit to an inverted parabola ($\gamma_0 < 0.004$) or to a Gaussian ($\gamma_0 > 0.004$). Figure 4.11 shows the region of the (γ, t) phase space explored. Note that the range of t values based on the density profile thermometry is indistinguishable at this point, so that the horizontal line segment encompasses all sets of data used for this study.

⁹We remark that other thermometries as detailed in Ch. 3 are possible, and seem to indicate a lack of true equilibrium. See the discussions later in this section for more details.

¹⁰solely justified by the increasingly significant wings for greater values of γ_0 .

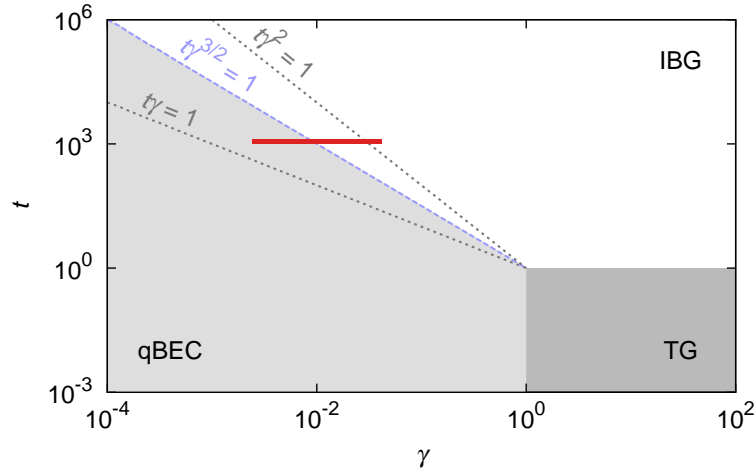


Figure 4.11.: Phase diagram illustrating the region explored by the data sets.

The total duration of the evolution $\tau_{\max} = 500$ ms is kept constant here. The damping does not vary much throughout the entire set of data, and is generally small so that the lifetime cannot be determined precisely. In addition, a small loss¹¹ makes it difficult to ascertain if the damping is due to the intrinsic physical behavior of the system. Therefore, the data here will not be used in the lifetime studies presented in the next section.

The theory treatment consists of two independent and complementary approaches: an exact short-time expansion of the dynamics and a long-wavelength hydrodynamic analysis. The former is microscopic, starting from the equation of motion governing individual constituent atoms. The latter is macroscopic, treating the entire system as a bulk entity. Both take the finite temperature into account, a first to our knowledge. The agreement between these two approaches sheds light on the validity of hydrodynamics as well as on the nature of mass transport in 1D.

Real-space frequency shift

Since the values of t for the data fall within $\pm 10\%$ of their mean, we plot the measured ratio of f_{Bz}/f_D as a function of γ_0 in Fig. 4.12 (top panel). Asymptotic values of $\sqrt{3}$ for qBEC and 2 for IBG are shown as dotted lines as a reference.

Models. Our microscopic model assumes that the system at $\tau = 0$ is at thermal

¹¹of about 15% of the atoms over the course of 500 ms.

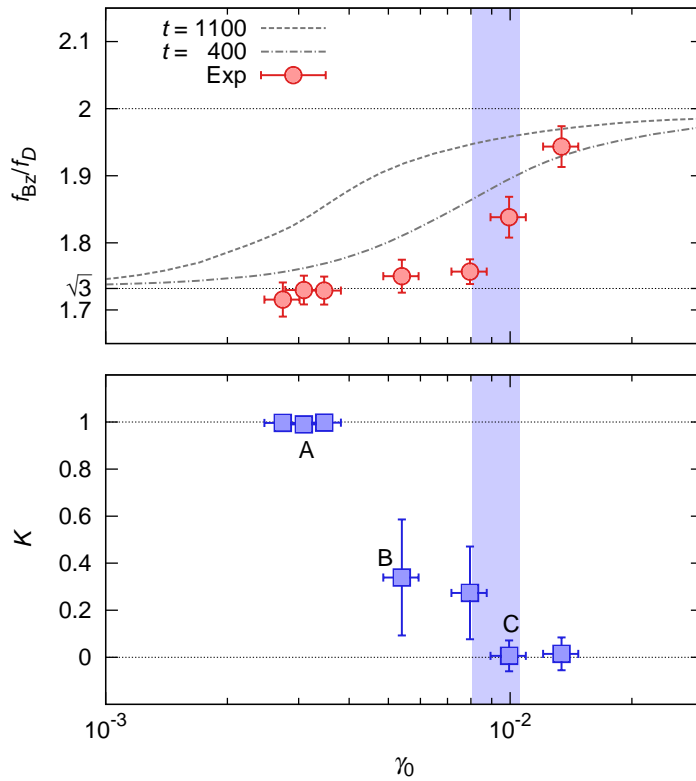


Figure 4.12.: Breathing mode in the qBEC to IBG crossover. Top panel: shift of the breathing frequency in real space. Data (points) are compared with theory predictions at $t = 1100$ (dashed line) and at $t = 400$ (dash-dotted line). Asymptotic values of $\sqrt{3}$ for qBEC and 2 for IBG are shown. Bottom panel: disappearance of the momentum-space frequency doubling. The crossover interaction parameter $\gamma_{\text{co}} \equiv t^{-2/3}$ is shown as the shaded region for $t = 1100$, accounting for a 10% statistical uncertainty on t . Data labels A-C corresponds to the data sets shown in Figs. 4.5, 4.14 and 4.7.

equilibrium with a Hamilton operator

$$H = H_{\text{LL}} + H_{\text{pot}}, \quad (4.20)$$

where $H_{\text{pot}} = \sum_j \frac{1}{2} m \omega_0^2 z_j^2$ is the potential energy in the trap ω_0 . An instantaneous change of trapping frequency from ω_0 to ω_D can be written as

$$\Delta H = (\alpha^2 - 1) H_{\text{pot}}, \quad (4.21)$$

where $\alpha \equiv \omega_0/\omega_D$ gives the quench strength. The short-time expansion of

Heisenberg equation of motion of such an operator can be written as

$$\langle \Delta H \rangle(\tau) = \langle \Delta H \rangle_T - \frac{\tau^2}{2!} \langle C_2 \rangle_T + \frac{\tau^4}{4!} \langle C_4 \rangle_T + \dots, \quad (4.22)$$

where C_2 and C_4 are the second and fourth order nested commutators with the final Hamilton operator $H_f = H + \Delta H$, and the thermal average $\langle \dots \rangle_T$ is taken over the thermal state of H . Assuming $\langle z^2 \rangle (\propto \langle \Delta H \rangle)$ evolves sinusoidally¹² with time at a frequency f_{Bz} , we have

$$\frac{f_{Bz}^2}{f_D^2} = \frac{\langle C_4 \rangle_T}{\langle C_2 \rangle_T} = 4 - \frac{1}{2} \frac{\langle H_{\text{int}} \rangle_T}{\langle H_{\text{pot}} \rangle_T}, \quad (4.23)$$

where $H_{\text{int}} = g_{1D} \sum_{j < k} \delta(z_j - z_k)$ is the interaction part of H_{LL} . The final equality in Eq. (4.23) comes from explicitly working out $\langle C_2 \rangle_T$ and $\langle C_4 \rangle_T$ [24], and taking the limit of an infinitesimal quench amplitude $\alpha \rightarrow 1$, where the sinusoidal approximation is valid. This expression can be evaluated as soon as the energy terms $\langle H_{\text{int}} \rangle_T$ and $\langle H_{\text{pot}} \rangle_T$ are known. In our case, the YY equation of state provides means for numerical computation.

Our macroscopic model starts from the hydrodynamic equations (HDE) [107],

$$\partial_\tau \rho + \partial_z(\rho v) = 0, \quad (4.24)$$

$$m \partial_\tau v + \partial_z \left(\frac{1}{2} m v^2 \right) + \partial_z \left(\frac{1}{2} m \omega_D^2 z^2 \right) - \frac{1}{\rho} \partial_z P = 0, \quad (4.25)$$

where $\rho = \rho(z, \tau)$ and $v = v(z, \tau)$ are the density and velocity fields, and P is the pressure. Since long-wavelength density waves in a fluid are adiabatic¹³, we make the same assumption here. Linearization is justified by the experimental observation that the breathing frequency varies little for α up to 3, so that for a slice of gas at position z , its (small) displacement field $u(z, \tau)$ obeys

$$\partial_\tau^2 u = -\omega_D^2 u + \frac{1}{m\rho} \partial_z \left(\frac{\partial P}{\partial \rho} \Big|_S \rho(\tau = 0) \right) \partial_z u + \frac{\partial P}{\partial \rho} \Big|_S \partial_z^2 u, \quad (4.26)$$

where S denotes the entropy per particle, and the isentropic pressure curve used in $\frac{\partial P}{\partial \rho} \Big|_S$ can be obtained numerically from the YY equation of state. For the com-

¹²which is *exact* in the IBG and TG limit [recall Eq. (4.14)], but only true for $\alpha \rightarrow 1$ in the qBEC limit.

¹³in the sense that there is no heat flow and therefore no entropy exchange.

pression mode, one expects $u(z, \tau) \propto ze^{-i\omega_{Bz}\tau}$, so that the breathing frequency f_{Bz} can be obtained numerically through the crossover. This method extends the analytic work of [107], but now the finite temperature and the crossover are taken into account by means of the numerical equation of state instead of the power-law limits used in the original work.

Discussions. We first verify *a posteriori* that both methods mentioned above yield *identical* results, plotted in Fig. 4.12 (top panel, dashed line) for $t = 1100$. Such an agreement strengthens the applicability of HDE to 1D system, for which the concept of collision time is not well defined¹⁴. Also, it provides an assessment of the nature of the mass transport at finite temperature, which appears to happen in an isentropic way. Moreover, Eq. (4.23) extends the regime of validity of the existing sum-rule approaches, which predicts $f_{Bz}/f_D = \sqrt{2}$, whereas the correct asymptotic limit is $f_{Bz}/f_D = 2$.

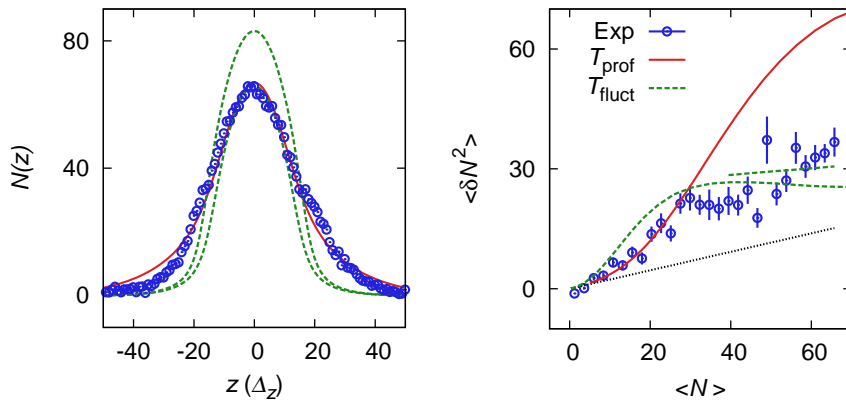


Figure 4.13.: Sample analysis demonstrating a ‘two-temperature’ phenomenon. Both the *in situ* density profile (left) and the atom-number fluctuations (right) are shown. The data (points) are compared with the calculation using $T_{\text{prof}} \simeq 103$ nK (solid lines) and those using $T_{\text{fluct}} \simeq 40$ nK (dashed lines). The Poissonian limit of the atom-number fluctuations is included (right, dotted line) as a reference. The central interaction parameter is $\gamma_0 = 0.008$ for this data set.

On the other hand, the lack of quantitative agreement between the experimental data and our models prompts further investigation. We analyze the calibration scans using the atom-number fluctuation thermometry introduced in Sec. 3.2.2, and find temperatures T_{fluct} about a factor 3 smaller than the corresponding T_{prof} . A sample analysis is shown in Fig. 4.13. Comparing the data points with the

¹⁴The usual validity statement for HDE reads $\omega_D \tau_{\text{coll}} \ll 1$, where τ_{coll} denotes the collision time.

solid line in the right panel, it is clear that T_{prof} overestimates the atom-number fluctuations. On the other hand, the left panel indicates the failure of computing a density profile at T_{fluct} (preserving N_{tot} or $\mu_0 \simeq g_{1D}\rho_0$) that agrees with the measurement. Such a discrepancy seems to suggest that the initial state may not be described by the usual Gibbs ensemble with a single temperature, and is the basis of our investigations that will be documented in Ch. 5. For the moment, we may treat both thermometries as *bounds* of an estimated temperature. By plotting Eq. (4.23) at $t = 400$ (computed from the mean of T_{fluct}) in Fig. 4.12 (top panel, dash-dotted line), we see that indeed the agreement between the experiment and the theory improves.

Disappearance of self-reflection

To address the behavior of the breathing mode in momentum space, we investigate the time evolution of w_p . Since w_p shows a periodic behavior at the frequency ω_{Bz} , it can be expanded in a discrete Fourier spectrum. The relative weights of the Fourier components vary through the crossover, and we obtain quantitative information by fitting w_p with a two-frequency model,

$$w_p = Ae^{-\frac{\tau}{\tau_1}} + Be^{-\frac{\tau}{\tau_2}} \left[\sqrt{1-K} \cos(\omega_{\text{Bz}}\tau) - \sqrt{K} \cos(2\omega_{\text{Bz}}\tau) \right]. \quad (4.27)$$

Here, A is fixed at the average width during the initial cycle, the phase corresponds to a minimal *in situ* width at the beginning of the oscillations. Four fit parameters remain: B gives the initial amplitude of the oscillation, τ_1 and τ_2 give the lifetime of the mean and oscillation, and K gives the (relative) power of the second harmonic.

This model is included as the solid line in the bottom panel of Fig. 4.5, where the second harmonic clearly dominates, and in that of Fig. 4.7, where the first harmonic dominates. It is also possible to find the coexistence of the two modes. Fig. 4.14 shows a data set in the crossover that exhibits such a feature.

Discussions. The relative power of the second harmonic K (points) is shown in Fig. 4.12 (bottom panel) as a function of γ_0 . In qBEC, the second harmonic dominates, as predicted by the scaling solution, and heralds the self-reflection mechanism. In IBG, the first harmonic dominates, as expected for a noninteracting gas where the self-reflection is absent. Both weights vary gradually through the

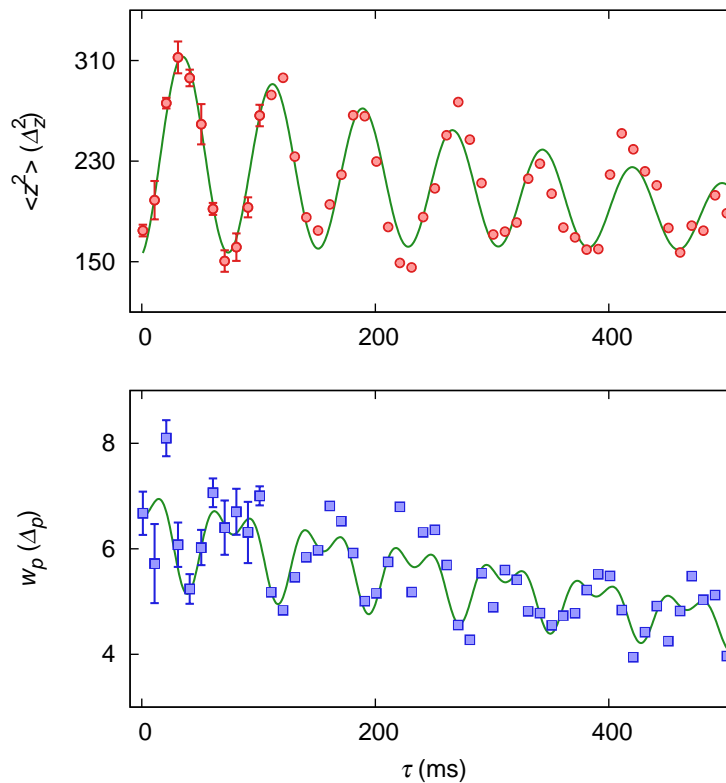


Figure 4.14.: Width variations of a sample in the qBEC to IBG crossover. Data (points) are compared with fits (lines): $\langle z^2 \rangle$ is fitted with a damped sinusoid, whereas w_p is fitted with a two-frequency model [see Eq. (4.27) and related discussion]. The statistical error is shown for the first 100 ms.

crossover, indicating a smooth disappearance of the self-reflection mechanism.

This can be seen as the effect of the breathing mode on the thermally excited Bogoliubov modes of high energy. Their frequency and wave function¹⁵ would be modulated in time, such that w_p is larger at minimal $\langle z^2 \rangle$ (higher density and more thermal fluctuations) than that at maximal $\langle z^2 \rangle$ (lower density and less thermal fluctuations), see Fig. 4.14. The periodicity at $2\omega_{Bz}$ is then broken and the first harmonic at ω_{Bz} emerges.

Figure 4.12 shows that the first harmonic starts to gain weight at a value of γ_0 significantly smaller than that where the frequency shift takes place in real space, so that the disappearance of the second harmonic happens within the qBEC regime.

¹⁵both depend on the instantaneous density profile.

Future work. Quantitative investigation of such a variation in theory is still underway. The main ideas are outlined here.

Given the linearization and weak quench limit used in the modeling above, it appears that we are not far from being *quasistatic*, in the sense that the system is not too far from equilibrium. Indeed, fitting the instantaneous *in situ* density profile to the equilibrium equation of state, we obtain a temperature variation of about 5 nK peak to peak. This, together with LDA, allows the assumption that the overall momentum distribution remains as a weighted sum of the *local equilibrium* momentum distribution with the local density $\rho(z, \tau)$ and at the overall temperature $T(\tau)$. For the width of the instantaneous momentum distribution during the breathing mode, two relevant scales are in play: the local momentum width per slice and the hydrodynamic velocity field. The former undergoes adiabatic compression and rarefaction due to density modulation, and therefore oscillates at ω_{Bz} , while the latter oscillates at $2\omega_{Bz}$, as described in Sec. 4.3.1.1. Numerically working out the instantaneous momentum distribution for a given initial condition allows for the determination of the relative power.

Alternatively, thermal fluctuations in the system can be treated with a classical field approximation, so that numerical methods such as SGPE could be used to simulate the evolution of the momentum distribution. This is currently being discussed with the atom-chip team in Vienna, who has developed the numerics for different purposes but may have an interest in understanding such problems.

4.3.2.2. Quasicondensate to Tonks-Girardeau gas

Real-space frequency shift

This is investigated in the work of [73], where a BEC of cesium-133 atoms are loaded into a 2D optical lattice to create an ensemble of 1D systems. The interaction is adjusted by a Feshbach resonance that changes the 3D *s*-wave scattering length of the atoms. The real-space breathing frequency is measured and used to identify the thermodynamic regime of the system from IBG to qBEC and then to TG. As an illustration, Fig. 4.15 reproduces two of the key figures from their publication [73].

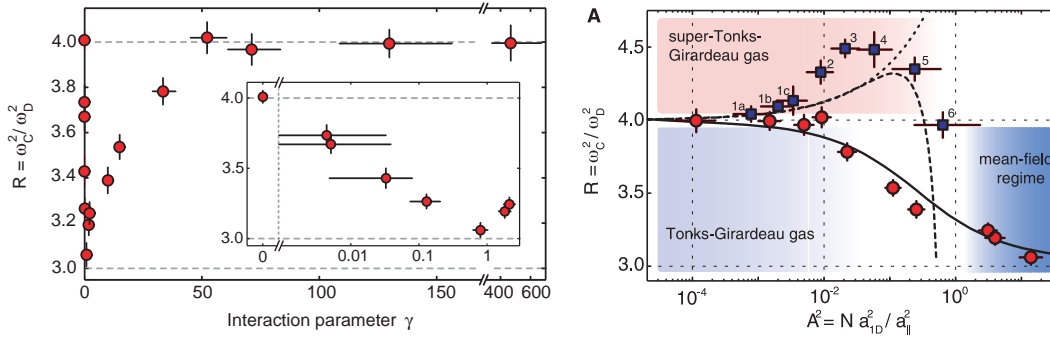


Figure 4.15.: Reproduction of Fig. 2 (left) and Fig. 3A (right) of [73]. The authors measured the squared frequency ratio between the compression (breathing) mode and the dipole mode R as a function of the interaction parameter γ (left), and demonstrated excellent agreement with the zero-temperature theory (right: circles vs solid line) according to [107].

Since the thermal fraction of the system is small, the authors essentially probe a zero-temperature system, which demonstrates excellent agreement with the theory based on sum rules [107].

Disappearance of self-reflection

Such a phenomenon is not expected here, since both limiting cases exhibit the momentum-space frequency doubling. An experimental verification requires the capability to tune the interaction strength, to reach the strongly interacting TG regime, and to image in momentum space. Reported experiments often meet some of these conditions but never all to my knowledge, so that such a study has yet been performed.

Theoretically, the methods outlined in the previous section under the heading of 'Future work' could in principle be applied here. Such a numerical task is unfortunately out of the scope of the current manuscript and will not be discussed further.

4.3.2.3. Tonks-Girardeau to ideal Bose gas: a toy model and a perspective

The crossover from TG to IBG regimes has yet to receive much attention in the context of the breathing mode, and understandably so, since one expects the same

asymptotics $f_{Bz}/f_D = 2$ for both cases. Our understanding of the self-reflection mechanism would hopefully renew some interest in this topic, since the exact solution of a TG gas (see Sec. 4.3.1.3) predicts a momentum-space frequency doubling that is absent in the IBG limit. I outline some theory tools that could be useful for such an investigation.

Two atoms in a harmonic trap: a toy model. This is in fact an exactly solvable model with any interaction strength. The seminal work of Busch *et al* [23] has given the recipe to construct all eigenstates for the relative wave function, so that the full spectrum of the system is known. The finite temperature can be taken into account by considering the statistical operator of a thermal state. The evolution dynamics after a quench of the trapping potential can then be computed, up to a cutoff that determines how many states are taken into account.

Exact diagonalization. This method aims at diagonalizing the many-body Hamilton operator, and therefore is able to tackle the problem with more than two atoms. A typical implementation uses the harmonic oscillator basis, so that the interaction part contains the off-diagonal elements. Depending on the strength of the interaction, an appropriate energy cut-off can be placed and the diagonalization is then performed numerically. Similar to the case of two atoms, one again obtains the full eigenstates and the evolution dynamics can be computed. This method has been used to compute properties of a handful of spinor bosons in [42] up to the strongly interacting limit, and the convergence at large values of g_{1D} is tested.

High-temperature TG gas. A recent article has demonstrated the possibility to compute the exact momentum distribution of a thermal TG gas [152]. Together with the scaling solutions, this constitutes a promising way of investigating the disappearance of the self-reflection mechanism within the TG regime.

4.4. Lifetime studies

The experiments performed to investigate the frequency behavior in the qBEC to IBG crossover (see Sec. 4.3.2.1) have also revealed remarkably large values of

lifetime¹⁶ of the breathing mode. We believe that it is related to the 1D nature of the system, in particular, the integrability of the underlying LL model, despite a small population in the transverse excited states. Indeed, the decay of collective oscillations in 3D systems is associated with the Landau damping mechanism [50, 87]. A blind application of a similar calculation would yield lifetime values significantly below those observed. The microscopic theory model based on the Heisenberg equation of motion can take into account higher order terms in the short-time expansion, and appears promising to describe the system. This is currently under development. I summarize the key results on the experiment below.

For the data presented below, the experimental procedure is the same as those described in Sec. 4.2.2, except that the total duration τ_{\max} is now extended to a range between 700 ms to 900 ms, eventually limited by a typical cycle duration without affecting the loading condition¹⁷. Calibration scans were carried out as before and the lifetime is obtained by fitting $\langle z^2 \rangle$ with a damped sinusoid. The fitted values of the lifetime τ_{Bz} and of the breathing frequency f_{Bz} then yield the quality factor $Q_{\text{Bz}} \equiv 2\pi f_{\text{Bz}} \tau_{\text{Bz}}$. Another parameter of interest is the fractional population in the transverse excited states $N_{\text{TE}}/N_{\text{tot}}$. This can be obtained directly by computing the transverse ground-state population at the profile temperature, i.e. $N_{\text{YY}} = \sum_z \Delta_z \rho_{\text{YY}}(z, T_{\text{prof}})$, and then use the identity $N_{\text{tot}} \equiv N_{\text{YY}} + N_{\text{TE}}$ according to Eq. (2.23).

These samples have a temperature $t \in (1170, 2650)$, and a central interaction parameter $\gamma_0 \in (0.0019, 0.0034)$. There is no obvious disagreement between the profile thermometry and the atom-number fluctuation thermometry. However, the very notion of the 1D interaction parameter becomes questionable, since $N_{\text{TE}}/N_{\text{tot}} \in (15\%, 71\%)$ is no longer negligible. Therefore, we use $N_{\text{TE}}/N_{\text{tot}}$ as the independent parameter in Fig. 4.16. In the top panel, we see that the mapping between t and $N_{\text{TE}}/N_{\text{tot}}$ is nearly linear. The values of f_{Bz}/f_D are shown in the middle panel, with the 1D qBEC limit at $\sqrt{3}$ plotted in dotted line as a reference. Most data points fall just below this limit, indicating that the 3D effects start to

¹⁶The exponential fit over 500 ms of oscillation gives lifetime values on the order of a second. More precise determination of the (large) values of lifetime therefore requires measurements at longer evolution time.

¹⁷Longer cycle time affects the loading rate, which in turn affects the efficiency of the cooling sequence. For practical purposes, therefore, the total duration (~ 20 s) of the sequence is chosen and all preparation steps are optimized at this value.

play a role in the dynamics of the system. However, the true 3D qBEC limit is at $\sqrt{5/2} \simeq 1.581$, so that our samples are far from behaving like a true 3D system. Finally, Q_{Bz} is shown in the bottom panel. The data span more than one order of magnitude of Q_{Bz} , showing a clear monotonous correlation with the fractional population in the transverse excited states (and thus with the temperature).

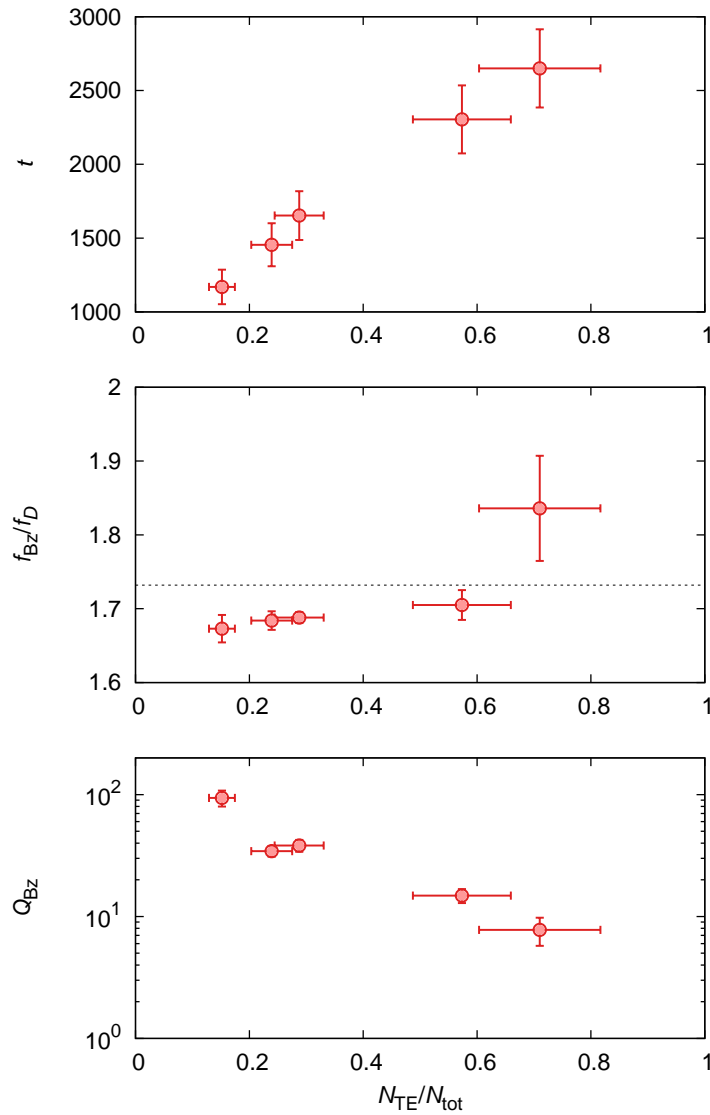


Figure 4.16.: Lifetime studies of the breathing mode of a nearly 1D gas. The top panel indicates a nearly linear dependence between t and N_{TE}/N_{tot} . The middle panel plots f_{Bz}/f_D , with the 1D qBEC limit shown as the dotted line. Q_{Bz} is plotted in semilog scale in the bottom panel.

Conclusions

In this chapter, we have seen a joint theoretical and experimental investigation of the breathing mode of 1D Bose gases.

The study of the breathing frequency attempts to cover various regimes of the 1D phase diagram spanned by the interaction parameter and the reduced temperature.

- **Breathing frequency in real space.** We reproduce the breathing frequency expected in the three limiting cases, the IBG, qBEC and TG gas, as well as in the qBEC to IBG crossover, and we propose finite-temperature models to compare with our experimental data. The qBEC to TG gas crossover is reviewed, and we propose a few theoretical tools that will allow the investigation in the TG gas to IBG crossover.
- **Self-reflection mechanism.** The experimental investigation of the breathing frequency in momentum space in the qBEC to IBG crossover has led to the very first demonstration of an interaction-induced self reflection mechanism, which is observed as a momentum-space frequency doubling. This mechanism is also to be expected in the TG regime according to the exact solutions of the TG gas at zero temperature. There is no known theoretical frame work that describes the disappearance of the self reflection. Potential candidates are discussed as future works.

The study of the breathing lifetime is purely experimental at this stage. The data lie mainly in the 1D-3D dimensional crossover. For qBEC whose breathing frequency in real space remains more or less constant ($f_{Bz} \simeq 1.7f_D$), the quality factor varies by one order of magnitude when the population in the transverse excited states are increased from about 15% to 60%. Theoretical investigations in collaboration with Dr. Giuseppe Carleo are ongoing.

A two-temperature phenomenon is observed as a by-product, and its investigation is detailed in the next chapter.

5. Long-lived Nonequilibrium States

Contents

5.1. Motivation	96
5.2. Experiments	96
5.2.1. Experiment 1: let's wait and see	98
5.2.2. Experiment 2: adjusting the evaporation parameters	100
5.3. Discussions	103
5.4. Future developments	105

In this chapter, I present some experimental studies aimed at investigating long-lived states produced at the end of the evaporative cooling that cannot be described by a Gibbs ensemble. Such states have been repeatedly observed on our experimental setup. Although the cause is unclear, we believe that these states are produced as a consequence of crossing from a 3D regime where thermalization processes are fast and well understood [104], to a 1D regime where the underlying LL model is integrable and its thermalization is currently under investigation by various groups and means [66, 94, 100]. I will document the measurements carried out and discuss about the empirical observations. Theoretical understanding from first principles is yet to be developed.

I organize this chapter as follows. In Sec. 5.1, I discuss the motivation of this study. Section 5.2 presents the two experiments carried out and their respective outcome. I then discuss the implications of our finding in Sec. 5.3, followed by an outlook of potential future developments along this direction in Sec. 5.4. Some concluding remarks are presented at the end.

5.1. Motivation

The motivation of such a study is three fold.

First, the persistence of such non-Gibbs states directly impacts the outcome of experiments performed on our setup. For example, in the studies of the breathing mode presented in Ch. 4, the apparent ‘two-temperature’ phenomenon makes precise and quantitative comparisons between our measurements and theory models difficult. The appearance of such states is empirically related to the failure¹ of momentum profile thermometry, and occasionally that of the density profile thermometry. A characterization and hopefully a full understanding of such states are therefore desirable.

Second, the thermalization of 1D gases is a long standing and interesting problem by itself, and requires further investigation in order to clarify the relevant physics behind. Some of the recent publications (e.g. [66, 100]) present significant efforts made in this direction, although the subject is far from being well understood. By investigating the production and evolution of the non-Gibbs states that we observe, we hope to understand if thermalization processes would eventually lead to the disappearance of such states.

Third, quantum many-body systems in 1D have been studied experimentally by many teams in the community of ultracold atomic gases. Discussions with various colleagues in the field have lead to us realizing that our experimental setup is not alone in producing states which are not well described by Gibbs ensemble at equilibrium, despite the acclaimed isolation and degree of control possible. It is therefore interesting to document our observations in order to facilitate possible comparisons across different experiments.

5.2. Experiments

Two experiments will be documented below. The first is a simple ‘wait and see’ protocol, verifying that the resultant nonequilibrium state survives time and

¹in the sense that the fit routine tend to yield a profile that agree poorly with data.

losses. In the second experiment, we vary the evaporation parameters in the hope to associate the rate of evaporation to the extent of lack of equilibrium in the system.

Two of the probes described in Ch. 3 are used: the *in situ* density profile thermometry, which gives a profile temperature T_{prof} , and the atom-number fluctuation thermometry, which gives a fluctuation temperature T_{fluct} . The justification of such a choice is purely pragmatic. Both methods have been developed some time ago on our experimental setup and their reliability is time tested. On the contrary, the thermometry based on the measurement of momentum distribution is sensitive to the imaging setup², and often yields a poor fit when the two above mentioned thermometry methods do not agree with each other³. The quantitative understanding of the momentum correlation measurements is being developed right now. The density-ripple measurement has been only recently implemented. Fine adjustments and further consistency checks are needed before it can yield trustworthy results on our setup. Last but not least, to gather information using all the probes available would require about 5 hours of data acquisition time for each experimental condition. Slow drifts render such a brute-force approach tedious if not impossible altogether.

I remark that the evaporation is carried out in such a way that there is minimal residual breathing mode induced. Indeed, it is possible to induce a breathing oscillation if the final trap depth becomes comparable to or smaller than the chemical potential or the evaporation takes place too fast for a simultaneous density redistribution. Given the usually long lifetime of such collective oscillations of a (nearly) 1D system, as seen in the previous chapter, there would be little hope to reach an equilibrium state. Therefore, we made sure for the experiments documented below that the residual breathing motion is barely visible if any, in both real and momentum space. This way, we rule out the breathing mode as the obvious cause of the nonequilibrium state produced.

²Factors such as the imaging resolution, a slight misalignment between the probe beam and the transverse direction of the cloud, imperfections in implementing the focusing technique, all contribute to degrading the imaging quality. Although our understanding and control have improved over time, existing data are of varying quality and a fair comparison is not possible at the time being.

³Note that Ref. [84] indeed presents data sets where a fair agreement is seen between the thermometries based on the measurement of the atom-number fluctuations and that of the momentum distribution. However, this does not occur deterministically and post selection is necessary in order to find such an agreement.

5.2.1. Experiment 1: let's wait and see

Experimental procedures

Such a naïve approach is of course motivated by the hope that should the system thermalize within time scales allowed by the experiment, any discrepancy in temperatures obtained by different probes would eventually diminish or even disappear⁴. Experimentally, we then perform an interleaved calibration scan that measures both the *in situ* density profile and atom-number fluctuations at different values of the waiting time up to ~ 1 s after the end of the evaporation. Note that here the preparation sequence is kept unchanged, and the data sets are acquired within a few days so that the variation in the initial loading condition, empirically observed as a sensitive factor, is minimal.

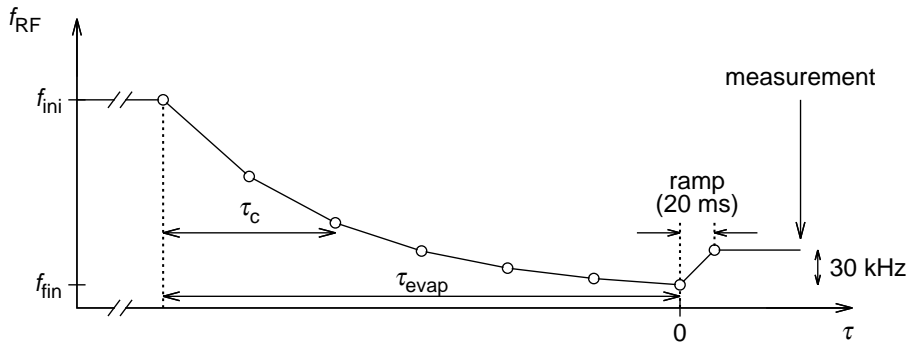


Figure 5.1.: Sequence of RF frequency through and after the final evaporation stage. The evaporation consists of six linear ramps that approximate an exponential decrease. After the evaporation is complete, the RF frequency is raised by ~ 30 kHz in ~ 20 ms in order to terminate the evaporation while allowing the energetic atoms produced by three-body collisions to escape. The end points of the ramps are represented by empty circles.

The final cooling phase that employs radio-frequency (RF) assisted evaporation (in the modulated guide) is carried out via a six-piece frequency ramp at constant power, see Fig. 5.1 for an illustration. The frequency ramps are piece-wise linear, and the values approximate an exponential decrease, with a total duration $\tau_{\text{evap}} = 900$ ms and a time constant of $\tau_c = 300$ ms. The Rabi frequency is not measured on this experiment, and the amplitude is historically adjusted so that one may efficiently evaporate from a thermal gas into a Thomas-Fermi density profile. We further verify experimentally that up to $\pm 20\%$ change in the RF

⁴After all, there are occasions when both thermometries yield comparable results.

power does not result in any apparent change of measured results. During the waiting time, a shielding RF field is kept at the same power ~ 30 kHz above the final value of the cooling sequence, so that energetic atoms produced by three-body collisions may escape without heating the system [128].

Results

The observed temperatures as a function of the waiting time are shown in Fig. 5.2 (top). The uncertainty of T_{prof} is estimated by the standard deviation of the fit temperature using ~ 25 single-shot density profiles. The uncertainty of T_{fluct} could in principle be estimated using the correlation between neighboring pixels⁵ [82]. However, this method appears to fail for the data presented here, possibly due to the fact that the system is not at equilibrium to begin with. We set by hand the RMS diffusion length⁶ $\delta_z = 3 \mu\text{m}$, corresponding to an imaging reduction factor $\kappa = 0.246$ [83]. The two temperatures do not converge on the time scale of the experiment.

We show samples of the density profile and of the atom-number fluctuations for two sets of data in Fig. 5.3. We see that the fit procedure yields density profiles that agree fairly well with the data, despite the apparent disagreement between the two thermometry methods. Also, there is little qualitative difference in the performance of both thermometries.

The atom loss during the waiting time is small ($\sim 30\%$ over the course of 1 s) and does not appear to induce dramatic changes in observed temperature values. We show both the measured total number of atoms N_{tot} and the number of atoms in the transverse excited states N_{TE} predicted by the MYY model at T_{prof} in Fig. 5.2 (bottom). The uncertainty of N_{tot} is given by the statistical fluctuation over ~ 25 shots of atom-number calibration scans, while that of N_{TE} is estimated using the uncertainty of T_{prof} .

Thus, it appears that we obtain a long-lived state that cannot be described by the usual Gibbs-ensemble equilibrium with a uniquely defined temperature.

⁵We use the first and second neighbor for this purpose, since we do not resolve the typical correlation lengths in our system. Recall that the pixel size $\Delta_z = 2.7 \mu\text{m}$, and the healing length $\xi \simeq 0.4 \mu\text{m}$ for a linear density of $\rho = 200$ atoms/ Δ_z .

⁶based on previous data with similar imaging parameters and statistics.

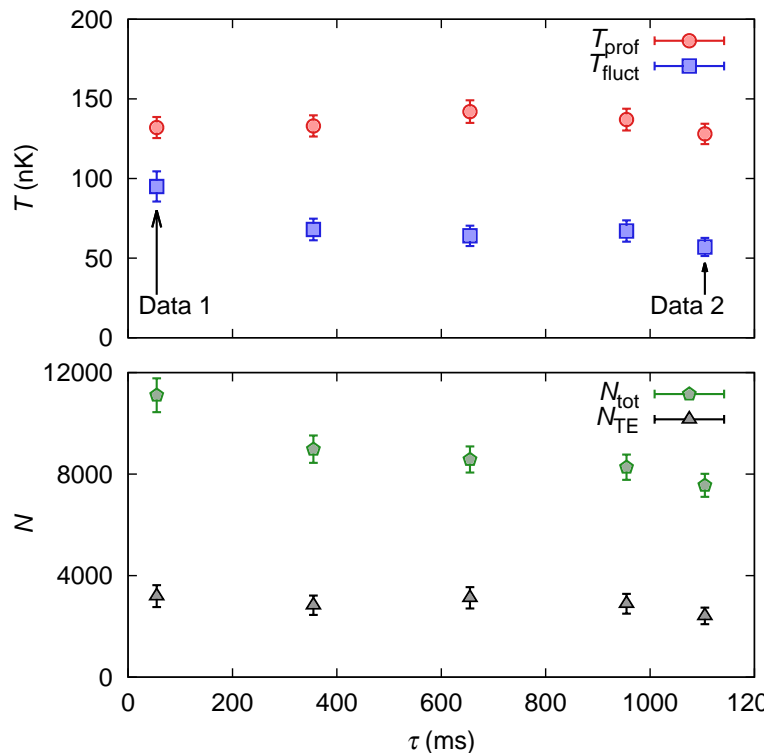


Figure 5.2.: Evolution of the ‘two-temperature’ phenomenon vs the waiting time. Top: Profile temperature T_{prof} and fluctuation temperature T_{fluct} as a function of the waiting time. Bottom: the corresponding atom numbers N_{tot} and N_{TE} . The data labels correspond to the samples presented in Fig. 5.3.

5.2.2. Experiment 2: adjusting the evaporation parameters

Experimental procedures

Since the observed temperatures do not appear to converge upon waiting in the previous experiment, more dramatic measures may be necessary to induce some variation in their behaviors. As a first attempt, we vary the time parameters of the evaporation in order to do so. In particular, we change the evaporation duration τ_{evap} and exponential time constant τ_c , while keeping $\tau_{\text{evap}}/\tau_c = 3$, and perform interleaved calibration scans about 15 ms after the evaporation.

The initial RF frequency f_{ini} is kept constant. Ideally, one would prefer to keep the final frequency value constant as well, so as to study the impact of the time parameters only. However, this is problematic for practical reasons. Indeed, the rate and the efficiency of evaporation are so dramatically different for the regimes

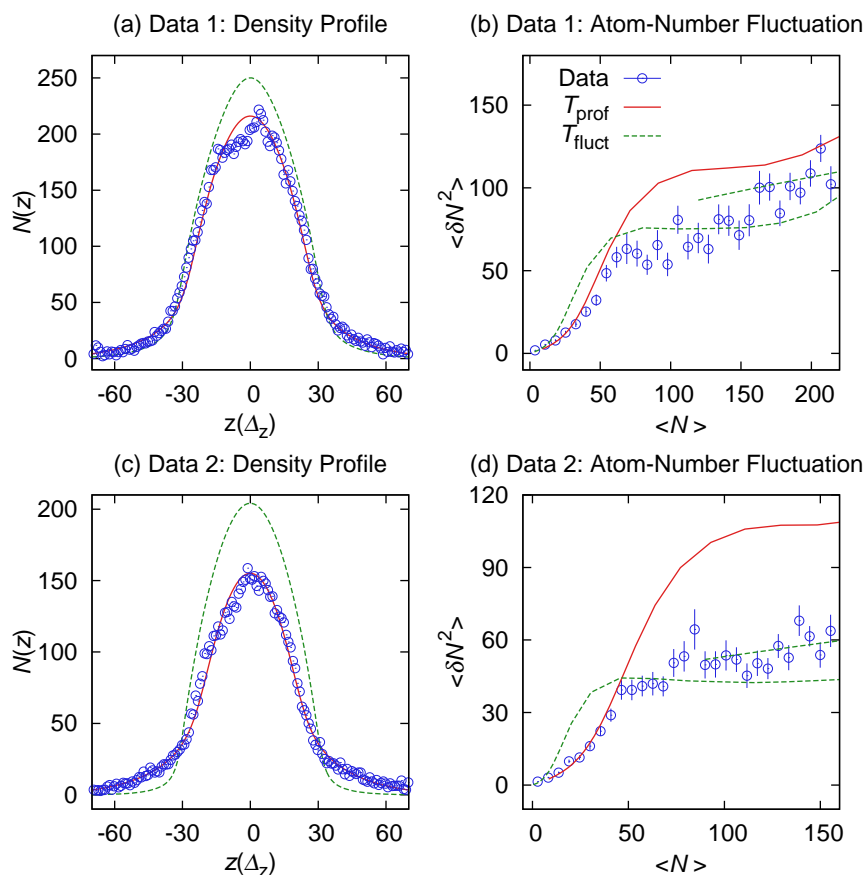


Figure 5.3.: Both the density profile (left) and the atom-number fluctuations (right) are shown for two data sets. Data (points) are compared with theory predictions at T_{prof} (solid lines) and those at T_{fluct} (dashed lines). All theory curves are computed from MYY equation of state. The straight lines are the linearization of Eq. (2.20), the equation of state for qBEC. The samples correspond to those labeled in Fig. 5.2.

explored that one would end up with a final dynamic range of linear density that is beyond the capability of the current imaging set up⁷. Thus, the final RF frequency value f_{fin} is decreased so that N_{tot} is approximately preserved instead.

Results

The observed temperatures as a function of the evaporation time constant τ_c are shown in Fig. 5.4 (top). We see that the disagreement between T_{prof} and T_{fluct} does not improve as the rate of evaporation is varied. On different occasions, longer τ_c up to 600 ms is attempted, and the ‘two-temperature’ phenomenon per-

⁷recall that too high an optical thickness would eventually render the calibration of N_{tot} inaccurate.

sists. However, these data set start from a different initial condition⁸ before the evaporation, making direct and quantitative comparisons difficult.

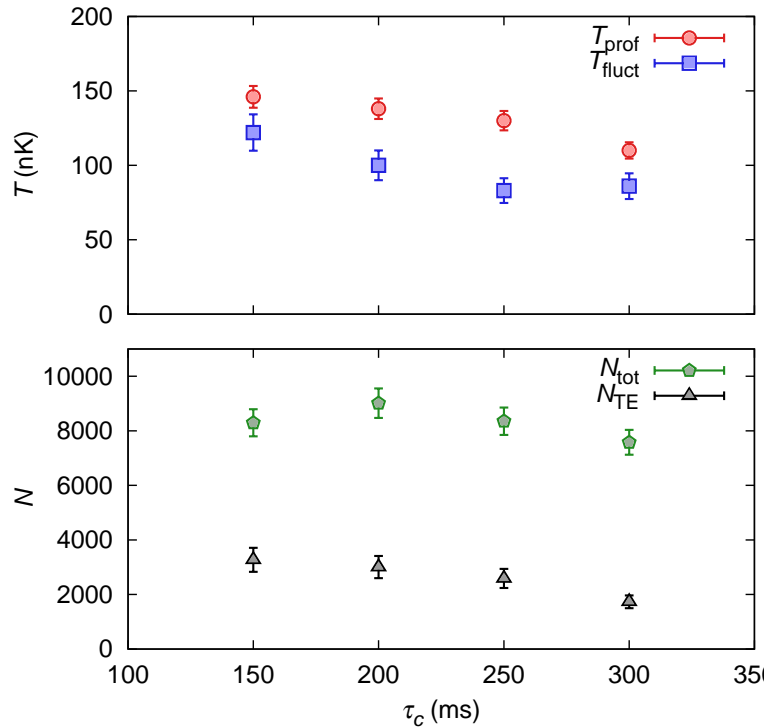


Figure 5.4.: Variation of the ‘two-temperature’ phenomenon as a function of the evaporation time constant τ_c . Top: Profile temperature T_{prof} and fluctuation temperature T_{fluct} as a function of τ_c . The total duration of evaporation is always kept at $\tau_{\text{evap}} = 3\tau_c$. The final RF frequency f_{fin} is gradually decreased for longer durations of the evaporation in order to stay within parameters allowed by imaging. Bottom: The corresponding atom numbers N_{tot} and N_{TE} for the data sets.

The variation of both N_{tot} and N_{TE} are included in Fig. 5.4 (bottom). As intended, N_{tot} remain almost constant, while N_{TE} is seen to decrease as the evaporation is made slower. Since the final frequency of the RF field is constant, it is difficult to conclude if there is a causal relation between the decrease of N_{TE} and the increase of τ_c .

Thus, it appears that the ‘two-temperature’ phenomenon is robust under the variation of the evaporation rate.

⁸due to drifts of the experiment over the time scale of a few days

5.3. Discussions

Technical artefacts. When the cause of such non-Gibbs states is unclear and uncontrolled, it is never too prudent to rule out possible technical artefacts.

Potential rugosity, a common issue in atom-chip experiments, is ruled out in the measurement of T_{fluct} via the sorting and binning of the atom-number fluctuations in data analysis (see Sec. 3.2.2). The measurement of *in situ* density profile may still suffer from such an artefact. However, since the modulated guide removes any rugosity caused by imperfect current-carrying wires, the only remaining factor is the bump in potential created by Rb atoms that are adsorbed on the gold mirror near the usual trap position⁹. Fortunately, the profile fit routine may exclude the affected region and the T_{prof} obtained differs no more than $\sim 2\%$, so that it is insufficient to explain the discrepancy between T_{prof} and T_{fluct} .

For experimental conditions that are more 3D, i.e. when there is a significant population in the transverse excited states, the MYY model may fail, rendering the profile fit problematic. The MYY model assumes a purely 1D transverse ground state with an equation of state $\mu = g_{1D}\rho$, and the transverse excited states obey the IBG equation of states. At high linear densities, such an assumption is in disagreement with the heuristic qBEC equation of state $\mu = \hbar\omega_{\perp}(\sqrt{1+4\rho a} - 1)$, which is known to work well for a qBEC in the 1D-3D crossover. However, the two-temperature phenomenon that we observe is not limited to samples with high linear densities, so that such a conjecture is again insufficient to explain our observations.

Therefore, the prime suspect in our case is the RF side bands that are present as a consequence of the current modulation in the transverse confinement. Since this is specific to our setup, we cannot rely on the experience of others for comparison.

As explained in [82], the joint effect of an AC current in the modulated guide at a frequency f_{MG} (currently at 200 kHz) and of a weak monochromatic RF field at f_{RF} can be seen as an effective carrier RF field with (weaker) side bands at

⁹Note that the atoms are approximately $4 \mu\text{m}$ above the chip surface. Compared to $\gtrsim 100 \mu\text{m}$ as typically realized on other experiments, our setup is far more sensitive to the adverse effects of Rb deposition.

$f_{\text{RF}} \pm f_{\text{MG}}$. As a result, it is possible to evaporate in several windows of the carrier frequency, with expectedly different efficiencies. Historically, both the power and carrier frequency are experimentally determined so that the evaporation is efficient. However, the extent of the ‘two-temperature’ phenomenon (quantified by, e.g., the ratio $T_{\text{prof}}/T_{\text{fluct}}$) differs depending on the choice of the window. For experiments recorded in this chapter, the window of $f_{\text{RF}} \in (1 \text{ MHz}, 1.2 \text{ MHz})$ is chosen for evaporation so that the ‘two-temperature’ phenomenon is minimal if not absent. Nevertheless, in order to completely rule out current modulation as a possible cause of the non-Gibbs state observed, it may be necessary to perform tests in a modulated guide with a higher f_{MG} or in a static trap. This presents a possible extension of the current study.

A possible physical cause. Suppose the presence of two apparent temperatures is indeed physical, we propose a possible cause of such a phenomenon. Since the nearly 1D samples are obtained by forced evaporation starting from a hot and elongated 3D cloud of atoms, the reduction of dimensionality may have prevented some of the loss-induced excitations from thermalizing completely once the nearly 1D (and integrable) regime is reached.

In order to verify this hypothesis, one would ideally wish to know the *initial* conditions before the final evaporation stage. This is not yet implemented for technical reasons¹⁰. We could however look at the *final* conditions, e.g. the dimensionless parameters of the samples obtained. The two-temperature phenomenon investigated here seems to occur, although not deterministically nor controllably, for $t\gamma_0$ on the order of 1 to 10, as the case of the data discussed in Refs. [9, 84], as well as those presented in this thesis (in the last and the present chapters). Systematics are yet to be found in this parameter range. For larger values of $t\gamma_0$ (say around 15 or above), the samples are generally hot and ideal Bose gas like, so that no saturation is expected in the atom-number fluctuations, and little discrepancy is observed between the two thermometries. For $t\gamma_0 \lesssim 1$, as in the data presented in Ref. [83], the atom-number fluctuations strongly saturate, and the two thermometries also tend to agree.

Further investigation and verification of such a hypothesis is of course necessary, and would be particularly interesting in the parameter range where the system-

¹⁰Since the samples are much hotter and denser, the usual imaging methods fail to determine the absolute atom number accurately, rendering it difficult to perform thermometry

atics are unclear.

5.4. Future developments

Going forward, we envision several developments in this direction.

- Technical artefacts such as the effect of current modulation should be quantified, although the current consensus within the team is that this may not explain the observed two temperatures.
- Continuing to use the existing probes, one may wish to perform tests that vary other parameters during evaporation, in the hope of finding a ‘control knob’ that tunes the extent of the ‘two-temperature’ phenomenon. Along the way, it may be necessary to expand the dynamic range of the current imaging system in order to perform tests in a more controlled manner.
- The consolidation of new probes such as the measurement of density ripples and momentum correlation could potentially reveal further information of the non-Gibbs state observed. After all, different probes can be seen as tests of thermal equilibrium with different stringency. A system that ‘passes’ some of these tests but ‘fails’ the others could potentially shed some light on the nature and severity of the tests.
- Theoretical investigation of the cooling process through the 3D to 1D crossover may also shed light on the understanding of our observations.

Conclusions

In this chapter, we have seen that a long-lived state that is not described by a Gibbs ensemble with a unique temperature is regularly obtained on our experimental setup. Two drastically different temperature values can be ob-

tained from the profile thermometry and the atom-number fluctuation thermometry. Such a 'two-temperature' phenomenon is robust against waiting and against the variation of the evaporation rate. It is not likely caused by technical artefacts, but could be a consequence of evaporating through the 3D-1D dimensional crossover. Further theoretical and experimental investigations are needed in order to fully understand the mechanism behind.

6. Modifying the Interaction Strength

Contents

6.1. Motivation	108
6.2. Experiments	109
6.2.1. Modulation	109
6.2.2. Abrupt changes	113
6.2.3. Ramp	116

By now, we have gathered some ideas about the non-Gibbs initial states that we often produce, as well as the evolution dynamics of the system excited into a breathing mode, the lowest lying nontrivial collective excitation. We are now ready to embark on the investigation of the dynamics of a system when we bring it even further away from equilibrium.

In this chapter, I document three kinds of experiments performed in this spirit by means of controlling the interaction parameter g_{1D} . This is achieved by controlling the amplitude of the current in the modulated guide, which in turn controls the transverse trapping frequency and thus the scattering processes that it mediates [113].

Similar to the previous chapter, the results presented here are again of preliminary character, as the investigation is mostly experimental, and the theoretical understanding of the subject matter is still on-going.

I organize this chapter as follows. I will first discuss about the motivation in Sec. 6.1. Details of three experiments are then presented in Sec. 6.2 including

the experimental procedures, the preliminary results and an outlook for each of them. A conclusion is given at the end.

6.1. Motivation

Ultracold atomic gases constitute one of the prime systems for the study of quantum field theory, which predicts the generation of pairs of elementary excitations due to the parametric amplification of the zero-point noise whenever there is a change of boundary conditions (see [25] and references therein). This is known as the dynamic Casimir effect, and the observation of its acoustic analog has recently been reported in [85]. The change of boundary conditions can be implemented by the change of interaction strength (via the change of the confinement and/or scattering length), and the propagation of the excitations in spatially and temporally inhomogeneous systems can be used to simulate quantum field physics on a generic curved space-time.

In a 1D bulk system, the evolution is further complicated by the underlying integrable model (the Lieb-Liniger model), and the lifetime of elementary excitations may provide information about if and how a 1D system relaxes and thermalizes. This problem lies in the intersection of quantum physics and statistical physics, and has received much attention in recent years when quantum simulation of this problem with ultracold 1D Bose gases becomes possible.

On our experiment, the change of the interaction strength can be achieved by modifying the transverse confinement. The independence between the transverse and longitudinal confinement enables a clean realization of interaction modulation, quench and ramp. Although the initial state may not be at thermal equilibrium, the resultant highly nonequilibrium state will likely dominate the subsequent evolution. The ability to make observations in both real and momentum space allows complementary information to be recorded, hopefully revealing interesting physics as it did in the study of the breathing mode (see Ch. 4).

6.2. Experiments

Similar to the experiments presented in Ch. 4, the usual preparation procedures are taken for granted, and the final evaporative cooling stage is adjusted such that the resulting system lies within the qBEC regime. The modification of the interaction parameter then takes place, followed by a variable duration of evolution, before the system is imaged in either real or momentum space.

Three kinds of experiments are performed in order to tune the value of g_{1D} : modulation, abrupt changes, and ramps. Modulating g_{1D} is inspired by similar experiments performed by the team of metastable helium (He^*) in our group [85], where correlated pairs of excitations with equal but opposite momenta were observed for a nearly 1D qBEC. Changing g_{1D} abruptly falls in the category of quantum quench experiments, where the system is suddenly brought far away from its (nearly) equilibrium state and the relaxation dynamics often reveal interesting phenomena that may shed some light on our understanding of quantum ergodicity. Linear ramps in g_{1D} can be seen as a more modest version of the previous experiment, and the time scale defined by the ramp is expected to modify the final state of the system immediately after the ramp, so that one may hope to investigate the breaking down of adiabaticity during such an interaction ramp.

In the following sections, I will discuss the procedures as well as the results obtained from each experiment up to March 2014. They are by no means sufficient nor conclusive at this point, but should hopefully serve as a first demonstration that would be complemented by further experimental investigations as well as theoretical understanding.

6.2.1. Modulation

Experimental procedures

The modulation of the interaction strength g_{1D} is achieved by sinusoidally modulating the amplitude of the current in the modulated guide $I_{MG} (\propto \omega_{\perp} \propto g_{1D})$, so that the interaction strength follows the following profile during the modulation,

$$g_{1D} = g_0(1 + \alpha \sin(2\pi f_{\text{mod}}\tau)), \quad (6.1)$$

where g_0 denotes the initial interaction strength, α gives the strength of the modulation, f_{mod} is the modulation frequency. The modulation is carried out for a duration τ_{mod} , after which an image is taken with the focusing technique. Fig. 6.1 illustrates such a modulation sequence. For $hf_{\text{mod}} < \mu$, we expect the excitation of phonons, which are mainly visible in momentum space, so that the momentum distribution is recorded.

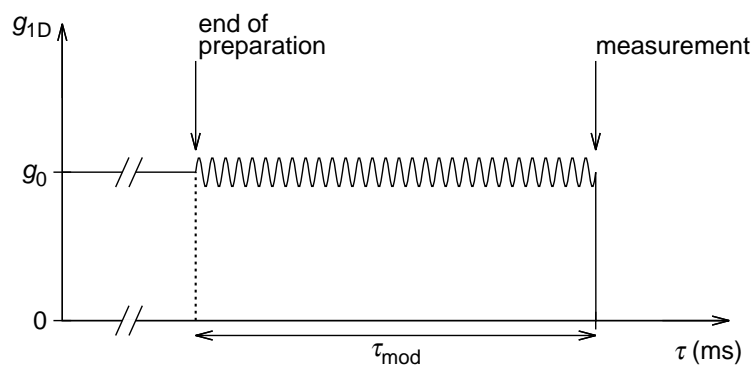


Figure 6.1.: Sequence of g_{1D} modulation.

Choice of parameters. An ideal parametric amplification calls for small amplitude and long modulation time [108]. We have implemented α values ranging from about 0.01 to 0.2, and up to 100 excitation periods¹. We observe that too large a value of α or too long a modulation time τ_{mod} simply leads to the redistribution of the injected energy (heating), as manifested by the broadening of the entire momentum distribution. Allowing the system to evolve after the end of the modulation tends to lead to the same observation, so that the measurements below are done immediately after the modulation is complete.

The values of τ_{mod} and α are experimentally adjusted, so that there is no significant broadening of the momentum distribution, whilst the population in the phonon ‘side bands’ are visible. There is also no apparent difference between keeping either the number of excitation periods or τ_{mod} constant for the values of f_{mod} attempted.

Thus, we have the following parameters held constant for the data presented

¹1 excitation period is given by $1/f_{\text{mod}}$.

below:

$$\alpha \simeq 0.1, \text{ and} \quad (6.2)$$

$$\tau_{\text{mod}} f_{\text{mod}} = 30 \text{ cycles.} \quad (6.3)$$

Results

Here we present the observations made with a nearly 1D qBEC sample in a confinement of $(f_{\perp}, f_z) \simeq (1900, 6.2)$ Hz. The characteristics of the sample can be summarized as follows,

$$N_{\text{tot}} \simeq 9300, \quad (6.4)$$

$$T_{\text{prof}} \simeq 110 \text{ nK}, \quad (6.5)$$

corresponding to $(t, \gamma_0) = (1400, 0.0025)$. The atom-number fluctuations are not measured here.

We plot in Fig. 6.2 the measured momentum distribution before and after the g_{1D} modulation. Three values of $f_{\text{mod}} = 2.5$ kHz, 3.2 kHz, and 4.4 kHz are shown (see legend). The panel on the left shows the raw profiles measured, while the panel on the right shows the difference between the profiles before and after the modulation.

As a first study, we analyze the data in a similar manner as [85]. From the calibration scan obtained without the modulation, we have $\bar{\mu} \equiv \frac{\mu_{3D}}{\hbar\omega_{\perp}} \simeq 1.63$, from which the speed of sound c can be obtained via

$$mc^2 = (\bar{\mu} - 1/\bar{\mu})\hbar\omega_{\perp}/2, \quad (6.6)$$

shown as the dashed lines in Fig. 6.2. The energy and momentum conservation dictates that $\hbar\omega_{\text{mod}} = 2\hbar\omega_k$, where $\pm\hbar k$ is the momentum of the excited phonon modes, and $\hbar\omega_k$ is their energy. Using the Bogoliubov-de Gennes spectrum,

$$\hbar\omega_k = \sqrt{c^2(\hbar k)^2 + \left(\frac{(\hbar k)^2}{2m}\right)^2}, \quad (6.7)$$

we obtain the value of $\hbar k$ for each modulation frequency f_{mod} , shown as the solid

lines with colors corresponding to those of the data in Fig. 6.2. Note that the broadening of the central low-momenta peak is minimal here but appears enhanced in the log scale used.

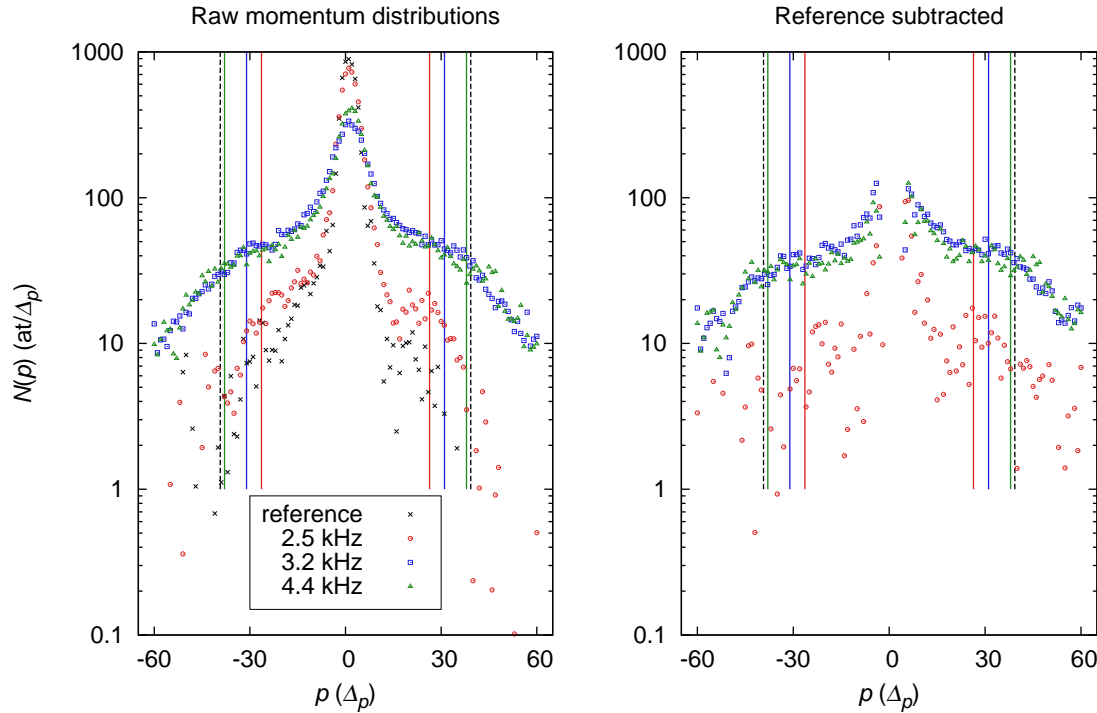


Figure 6.2.: The momentum distribution measured before (reference) and after the modulation of g_{1D} for three values of f_{mod} . Both the raw profiles (left) and the difference from the reference (right) are shown. The dashed lines mark the momenta corresponding to the speed of sound, while the solid lines mark the momenta of the excited phonon modes for each f_{mod} .

Contrary to what has been observed in [85], the data shown here do not exhibit the excitation of a well-defined phonon mode. This is not unique to the data set presented, but is true for all parameter regimes explored (t between 1000 and 1500 based on the density-profile thermometry, and $\gamma_0 \gtrsim 0.001$) on our experiment. However, there is a general trend of an enhanced population of the low momenta states up to $\pm\hbar k$, seen as the fact that the wings of the measured momentum distribution fall off approximately at the position of the expected phonon momenta. The slight quantitative disagreement can be attributed to the uncertainty of $\bar{\mu}$.

Such an enhanced population resembles the so-called ‘damping products’ in [132]. A more detailed comparison with the experiment detailed in [85] reveals

the following. While the extensive parameters such as T , N_{tot} and the (1D) interaction strength² $g_{1\text{D}}$ are comparable, the intensive parameter $\gamma_0 (\propto m)$ differs substantially due to a factor 21.75 in the atomic mass between ^4He and ^{87}Rb . As a consequence, the He^* experiment in our group is able to explore samples that are much further in the qBEC regime ($\gamma_0 \lesssim 10^{-5}$ for $t \simeq 1500$) than those accessible on our experiment ($\gamma_0 \gtrsim 10^{-3}$ for similar t values). A GPE simulation assuming qBEC behavior confirms that further into the qBEC regime, well-defined phonon modes can be more easily excited and survive sufficiently long to be observed, while the contrary is true for samples that are closer to the qBEC to IBG crossover.

Outlook

Going forward, now that we have seen the extreme cases where the observation of the parametrically amplified phonon modes is either possible or not, it would be interesting to study the intermediate behavior of both the susceptibility to such excitations and the lifetime of the excited modes. This would be within the reach of a joint effort between both the He^* experiment and ours, provided a common point of the intensive parameters in the 1D phase diagram (γ_0 in particular, since the matching of t is possible as it is) can be found. It would require some changes in the current setup, and therefore falls under the category of future developments.

6.2.2. Abrupt changes

Experimental procedures

Here, we vary the interaction parameter $g_{1\text{D}}$ in time according to the profile depicted in Fig. 6.3 at the end of the evaporation (i.e. the preparation).

Although the intention is to abruptly displace the system into a highly nonequilibrium state, care has to be taken not to send a significant population into the transverse excited states so that the (nearly) 1D nature is not broken immediately. Since $f_{\perp} \simeq 2$ kHz defines a time scale $1/f_{\perp} \simeq 0.5$ ms, the ramp is executed for

²Recall that $g_{1\text{D}} = 2\hbar\omega_{\perp}a$, and the choice of ω_{\perp} coincidentally compensates the difference in a for the experiment in [85] and ours, such that the values of $g_{1\text{D}}$ in these two cases differ by about 10% only.

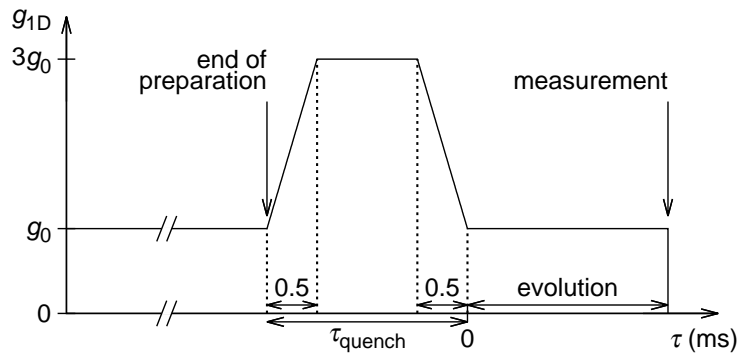


Figure 6.3.: Sequence of g_{1D} double quench.

this duration. In addition, a relatively low RF field is kept in order to allow the atoms excited into the transverse excited states to escape.

A single ramp in g_{1D} would have been conceptually simpler. However, this is expected to generate a strong breathing oscillation since the excess interaction energy would drive the density and size oscillations, which may mask other interesting features of the subsequent evolution. Therefore, a trapezium profile of g_{1D} (double quench) is used to minimize the excitation of the breathing mode.

The excitation strength $\alpha = g'_{1D}/g_{1D} \simeq 3$ is held constant here and in the next experiment. The effect of this parameter is not yet investigated.

Preliminary results

Here we present the observations made at long evolution times with a nearly 1D qBEC sample in a confinement of $(f_{\perp}, f_z) \simeq (1900, 6.2)$ Hz. The sample characteristics can be summarized as follows,

$$N_{\text{tot}} \simeq 12000, \quad (6.8)$$

$$T_{\text{prof}} \simeq 130 \text{ nK}, \quad (6.9)$$

corresponding to $(t, \gamma_0) = (1600, 0.0019)$. The atom-number fluctuation gives $T_{\text{fluct}} \simeq 100 \text{ nK}$ for $\delta_z = 3 \mu\text{m}$.

We plot the evolution of the width in real and momentum space after the double quench in Fig. 6.4. The widths are obtained and analyzed in the same way as those detailed in Ch. 4.

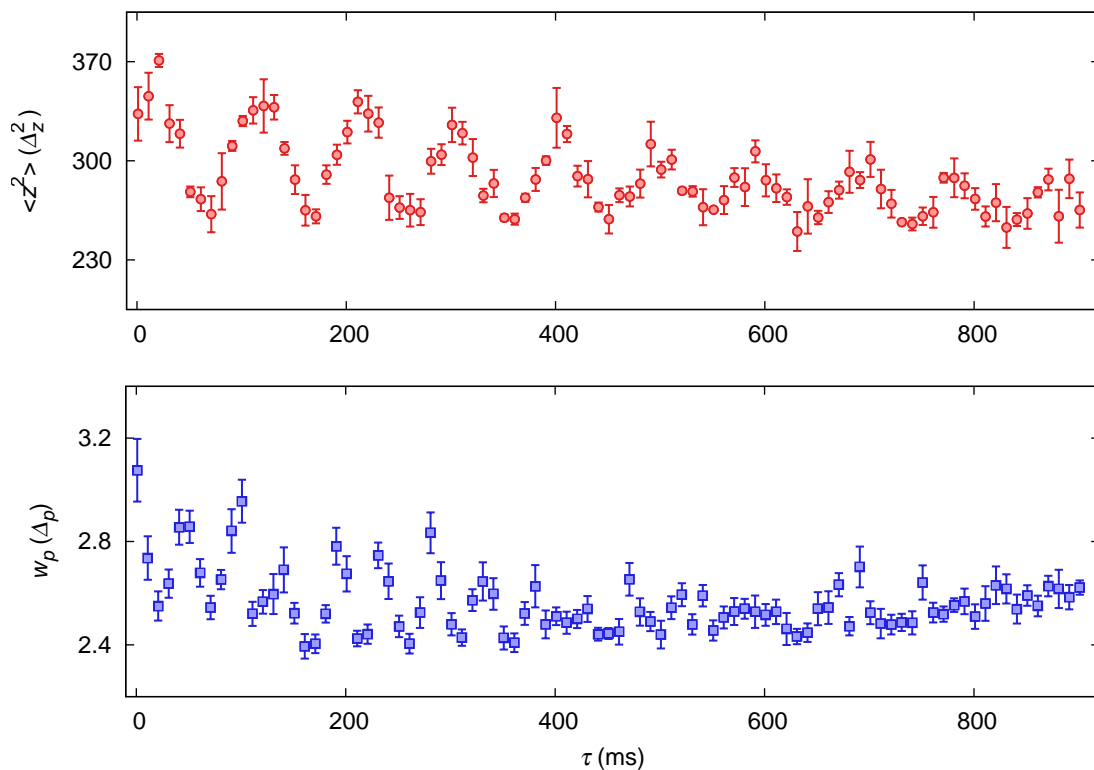


Figure 6.4.: The widths evolution in real and momentum space measured after a g_{1D} double quench. The error bars only accounts for the statistics.

In real space, a slight breathing oscillation remains. We measure

$$f_{Bz}/f_D = 1.67 \pm 0.01, \quad (6.10)$$

$$Q_{Bz} = 42 \pm 9. \quad (6.11)$$

Given that $N_{\text{tot}}/N_{\text{TE}} \simeq 28\%$ here, the breathing behavior (in terms of both the frequency and the lifetime) induced by the g_{1D} quench is similar to that induced by a quench of f_z , as recorded in Sec. 4.4.

In momentum space, the evolution in the initial 400 ms exhibits a frequency doubling with the relative power of the second harmonic $K = 0.93 \pm 0.16$. The subsequent evolution is however more complex. A quick and dirty Fourier analysis reveals more frequency components besides the fundamental and second harmonic, vaguely resembling what has been observed in [115], except that I do not find candidates among other collective modes that could immediately explain these frequencies. Given that each frame is imaged about 20 times, these

frequency signals are likely above the noise. However, further theoretical understanding is necessary before any assertion can be made.

Outlook

The short-time evolution is not yet investigated in detail. Although one would expect interesting phenomena such as the light-cone effect in the spreading of correlations [34, 100], the early attempts made in this direction at the end of 2012 were fruitless, most likely as a result of poorer loading condition at the early stage of the dispenser life cycle. More attempts will probably be made in the future.

6.2.3. Ramp

Experimental procedures

This experiment aims to investigate how the time scale defined by a linear ramp in g_{1D} modifies the subsequent behavior of the system. In this case, the value of g_{1D} follow the profile depicted in Fig. 6.5. As in the previous experiment, the excitation strength $\alpha \simeq 3$ is a controlled parameter. Different durations of the ramp τ_{ramp} between 1 ms and 20 ms are implemented. Also, the only observation made so far is in momentum space, where yet another attempt of searching for correlated excitation pairs of equal and opposite momenta is made.

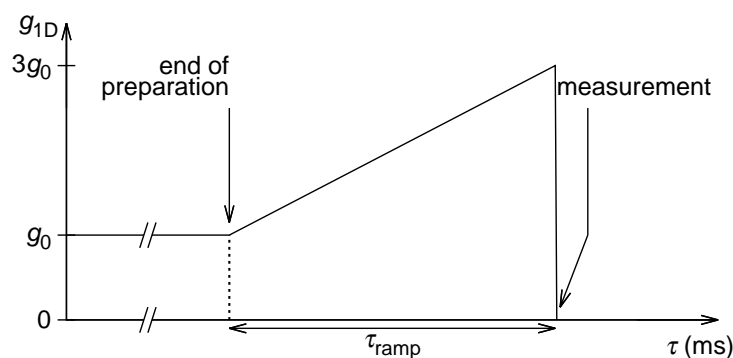


Figure 6.5.: Sequence of g_{1D} ramp.

Preliminary results

Here we present the observations made with a nearly 1D qBEC sample in a confinement of $(f_{\perp}, f_z) \simeq (1900, 6.2)$ Hz. The sample characteristics can be summa-

ized as the following,

$$N_{\text{tot}} \simeq 7600, \quad (6.12)$$

$$T_{\text{prof}} \simeq 140 \text{ nK}, \quad (6.13)$$

corresponding to $(t, \gamma_0) = (1700, 0.0032)$. The atom-number fluctuation gives $T_{\text{fluct}} \simeq 63 \text{ nK}$ for $\delta_z = 3 \mu\text{m}$.

Figure 6.6 shows the momentum correlations measured before and after the ramp with $\tau_{\text{ramp}} = 5 \text{ ms}$. Each data set is obtained with about 150 shots of images using the focusing technique, and analyzed following the procedures outlined in Sec. 3.3.2. The speed of sound according to Eq. (6.6) is at the edge³ of the plots shown.

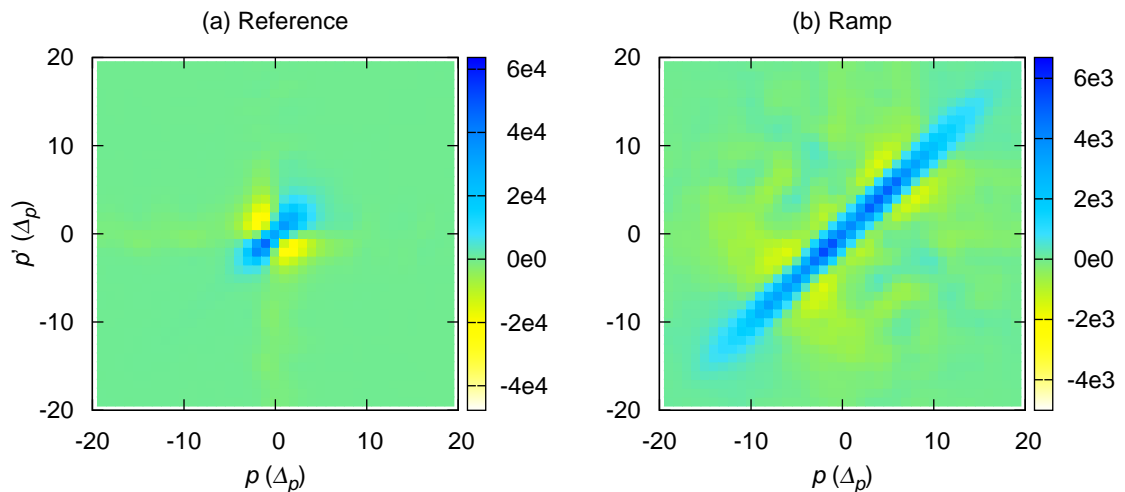


Figure 6.6.: The momentum correlations $\langle \delta N(p) \delta N(p') \rangle$ measured before (left) and after (right) a ramp in g_{1D} with $\tau_{\text{ramp}} = 5 \text{ ms}$. Note the different color scales used.

We see that without the ramp in g_{1D} , the features of the momentum correlations spreads over about 10 pixels, and strong anticorrelations (negative regions) along the $p = -p$ antidiagonal are seen, as expected of a system in the qBEC regime. After the g_{1D} ramp, the correlations along the antidiagonal become slightly positive, while the anticorrelations are displaced away from the antidiagonal.

³ $p_c = 18.2\Delta_p$ before the ramp and $19.2\Delta_p$ after the ramp.

Comparing both plots⁴, one may be tempted to conclude the creation of correlated excitation pairs from the emergence of positive correlations along the $p = -p$ antidiagonal. However, more samples are necessary for a confirmation. Also, the effect of τ_{ramp} has not been analyzed yet, pending the development of a single meaningful quantity from the momentum correlation matrix (see Sec. 3.3.2).

Outlook

The investigation thus far deals with the two-body correlations in momentum space. A recent theory paper by Bernier *et al* [14] shows that signatures of slow quench also exist in the one-body correlations, which decays in a different manner at short and long distance, and the propagation of the boundary separating these regimes resembles the Lieb Robinson dynamics of entangled quasi-particle pairs. One-body correlations can be probed by the measurement of the momentum distribution on our experiment. This will likely be investigated in the future.

Conclusions

In this chapter, we have seen a few experimental studies that aim to investigate the highly nonequilibrium behavior of (nearly) 1D Bose gases. The preliminary results indicate that:

- By modulating the interaction strength, we find that it is nearly impossible to observe well defined phonon modes for the experimental parameters (temperature and density) explored. It seems to be a consequence of a low response ('susceptibility') of the system to parametric amplification, and the short lifetime of the initial excitations possibly due to the presence of strong thermal fluctuations.
- An interaction double quench appears to reduce to a small-amplitude

⁴Owing to the difference in the absolute value of the correlations (see the color scale in Fig. 6.6), subtraction of the reference is not helpful in data visualization here.

breathing mode, for which the behavior in real space (frequency, lifetime) is governed by what we know from the study presented in Ch. 4. Interesting frequency signals appear in the long-time evolution in momentum space, in addition to the interaction induced frequency doubling expected of a qBEC. This may have some connection with nonlinear coupling between different collective modes. The short-time behavior has not been fully investigated.

- A sample data after a slow interaction ramp displays suppressed momentum anticorrelations between equal but opposite momenta ($p = -p'$), suggesting the possibility that correlated excitation pairs are generated. The dependence on the ramp rate has not been analyzed, pending the development of a single meaningful quantity from the momentum-correlation matrix.

Part III.

Beyond the Boundary

The development of experiments manipulating ultracold atomic gases have continuously benefited from technological advances. Fast electronics allow accurate experimental control, in turn improving the experimental precision. The development of semiconductor CCD chips enables the optical imaging of a wider and wider range of atomic species. Advanced laser technologies and fiber optics have tremendously improved the experimental stability and reproducibility in the past years. Technological improvements on an existing experimental setup is therefore crucial for its future capability and operability.

During my doctoral studies, I participated in the design and construction of some of the technological upgrades on our experiments. This part is devoted to the documentation of such efforts. The applied nature of the work presented here differs dramatically from the quantum schmantum recorded in the previous parts of the manuscript. The physical effects are better understood here, and it is the details of the implementation that would serve as a guide to the future users of our setup.

I organize this part as follows. Chapter 7 documents the design, assembly and preliminary tests of a new diffraction-limited imaging objective that will tremendously improve the imaging resolution. The final Ch. 8 records other technological upgrades that have taken place or will happen in the near future.

7. A New Imaging Objective

Contents

7.1. Motivation	126
7.1.1. Physics	127
7.1.2. Technology	129
7.1.3. Practical considerations	130
7.2. Problem	132
7.2.1. Optics	132
7.2.2. Mechanics	133
7.3. Solution	134
7.3.1. Design	135
7.3.2. Assembly	141
7.3.3. Testing	144

The ability of efficiently detecting phenomena of interest has always been at the heart of experimental research. Qualitative changes of detection techniques are often associated with new discoveries. Yet, quantitative improvement of existing techniques could also enable new methods of detection and analysis. Within the field of ultracold atomic gases, for instance, the ability to resolve single atoms in a Mott insulator [138] directly enabled the experimental simulation of the correlation propagation dynamics in a solid-state like system and the measurement of Lieb-Robinson bound [34]. In this chapter, I document my efforts to improve the imaging resolution of our current experimental setup through the design and construction of a diffraction limited objective with a medium-high numerical aperture (NA). Theory of optics and optical components are well established and therefore will not be the focus of this chapter. Rather, it is intended to be a

text documenting the thoughts and process that took place in completing such a task, so that future users of the experiment may understand the rationale behind various decisions.

I organize this chapter as follows. I discuss the physical, technological as well as practical consideration that motivated the project in Sec. 7.1. The problem is then formulated in Sec. 7.2, dictating the requirements in both optical performance and mechanical constraints. Sec. 7.3 then presents the solution in terms of its design, construction, as well as results of the performance tests. Concluding remarks are included at the end of the chapter.

7.1. Motivation

As mentioned in Ch. 1, our current imaging system (see Fig. 7.1) consists of a pair of off-the-counter optics that image the atoms on a CCD camera. I recall the imaging characteristics below:

$$\text{pixel size (linear dimension)} \Delta_z = 2.7 \mu\text{m}, \quad (7.1)$$

$$\text{PSF radius } r_{\text{PSF}} = 2.4 \mu\text{m}, \quad (7.2)$$

$$\text{RMS width of atomic diffusion spot } \delta_z \simeq 3 \mu\text{m}. \quad (7.3)$$

The pixel size in the object plane is obtained by measuring on the camera the size of a known structure. For instance, the three parallel wires that produce the modulated guide are about $1411 \mu\text{m}$ long.

The PSF radius refers to the radius of the first dark ring of the Airy pattern, knowing the object NA ($= 0.2$) of the objective, and is given by $r_{\text{PSF}} = \frac{0.61\lambda}{\text{NA}}$ evaluated at the imaging wavelength $\lambda = 780 \text{ nm}$.

Finally, the RMS width of the atomic diffusion spot during the imaging pulse is measured experimentally for typical *in situ* imaging parameters (pulse duration, saturation, and detuning). Details can be found in [82].

Besides the ever thrilling satisfaction of building better optics, motivations in

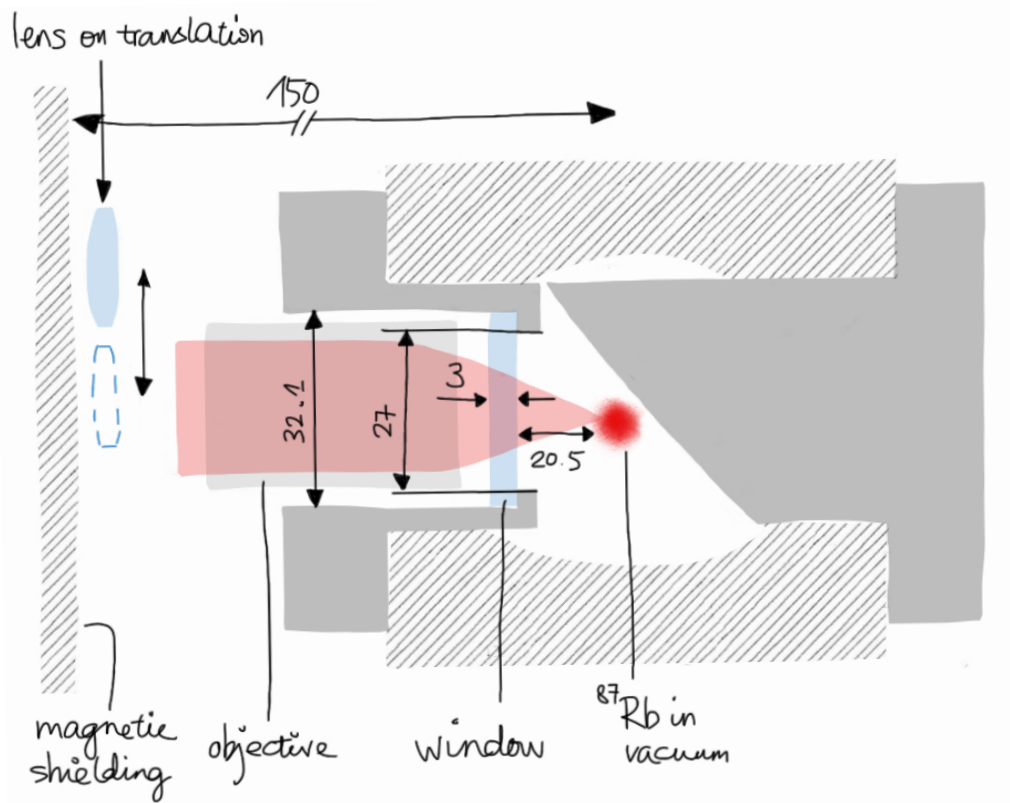


Figure 7.1.: An illustration of the spatial constraints of the new imaging objective. All dimensions are given in mm. The longitudinal axis of the atomic cloud is perpendicular to the plane of the paper. For clarity, the projecting doublet and the camera are not included here (see Fig. 1.6 for the entire imaging system). Instead, the spatial constraints for the new imaging objective is shown. An additional lens (to be mounted on a motorized translation stage) is needed during the MOT loading, and retracts away from the imaging path afterwards.

both physics and technology exist. I briefly outline both below, followed by a discussion of practical considerations.

7.1.1. Physics

The physical motivation to improve the spatial resolution lies in the consideration of signal to noise ratio (SNR) in the presence of atomic diffusion. Here, we assume the objective is diffraction limited, and there is a fixed relation between Δ_z and r_{PSF} as both are determined by the imaging optics and the resolution is always limited by the worse factor between the two. Hence, the dependence on NA of

r_{PSF} is carried over to Δ_z , up to a numerical factor that depends on the choice of the magnification.

We now consider the signal of a single atom registered in a single pixel on the CCD camera via absorption imaging. The photon count for a probe beam of intensity¹ I_{pr} for a duration τ_{pr} is given by $N_{\text{ph}} = I_{\text{pr}}\tau_{\text{pr}}\Delta_z^2\lambda/(hc)$. The absorption signal (in units of photon number) is then $\frac{\sigma}{\Delta_z}N_{\text{ph}}$ if all is collected within the same pixel, where $\sigma = \frac{\sigma_0}{1+s}$ is the scattering cross section, and $s \equiv I_{\text{pr}}/I_{\text{sat}}$ is the saturation parameter of the probe beam. Since the technical noise of the camera is negligible in our case, the main source of noise is the photon shot noise (PSN) given by $\sqrt{N_{\text{ph}}}$. Thus, we have an expression of SNR given by

$$\text{SNR} = \sqrt{\frac{3\lambda^2\Gamma}{4\pi}} \frac{1}{\Delta_z} \frac{\sqrt{s}}{1+s} \sqrt{\tau_{\text{pr}}}, \quad (7.4)$$

where the saturation intensity I_{sat} for the σ^+ transition on resonance is expanded in terms of the natural line width Γ and the transition wavelength λ . Therefore, a better SNR is obtained at small Δ_z or long probe pulse τ_{pr} .

However, the statement above is no longer true in the presence of atomic diffusion. During the probe pulse, the diffusion of the atoms can be modelled by a random walk in momentum space [82]. The resultant mean-square displacement is given by

$$\langle \delta z^2 \rangle = \frac{N_{\text{ph}}}{3} \left(\frac{h\tau_{\text{pr}}}{m\lambda} \right)^2 \quad (7.5)$$

$$= \frac{h^2\Gamma}{6m^2\lambda^2} \frac{s}{1+s} \tau_{\text{pr}}^3 \quad (7.6)$$

so that the condition of keeping the atom in question within the pixel, i.e. $\sqrt{\langle \delta z^2 \rangle} < \Delta_z$ gives a lower bound of the pixel size for a given τ_{pr} .

For experimental values of s ranging from a few per cent to on the order of unity², there is little qualitative change in the behavior of the conditions above. We thus plot in Fig. 7.2, for $s = 0.15$, the SNR as a function of τ_{pr} and Δ_z in a color map, and shade the inaccessible region due to atomic diffusion. We see that within the limit of resolution, a smaller pixel size and a shorter probe pulse are favorable

¹also known as irradiance in optics.

²which is relevant for experimental realizations.

to achieve a larger SNR. The need for smaller (and resolved) pixel size translates into the requirement of a larger object NA.

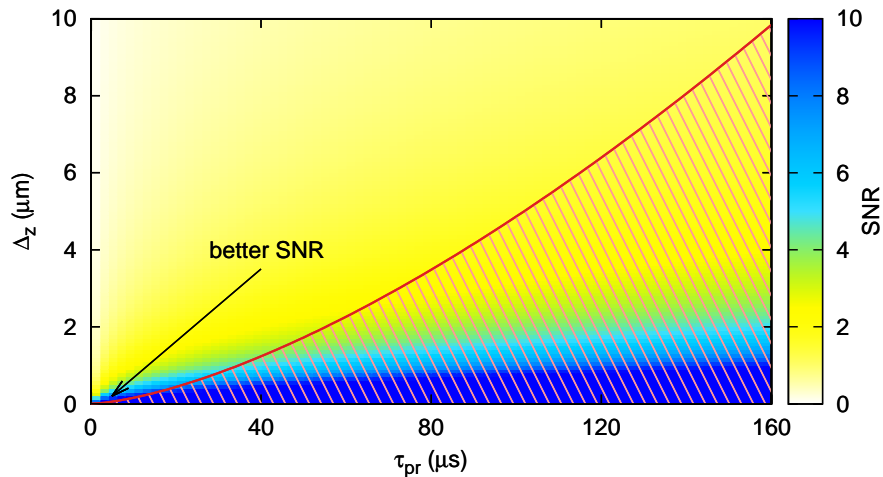


Figure 7.2.: SNR as a function of probe duration τ_{pr} and pixel size Δ_z at constant saturation parameter $s = 0.15$. The color scale of the SNR is clipped at 10 in order to demonstrate the variation at small SNR.

A side remark. The above analysis also provides evidence that it would be disadvantageous to image using the $^5S \rightarrow ^6P$ transition despite the apparent gain in the diffraction limit. Indeed, this transition has a wavelength $\lambda = 420$ nm and a natural line width $\Gamma = 2\pi \times 1.3$ MHz for ^{87}Rb , so that for the same s and τ_{pr} , the SNR degrades by about a factor 4 according to Eq. (7.4) whereas the diffusion remains approximately the same according to Eq. (7.6), rendering it more difficult to achieve a high SNR.

7.1.2. Technology

Science and technology have always been entangled in their development. Despite the fact that experiments of ultracold atomic gases have been used predominantly for fundamental research thus far, the sheer complexity of such experiments calls for exceptional technological expertise in order to achieve acceptable precision in control, manipulation, and detection of such systems.

Among various detection schemes, imaging using a camera has been proven robust and is widely used. The improvement of the spatial resolution received ded-

icated attention on various occasions [4, 13, 117]. A quick survey of a few recent experimental works [138, 156] enabled by improved imaging resolution demonstrates precisely the importance of such technological developments. Figure 7.3 places a few notable examples in this spirit on a time line. They are categorized according to if the imaging objective is commissioned from an external company, home-made, or bought off-the-counter. The information is obtained mainly from [13] and the references therein, so that it is by no means exhaustive. However, the general tendency in the technological development is indisputable. In particular, the group of experiments with home-made objective exhibits a clear trend of improving the resolution (as a result of increasing the NA), shown as the shaded band in Fig. 7.3.

On our experiment, the last upgrade of the imaging setup took place around year 2012 (square labelled 'PUCEex' in Fig. 7.3), achieving a NA of 0.2 and a pixel size $2.7 \mu\text{m}$. In order to improve the resolution, an objective with NA comparable to the above mentioned experiments is needed.

7.1.3. Practical considerations

A test quotation from J. Fichou³ estimates the cost of a single piece of customized objective (design and production) to be around €8000, which is a costly investment on an ultracold atom experiment. A search through the catalogues (see table) of renown microscope objective manufacturers indicates that it is unlikely to find mass-produced objectives⁴ that fulfill all performance requirements (see next section).

On the other hand, the various technical expertise available at Institut d'Optique are not to be underestimated. Optical design is a course taught to the second-year students in optical engineering on a regular basis, so that both experienced staff and dedicated softwares are readily available. The optical workshop has been polishing optics that would produce wavefront distortions of " λ over what you want"⁵, while the mechanical workshop can easily produce pieces of lin-

³URL: <http://www.optique-fichou.com/en/>.

⁴which tend to cost about €3000 per piece on average.

⁵Direct translation from a verbatim quote by Gilles Cola, former optician at the institute, now retired.

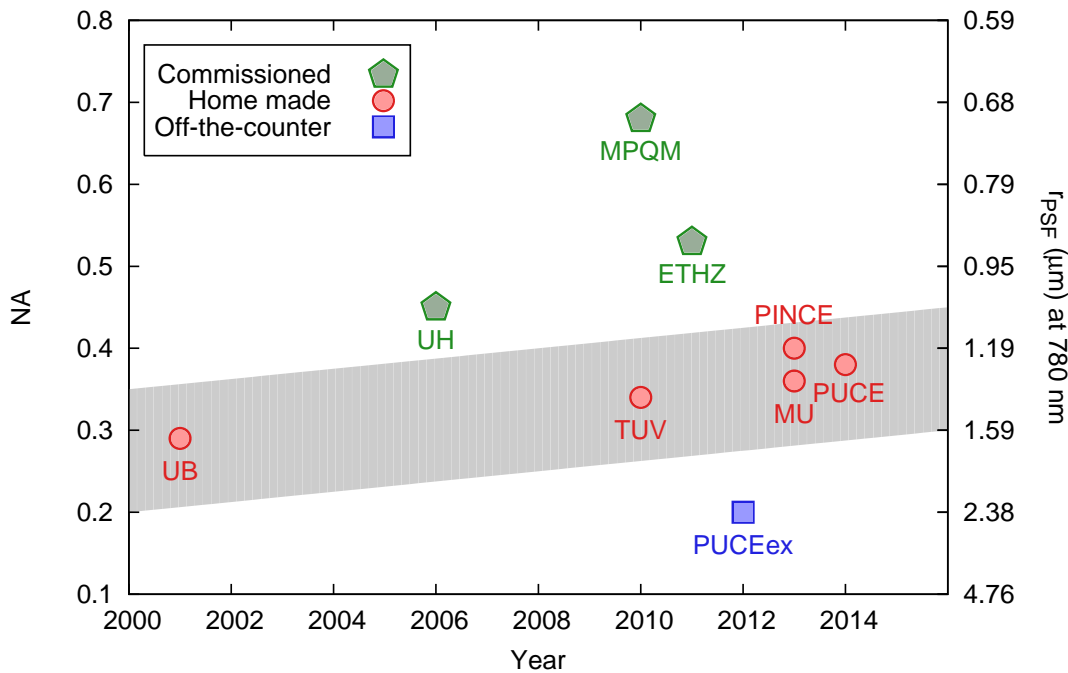


Figure 7.3.: Imaging NA of a few recent experiments with *ex vacuo* optics. The information is obtained mainly from [13] and the references therein, and is therefore by no means exhaustive. The corresponding radius of the central Airy disc evaluated at 780 nm is shown on the right as a reference^a. The data labels are given here^b.

^aOnly two experiments operate at different wavelengths: ETHZ at 671 nm and UB at 852 nm. The resulting difference in r_{PSF} is about 10% and does not introduce qualitative change in the graph above.

^bUB: University of Bonn [4], UH: University of Heidelberg [117], MPQM: Max-Planck Institute München [138], TUV: Technical University of Vienna [22], ETHZ: Swiss Federal Institute of Technology in Zurich [156], PUCE and PUCEex: atom-chip experiment at Institut d’Optique Palaiseau (‘ex’ for the existing set up [82, 84]), PINCE: optical-tweezer experiment at Institut d’Optique Palaiseau [111], MU: Monash University [13].

ear dimensions up to $\pm 10 \mu\text{m}$ within the specification. The synergy between the workshops has already lead to the successful construction of another imaging objective currently used on the ‘PINCE’⁶ experiment [111]. Equipments measuring the performance of optical elements are available from the teaching department⁷, where practical tasks are taught via lab courses.

Hence, the production of the current microscope imaging objective presents the perfect opportunity for me to collaborate with various experts in their respective

⁶French for tweezer. The namesake is an optical tweezer that transports an ultracold cloud of atoms over about 30 cm.

⁷known as Laboratoire d’Enseignement Expérimental (LEnsE).

Model	Working distance	Glass thickness	Numerical aperture	Outer diameter	IR transmission
Mitutoyo G Plan Apo	29.42 mm	3.5 mm	0.28	34 mm	unknown
Zeiss EC Plan Neofluar	18.5 mm	0.17 mm	0.16	30 mm	~ 88%
Olympus EO M Plan Apo	20 mm	unknown	0.42	34 mm	unknown
Leica Pl Fluotar	6.7 mm	≤ 2 mm	variable	31.5 mm	~ 80%
Nikon CFI S Pl Fluo	≤ 8.2 mm	≤ 2 mm	0.45	unknown	unknown

Table 7.1.: List of available commercial microscope objectives and their key characteristics. Information are obtained from the online sales catalogue. The best option (Mitutoyo) suffers from too large an outer diameter and less-than-ideal NA. Other options are generally incompatible with the desired long working distance and insufficient correction power, as a 2 mm window thickness may be detrimental to the UHV desired.

fields and have a first-hand experience in simple instrumentation.

7.2. Problem

The requirement of the final objective covers two areas: the optical performance and the mechanical constraints. Both aspects are crucial in order for the objective to be integrated onto the existing experiments. I describe them below.

7.2.1. Optics

Using the design principles outlined in [4], the desired optical performance can be summarized as follows. The objective should

1. conjugate focus to infinity, thus collimating the light that is emitted and/or scattered by the atoms;
2. have an NA of at least 0.3, and the larger the merrier;
3. have a working distance > 23.5 mm, due to a 20.5 mm atom-window separation and a 3 mm window thickness;
4. be nearly diffraction limited at 780 nm, correcting the aberration introduced by the window, which is made of standard BK7 glass;
5. have a diffraction limited field of view of at least ± 100 μm , which is the typical longitudinal size of the atomic cloud.

7.2.2. Mechanics

Given that the objective is to be integrated onto a working experiment, mechanical constraints due to the existing setup need to be carefully accounted for.

The current setup has a limited optical access due to the size of the vacuum chamber, which is a cube of 7 cm on each side. The atoms are situated nearly at the center of the cube, whereas the objective is mounted outside a standard CF40 window. The required long working distance (> 35 mm) usually implies a larger focal length and therefore a smaller NA.

One way to improve the NA of the system would be to mount the objective in vacuum. This strategy completely avoids the task of aberration correction, since the light would only encounter the window after being collimated, so that ideally no aberration would be introduced. However, the simplicity of optics⁸ has to be traded off by the complexity of the mounting mechanics in order to retain certain degrees of freedom in positioning the lens(es) with respect to the atoms. A notable example in this spirit is the HALO lenses developed for ion trapping [126, 129]. The accompanying piezo translation system is however too bulky for our setup. Also, given the combination of NA and long working distance, monolithic

⁸provided the NA remains medium-high. A high-NA *in vacuo* objective would still require a complex optical design [151].

mounting mechanics such as those used in [139] are impractical. The prospective of breaking the vacuum in order to access the objective⁹ is also unattractive.

Since customization appears inevitable, a reentrant flange has been designed in order to reduce the working distance. The resultant spatial dimensions are illustrated in Fig. 7.1. Correspondingly, the following spatial constraints apply:

1. The reentrant tube limits the aperture at a diameter of 27 mm at the position of the window.
2. Since the (assembled) objective will be mounted inside the reentrant tube, its outer diameter is limited by a few factors. The inner diameter of the reentrant tube is 32.1 mm. The position of the atoms have $\pm 500 \mu\text{m}$ uncertainty due to the mechanical uncertainty in mounting the atom chip. A certain space should be left for the wall of the lens tube that contains the objective. The minimal wall thickness depends on the material.
3. The overall length of the objective assembly is limited by the magnetic shielding, which has an inner diameter of 300 mm. Mounting mechanics should also be accounted for. This essentially means a small overall length is favored.
4. The construction should be tolerant to potential imperfections during the assembly, given that the mechanical parts can be accurate up to $\pm 10 \mu\text{m}$ within specification.

7.3. Solution

This section is intended to be the documentation of the objective. It records the optical design, assembly, as well as the tests I carried out. For each section, I will discuss about the considerations, followed by the procedures for the actual task, and then show the results obtained.

Note that the design principles and optimization methods mentioned here are

⁹e.g. in the event of unintended Rb deposition on the lens surface.

also applicable to more general tasks of optical design.

7.3.1. Design

Considerations

Designing a medium-high-NA microscope objective from scratch seems to be a formidable task. Although the final goal is clearly spelt out, namely to correct the aberration introduced by a specific window while achieving a specific NA at a specific wavelength, a myriad of strategies exist [67], and one with little experience such as myself could easily lose the way.

Fortunately, similar tasks have been pursued before, notably in [4, 117]. Both could be used as a starting test design, so that the task simplifies slightly into a multivariable optimization in order to adapt the lens parameters (number of surfaces, glass material, radii of curvature, lens thickness and air spaces) to suit the new performance objective. For practical purposes, the work of [13] presents a step further in reducing the production complexity and the construction cost of the objective by adapting the design to catalogue lenses.

Commercial softwares performing classical ray tracing can be used for such an optimization. Among the three options available at Institut d'Optique, namely, OSLO, Zemax, and Code 5, the choice of using OSLO is arbitrary and out of convenience, since a free educational version is available for preliminary studies. It is also known that the performance of the optimization algorithms embedded in these softwares are comparable barring exceptional cases.

Procedures

The procedure used to carry out the optimization is listed below. Note that this is not intended to be a manual of OSLO, so that details such which function is used are omitted unless it is particularly relevant. Interested readers should refer to the official manual (available online) in order to familiarize themselves with the usage of the software.

Initialization. I start by adapting the design in [117] (the pentagon labelled 'UH'

in Fig. 7.3) to meet some of the desired specification¹⁰. Namely,

1. the entire system is scaled up so that the working distance is about 20.5 mm as needed, while the NA is preserved (at 0.45);
2. the entrance beam diameter is then reduced to 27 mm so that sufficient space is left for the lens tube and spacers. This reduces the NA to about 0.38;
3. the field is set to $\pm 250 \mu\text{m}$ so that a typical size of the atomic cloud of $200 \mu\text{m}$ can be easily accommodated.

Note that all lenses are set to the same diameter of 29.7 mm in order to simplify the design of the mechanical mount. The glass for the lenses are set to SF11 in order to take advantage of the high refractive index and thus stronger bending power per surface. The associated strong dispersion is irrelevant for a monochromatic system.

The scaling gives a resulting window thickness ~ 4.5 mm, too large compared to the desired 3 mm. This is left as a controlled parameter during the optimization.

Variables and error function. As with any optimization task, one needs to set the variables and the error function. The variables, to begin with, include all radii of curvature, the thickness of the three lenses, as well as all air spaces. Only the distance from the window (final flat surface in vacuum) to the atoms (focal point) is fixed to 20.5 mm as required.

The construction of the error function is a more complicated task. It is generally a weighted sum of all aberration coefficients at various position of the field, and the Euclidean distance from the desired NA. The careful choice of such weights determines the efficiency of convergence of the algorithm as well as the ability to find a global minimum of the error function. It takes rigorous studies (see e.g. [67] as a comprehensive textbook) and decades of experience to be able to choose them at will. This is also partly why commercial softwares are valuable,

¹⁰Note that the same procedure has been used starting from the Alt design [4]. However, the end product is ruled out due to poorer tolerance towards uncertainty in assembly. This will be explained later.

as they often come with ready-to-use routines that can construct error functions for various purposes. For OSLO, two of such routines exist for free, the OPIC and the GENII routines. Details of the algorithm behind is again beyond the scope of this manuscript. Documentation can be found online easily. For the construction of this objective, the GENII routine is used¹¹ and has demonstrated excellent convergence properties.

Optimization. Since the optimization boils down to a multivariable minimization problem, one needs to be aware of the pitfall of being trapped in a local minimum. This can be circumvented by carrying out the optimization incrementally, i.e., instead of immediately reducing the window thickness to the desired value of 3 mm, it is decreased in steps of 0.1 mm while the minimization routine is called multiple times until a convergence is reached for each reduction step. Also, the weight associated to the enforcement of NA is deliberately reduced by a factor 10 at this stage in order to allow for a more liberal combination of the radii.

The procedure up to this stage in fact depends on the choice of the software. Once a convergence is found for the final value of window thickness (3 mm), however, it is important to make fine adjustments manually in order to improve the practicality of the design. This calls for an ambiguity avoidance check, a radii matching exercise as carried out in [13], and a precision restriction of the lens thickness and air spaces. The weight to enforce the NA is returned to the initial values at this stage in order to strictly maintain the desired NA.

Usually, it is crucial to carry out an ambiguity avoidance check in order to reduce the possibility of human error at the assembly phase¹². This means that without any significant compromise on the performance, lenses of similar shape should be made either identical or visibly different (in physical size or radius of curvature), and biconcave (or biconvex) lenses should be made either symmetric or visibly asymmetric. This is automatically fulfilled in our case due to our starting design as the two meniscus lenses are indeed dramatically different in their radii of curvature, so that no further adjustment is necessary for this purpose.

¹¹Minor changes to the weights were made to remove chromatic aberration coefficients since they are irrelevant.

¹²It would be an extremely unpleasant surprise if one finds out during performance test that one (or possibly more) of the lenses is flipped and is responsible for a poor optical performance.

Since Lens-Optics¹³ has satisfactorily provided custom and catalogue lenses to our group on several occasions, we decided to work with them again in the hope to foster synergy. A published list of radii of curvature is available on their website¹⁴. As the production process has been optimized at these values of radii, matching the required radii to the published values minimizes production uncertainty¹⁵ and reduces the cost. This is achieved iteratively. For each step, one of the remaining radii is selected based on the minimal relative difference from a published value. This radius is then taken off the list of variables and set by hand to the closest published value, while all remaining variables participate in the reoptimization until a convergence is found. In the event that it is difficult to match the final radius, one could in principle request for a single custom radius of curvature. Alternatively, tracing a few steps back and changing the order of radii matching may lead to a fully matched solution. Trial and error is needed. Fortunately enough, the current design could be matched without much difficulties.

Now, the thickness of the lenses and air spaces remain as variables. Since air spaces are known to have a stronger effect on the aberrations, we will first restrict the lens thickness. The preference of a short objective calls for the use of thin lenses. This is already the case with the outcome of optimization, although the thickness is specified up to machine precision. Starting from the lens that is the closest to the window, each thickness (at the center of the lens) is iteratively rounded to the nearest 0.05 mm and reduced to (4 ± 0.5) mm, while all remaining variables participate in reoptimization until a convergence is found.

Finally, the two air spaces within the lens triplet are rounded to the nearest 0.1 mm to allow ample room for the uncertainty of air spaces (up to the spacer construction).

Tolerancing. Testing the tolerance of the system is necessary in order to ensure a reasonable success rate in the construction. Indeed, linear dimensions of the mechanical parts are accurate up to $\pm 10 \mu\text{m}$. This would result in displacement of the lenses on axis and/or in the transverse plane, and possibly tilting the lenses

¹³URL: <http://www.lens-optics.de/>.

¹⁴URL: <http://www.lens-optics.de/radien-tabelle.html>

¹⁵We measured the radii of curvature of lenses delivered and found agreement with specification within $\sim 0.1\%$.

so that their optical axes are no longer collinear. All effects may have a dramatic impact on the optical performance given the large NA.

To carry out the tolerance test, we assume that the uncertainty of each dimension can be modelled by a Gaussian random variable with zero mean (no systematic error) and a standard deviation of $10\ \mu\text{m}$. With some algebra, these uncertainties also translate into possible tilts of the elements. A Monte Carlo sampling of the uncertainties can then be carried out using the built-in function of OSLO (premium version). I show the result of 1000 run of samples in Fig. 7.4. This suggests that the planned in-house assembly would in principle not impact the optical performance of the design.

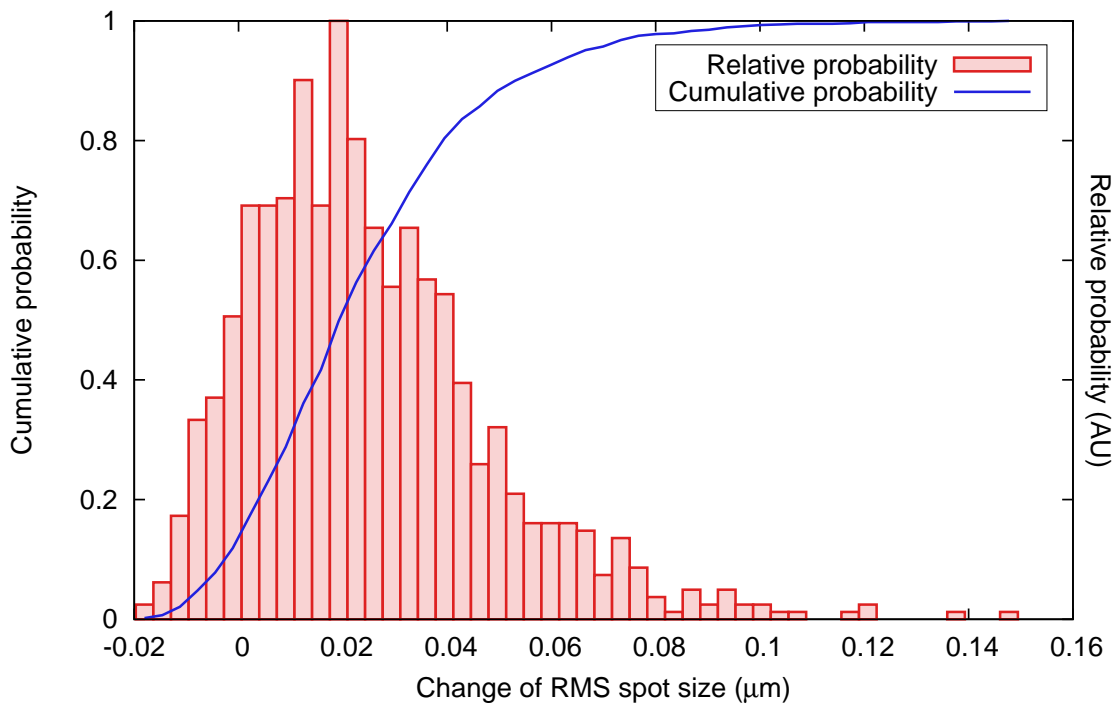


Figure 7.4.: Result of the tolerance tests using Monte Carlo simulation of mechanical uncertainties. Such a function is only available in the full version of OSLO. Note that the initial RMS spot size is $\sim 1.2\ \mu\text{m}$, so that we may safely conclude from the above result that the construction is tolerant to potential mechanical uncertainties.

Note that it is through such tolerance test that we discarded the alternative design starting from the one by Alt [4], as the simulated success rate is much lower. A closer look at the aberration coefficients associated with each surface reveals the crux of the problem. For our three-element design, the aberrations are evenly distributed over several surfaces, so that a local perturbation of the alignment has

a small effect on the overall optical performance. On the contrary, the adapted four-element design has strong aberrations associated to the final lens, so that a small misalignment of this element introduces an appreciable aberration to the entire system.

Outcome

I show the final design in Tab. 7.2 and Fig. 7.5, and its simulated performance in Fig. 7.6.

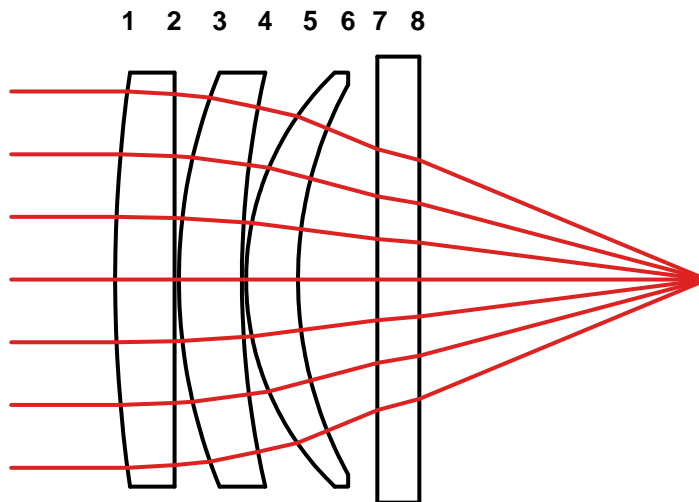


Figure 7.5.: Layout of the objective-window system. Surfaces 1 to 6 represent the objective triplet, and surfaces 7 to 8 represent the vacuum window. The atoms to be imaged will be located at the focal point of the system on the right.

The performance can be summarized in terms of the PSF, the encircled energy and the Modulation Transfer Function (MTF). The PSF is a measure of the resolving power of the system. The encircled energy is the radial integral of the PSF, and its comparison with the pixel size in the object plane also yields information about the resolution. The MTF gives the contrast in the incoherent imaging of a sinusoidal intensity modulation. The report graphics (generated directly by OSLO) are included in Fig. 7.6.

Finally, the simulated RMS optical path difference (OPD) over the entire wavefront is 0.013λ . At the best focus on axis, the Strehl ratio is $R_S = 0.993$ on axis and $R_S = 0.8$ at $\pm 245 \mu\text{m}$ off axis (in the object plane)¹⁶.

¹⁶For an optical system to be considered 'diffraction limited', we may apply the Maréchal cri-

Surface No.	Radius of curvature (mm)	Distance to next surface (mm)	Material
1	104.47	4.25	SF11
2	∞	0.3	air
3	39.446	4.5	SF11
4	66.98	0.3	air
5	20.61	3.7	SF11
6	29.161	5.66	air
7	∞	3.0	BK7
8	∞	20.5	vacuum

Table 7.2.: Surface data of the lens system.

Three sets of the lens triplets and two custom windows are ordered from Lens-Optics. Each surface will be antireflection coated with reflectance $R < 0.2\%$ at 780 nm and $R < 5\%$ at 1530 nm¹⁷.

7.3.2. Assembly

The assembly is carried out in-house with the assistance of both the mechanical workshop and optics workshops. The mount was designed in collaboration with the chief machinist Mr. André Guilbaud, while the chief optician Mr. Christian Beurthe provided means for the measurements of the dimensions.

I briefly record below the considerations that led to the design of the final mount, the procedures for mounting, as well as the outcome.

Considerations

The custom lenses were to have an diameter of $(29.7+0.5/-0.2)$ mm. A measurement of the diameters of the *actual* lenses helps to fine tune the inner diameter of the mount.

terion, which sets a (somewhat arbitrary) limit on the RMS OPD ($\leq \lambda/14$), or equivalently $R_S \geq 0.8$.

¹⁷Light at this wavelength is available and may be used for optical potential engineering. See Ch. 8 for a brief discussion.

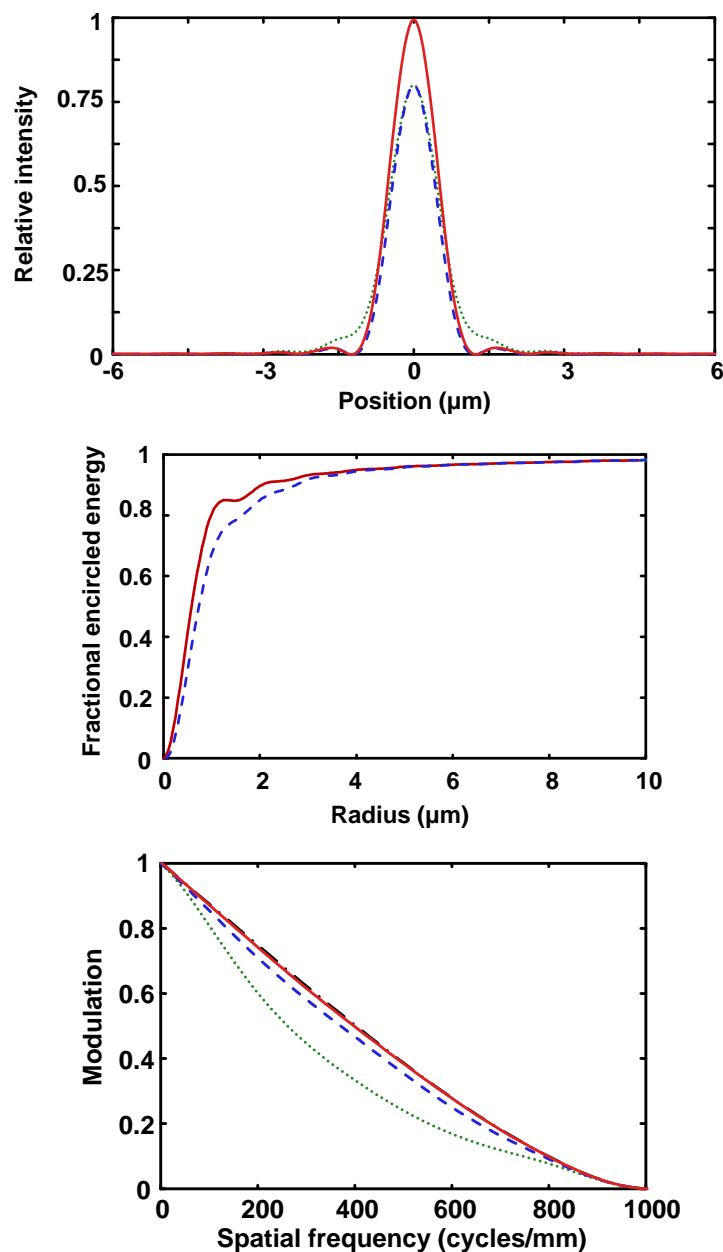


Figure 7.6.: Simulated optical performance of the objective-window system. The PSF (top), fractional encircled energy (middle), and MTF (bottom) are shown both on axis (solid lines) and at $\pm 245 \mu\text{m}$ off axis (dotted and dashed lines, corresponding to in and perpendicular to the plane containing the optical axis and field ray). The ideal performance (dash-dotted lines) is included as a reference, but it mostly overlaps with the on axis performance and is only visible in the MTF plot.

Given the restricted mechanical access in the reentrant tube and the uncertainty in chip mounting specified in Sec. 7.2.2, the outer diameter of the lens tube is made at 31.5 mm, so that the wall thickness is 0.9 mm. Mechanical stability re-

quires a choice of material that is sufficiently hard. Based on the experience of the mechanical workshop, we chose to use brass for this purpose. In addition, the possibility of carrying out anodization¹⁸ in house is an added advantage.

The position of the lenses in the triplet will be eventually secured by spacers and retaining rings, whose dimensions should well match those of the lens tube. Repetitions of mounting and dismantling are to be expected¹⁹. As a result, great care should be taken to avoid galling, which is a form of wear caused by the adhesion between sliding surfaces. This can be achieved by lubrication or appropriate choice of materials. Lubrication comes with the risk of staining the lenses and efficient means of cleaning without further damage is lacking. Instead, the spacers and retaining rings are also made of anodized brass so that no galling is expected.

As on the current setup, the new objective will be permanently fixed on the experiment. It would give a dramatic boost to the imaging resolution, but requires pairing optics during the MOT loading phase in order to retain a large loading volume. Since aberration is less crucial during the MOT loading, one simply needs a lens²⁰ to form an afocal telescope with the objective, and then adapt the beam waist with optics outside the magnetic shielding. The lens will be mounted on a mechanical translation stage which inserts the lens only during the MOT loading (see Fig. 7.1). Therefore, I need to ensure sufficient clearance at the expected position of the lens.

Procedures and outcome

The design and construction of the mounting mechanics were carried out at the mechanical workshop. The technical drawings are included in App. ?? as a record.

¹⁸so as to blacken the surface and avoid stray reflection.

¹⁹It is better to start pessimistic than to end unlucky.

²⁰E.g. Thorlabs C240TME-B with NA 0.5 and focal length 8 mm at 780 nm would suffice. The clear aperture is 8 mm, sufficiently larger than the beam size 6.6 mm at about ~ 26 mm in front of surface 1 (see Fig. 7.5 for the surface labels).

7.3.3. Testing

The ultimate performance test would of course be to image the Rb atoms on the actual experiment. However, as a control measure, it is also important to perform external tests for verification. Here I document the consideration, procedure, and the outcome of the tests performed on this objective before it is integrated onto the main experiment.

7.3.3.1. Test 1: measuring the wavefront deformation

Considerations

The performance of such a microscope objective can be characterized by measuring the optical path difference between the real and ideal wave front. This can be achieved using commercialized instruments such as a laser interferometer. We use ZYGO²¹ for this purpose, as it is readily available at LENS E.

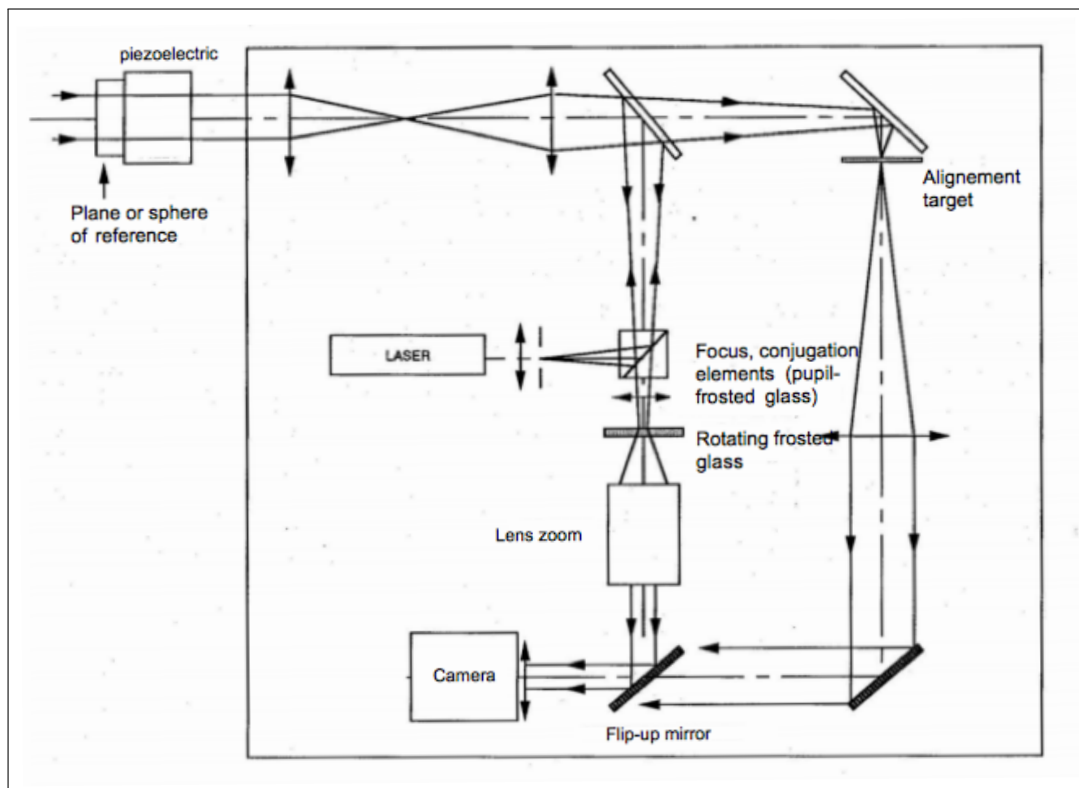


Figure 7.7.: Schematics of ZYGO. Courtesy of LENS E.

²¹Model: GPI ST; URL: <http://www.zygo.com/?/met/interferometers/gpi/>.

A schematic of the interferometer is shown in Fig. 7.7. The ZYGO interferometer is a Fizeau type interferometer with a phase-shifting piezo actuator. The reference flat wave front is a well collimated beam reflected by the almost perfect plane diopter (RMS OPD of a few percent λ) of a reference plane mirror. The measured wave front is sent through the objective-window system under test to a concave mirror, for which the center of curvature is adjusted exactly on the focus of the system on test. The interference pattern between the reference wave front and the measured wave front allows the measurement of the OPD introduced by the optical system. The OPD is very accurately measured with such a phase shift method (RMS OPD around $\lambda/20$).

The interferometer has a built-in laser system at 633 nm (He-Ne laser). The objective optimized for 780 nm is expected to exhibit a chromatic focal shift as well as spherical aberrations. We also take into account that the window delivered is slightly thicker than expected²². This can be easily simulated with OSLO, which gives the RMS OPD as 0.13λ and the Strehl ratio $R_S = 0.50$ on axis at 633 nm. We keep these values in mind throughout the measurement.

Procedures

We align in successive order the window, the objective, and the concave mirror at the output of the interferometer. Using the accompanying processing system, we measure the phase shift and obtain the OPD over the entire wave front. PSF, RMS OPD and Strehl ratio can then be computed.

Outcome

I present the test results here: the PSF in Fig. 7.8, the encircled energy in Fig. 7.9, and the MTF in Fig. 7.10. The 3.15 mm thick window is used here, giving the worse-case scenario.

The measured RMS OPD = 0.14λ and Strehl ratio $S = 0.49$ at $\lambda = 633$ nm. The residual aberration is mainly spherical (see Fig. 7.8), coming from the slightly thicker window as mentioned earlier. This is sufficient to explain the difference between the measurements and the expected performance at 780 nm (see Fig. 7.6).

²²The window thickness is 3 mm in design, and 3.15 mm and 3.11 mm in reality (two copies ordered).

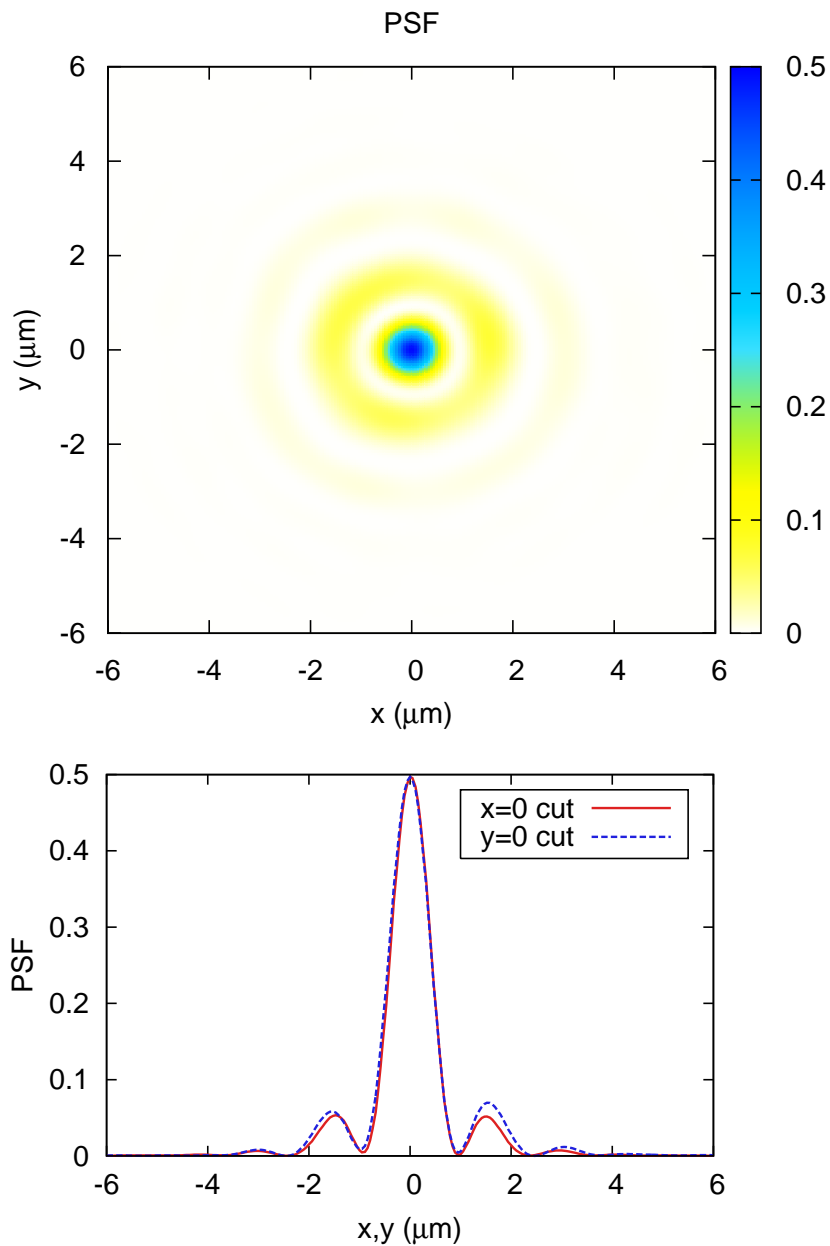


Figure 7.8.: Test 1: the measured PSF and its cuts along $x = 0$ and $y = 0$ on axis. Here, x and y (in this context) refer to the two transverse directions orthogonal to the optical axis. The rather good symmetry of revolution of the PSF suggests a residual spherical aberration and a slight decenter aberration, indicating that the mechanical parts are well within the tolerance. The spherical aberration can be explained by a slightly thicker window and the fact that the test is not carried out at the design wavelength.

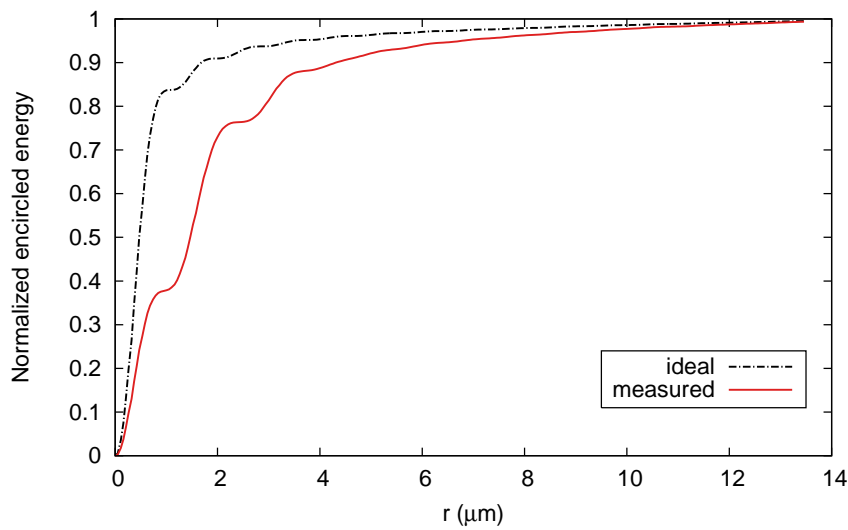


Figure 7.9.: Test 1: the measured normalized encircled energy. The measurement (solid line) on axis is compared with ideal performance (dash-dotted line). The difference can be explained by a slightly thicker window and the fact that the test is not carried out at the design wavelength.

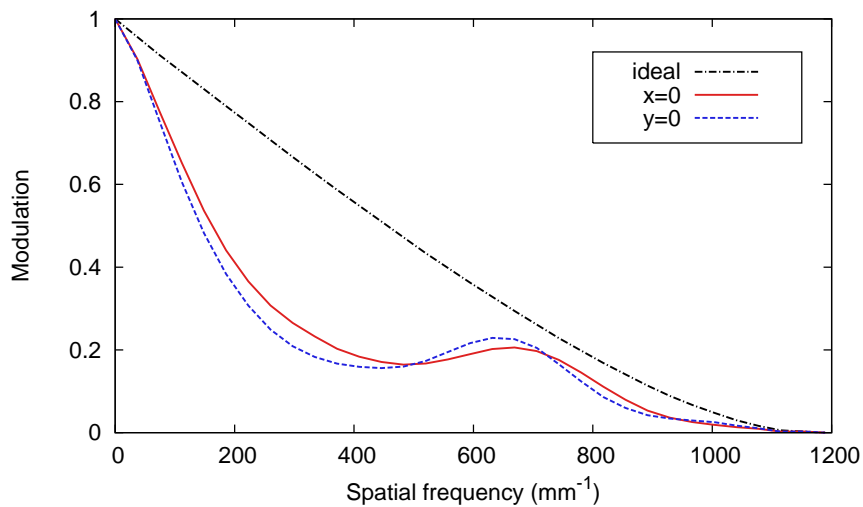


Figure 7.10.: Test 1: the measured modulation transfer function on axis along the two transverse directions x and y orthogonal to the optical axis. The measurements (solid and dashed lines) are compared with the ideal performance (dash-dotted line). The difference can be explained by a slightly thicker window and the fact that the test is not carried out at the design wavelength.

7.3.3.2. Test 2: measuring the point spread function

Considerations

On the other hand, the larger window thickness is not expected to cause such a dramatic change at the design wavelength, according to the simulations performed in OSLO. In order to verify this experimentally, I performed additional tests directly at $\lambda = 780 \text{ nm}$.

Submicron defects can be found in a thin layer of metal deposition (e.g. aluminium deposited on a glass slide). Since our new objective has $r_{\text{PSF}} = 1.2 \mu\text{m}$ in the object plane, finer structures will not be resolved and their images give the PSF of the objective directly. The schematic depicted in Fig. 7.11 allows the imaging of such pin holes on the CCD camera at 780 nm.

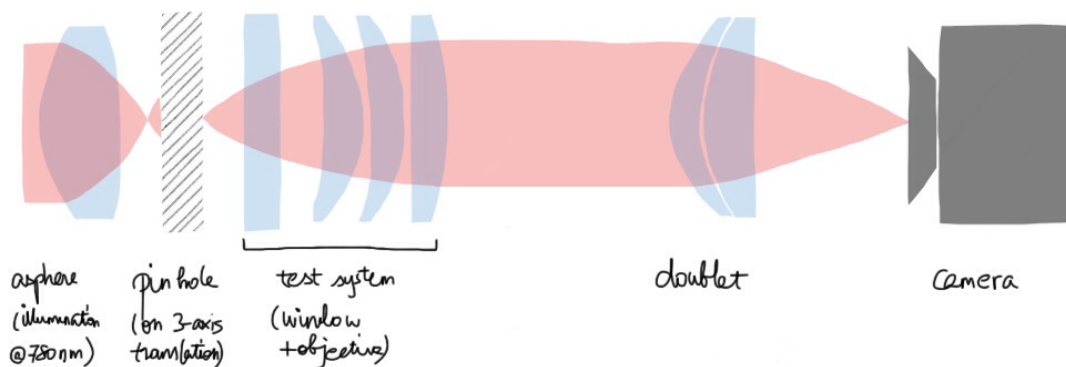


Figure 7.11.: Schematic of the PSF measurement. A microscope slide^a with sub-micron pin holes is mounted on a three-axis translation stage, and is illuminated by laser light at 780 nm focused using an asphere^b. The slide is positioned in the vicinity of the focal point of the window-objective system. A doublet^c is then used to image the PSF on the camera^d.

^aproduced in the clean-room facility at the institute.

^bAsphericon SPA 30-26 HPX, NA = 0.51.

^c $f = 500 \text{ mm}$, giving an expected magnification of $M = -14.3$ for infinity conjugation. The negative sign arises from the fact that the system is converging.

^dPixelfly QE 12 bit.

This test also permits the experimental determination of the diffraction limited field of view. Assuming the on-axis performance is ideal, the field is given by maximal transverse displacement of the pin hole that yields a $\leq 20\%$ reduction of the PSF peak intensity.

Procedures

Using the three-axis translation stage, we scan and record the PSF along three orthogonal directions in the vicinity of the focal point²³ of the objective. The camera is refocused for each image in order to account for a slight misalignment between the translation stage and the optical axis of the objective,

For each image of the PSF, we subtract the background, and normalize the peak intensity by the total intensity²⁴ in order to reduce the effect of the nonuniform illumination²⁵. The transverse scans then yield both the magnification and the field of view, while the longitudinal scan gives the tolerance of the working distance.

Outcome

I present the test results here: the PSF on axis in Fig. 7.12, the scans of the normalized peak intensity are shown in Fig. 7.13, and the PSF at the maximal transverse and longitudinal displacement while retaining a diffraction limited performance in Fig. 7.14. Again, the 3.15 mm thick window is used here, giving the worse-case scenario.

Comparing Fig. 7.12 with Fig. 7.8, we see that the spherical aberration is much reduced at 780 nm as expected. Instead, a slight decentering coma remains, most likely as a consequence of a slight misalignment of the three lens elements within the mounting tube.

Figure 7.13 shows the scans of the normalized PSF peak intensity along three orthogonal directions near the focal point of the objective. The transverse scans (circles and squares) show that the normalized PSF peak intensity decreases smoothly²⁶ away from the center of the field, and remain above 0.8 for about

²³which is the ideal location of the atoms.

²⁴The total intensity is obtained by integrating a sufficiently large area of the image that contains the PSF after the background subtraction. The convergence of the integral regardless of the size of the integration area is used as a criterion to precisely determine the value of the background.

²⁵likely as a result of unintentional diaphragming of the beam. We measure intensity fringes of $\sim 200 \mu\text{m}$ spatial period and $\sim 60\%$ visibility. Without normalization, these fringes would have masked the degradation of the PSF peak intensity due to the optical response of the objective (typically up to $\sim 40\%$).

²⁶The residual noise corresponds to an incomplete removal of the effects due to the nonuniform illumination, as the position of the sudden dips of the normalized PSF peak intensity coincides

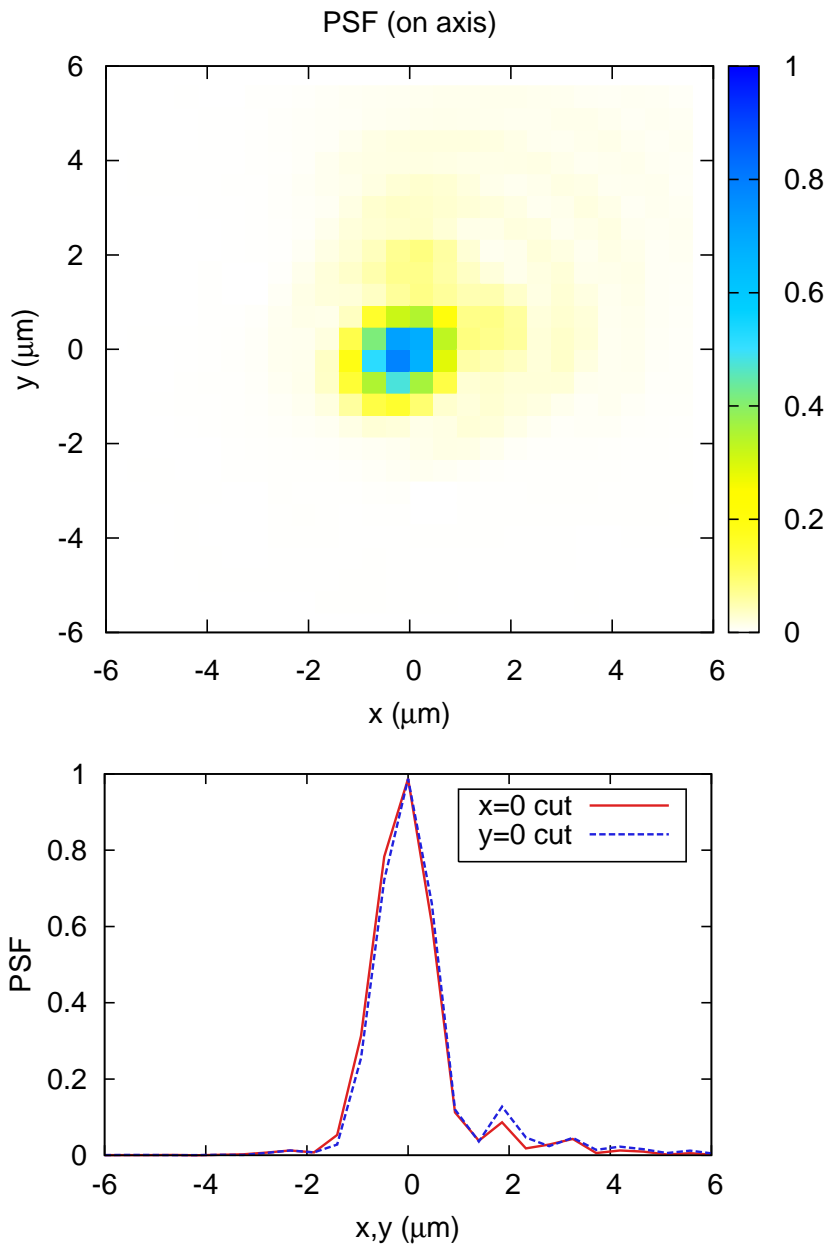


Figure 7.12.: Test 2: the measured PSF on axis and its cuts along $x = 0$ and $y = 0$ on axis. The notation is the same as Fig. 7.8. In comparison, the spherical aberration is much reduced at 780 nm. Instead, a slight decentering coma remains, but is uniform throughout the field (see Figs. 7.14).

$\pm 350 \mu\text{m}$. In terms of the homogeneity of the response, it is comparable to the simulated $\pm 245 \mu\text{m}$ at the best focus (see Sec. 7.3.3.1). The longitudinal scan (triangles) indicates that it is possible to defocus²⁷ about $\pm 250 \mu\text{m}$ while retaining

with that of the weaker illumination.
²⁷provided the CCD camera is refocused.

a diffraction limited imaging. This gives the tolerance on the working (atom-objective) distance.

These scans also confirm that the residual decentering coma is a minor effect, and is uniform throughout the region of space where the imaging is diffraction limited. Figure 7.14 shows two sample images of the PSF, taken at the maximal transverse and longitudinal displacement where the reduction of the PSF peak intensity is just about 20% (worst cases acceptable). Apart from the peak intensity reduction, these samples of PSF appear nearly identical to the PSF on axis, indicating a homogeneous spatial resolution of the objective. This also permits the possibility to deconvolve the experimental images with the measured PSF in order to reduce the effects of the residual decentering coma whenever necessary.

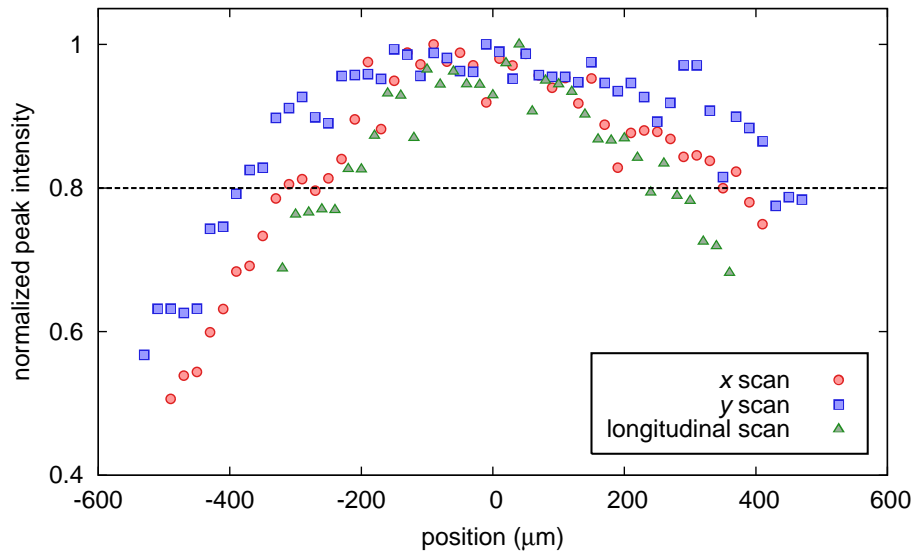


Figure 7.13.: Test 2: scan of the normalized PSF peak intensity in the vicinity of the focal point. Assuming an ideal performance in the center, a 20% reduction in the PSF peak intensity (dashed line) can be used as a criterion to identify the region of space where the imaging remains diffraction limited. The transverse scans indicate a diffraction limited field of view of $\sim \pm 350 \mu\text{m}$. The longitudinal scan indicates a tolerance of the working distance.

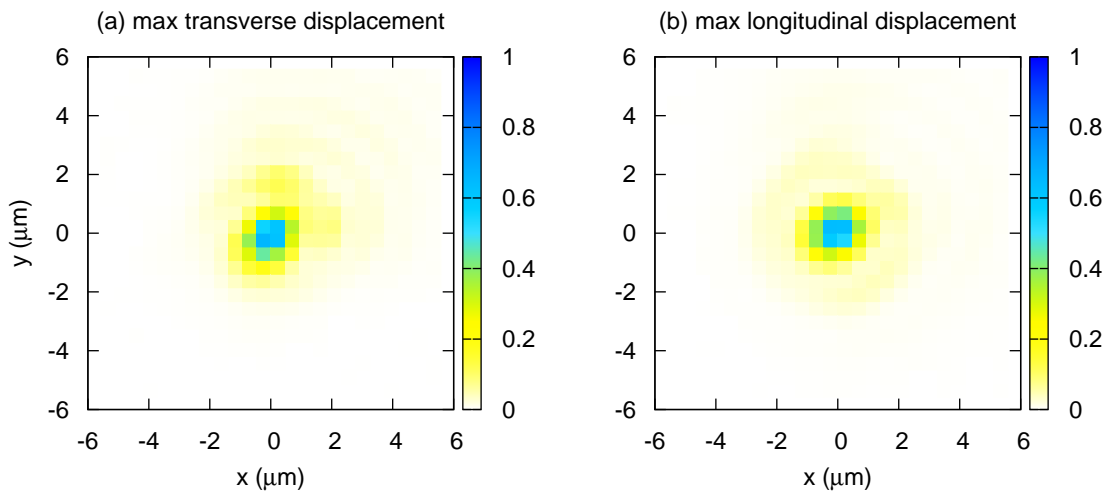


Figure 7.14.: Test 2: the measured PSF at the maximal transverse (off axis) and longitudinal displacement. Apart from the peak intensity reduction, these samples of PSF appear nearly identical to the PSF on axis, indicating a homogeneous performance of the objective over the field of view.

Conclusions

In this chapter, I have reported the optical design, mechanical assembly, and optical characterization of our new imaging objective. It is designed and optimized at 780 nm, and has an object NA= 0.385, now comparable to other ultracold atom experiments using home-made imaging systems. It operates *ex vacuo*, and enables diffraction limited imaging with an improved resolution of $r_{\text{PSF}} = 1.2 \mu\text{m}$ homogeneously over a field of view of $\pm 350 \mu\text{m}$. I have experimentally characterized its performance using two independent methods, confirming the simulated behavior.

8. Other Technical Upgrades

Contents

8.1. About the atom chip	153
8.1.1. New layout	154
8.1.2. Exploring alternative fabrication processes	154
8.2. There is more light!	157
8.2.1. Hybrid magneto-optical potential	157
8.2.2. Updating the existing laser system	159

In addition to the new imaging system, our experiment is also going through other technical upgrades aimed at improving the stability as well as the versatility of the experimental control. In this chapter, I record some of the changes that have taken place or are in the process of being implemented. They concern two aspects of the setup: the atom chip itself in Sec. 8.1 and the expanded laser system in Sec. 8.2.

8.1. About the atom chip

The new generation of the atom chip is modified in two aspects: its layout as well as the processes involved in the fabrication.

8.1.1. New layout

The new imaging objective has a diffraction limited field of view of at least¹ $\pm 350 \mu\text{m}$. Still, $350 \mu\text{m}$ is a small distance compared to the displacement ($\simeq 700 \mu\text{m}$) of the current trap position from the optical axis. This calls for a change in the chip design. I show in Fig. 8.1 both the existing (top) and the new (bottom) designs. The white area will be deposited with gold whereas the dark area indicates electrical insulation. Both the full view (left) and a zoom on the final trap position (right) are shown. In the new design, the final trap is centered on the chip, which will in turn be centered with respect to the vacuum chamber up to a few hundred microns. The objective will be mounted on a three-axis translation stage for the final alignment. The fabrication process of the new chips is ongoing.

In addition, the new design has implicitly centered the final modulated guide with the static magnetic trap, which is centered on the chip. This will hopefully reduce the loss during the transfer between the two traps and allow for a larger dynamical range of the total atom number in the final trap.

8.1.2. Exploring alternative fabrication processes

The successful fabrication of the atom chips depends heavily on the maturity of the processes involved. One could in principle rely on standard material and processes in order to ensure the fabrication yield. On the other hand, less standard processes may sometimes lead to unprecedented performance. As the very conception of the atom chip hopes to integrate more than just microelectronics [51, 53], it is important to continue refining the procedures and techniques involved in fabrication.

In our case, the change of the chip design presents the perfect opportunity to explore new processes. I list a few aspects that are being pursued right now.

¹A trade off can be made to increase the field of view at a slight cost of the on-axis performance. Depending on the magnification, the degradation on axis may not impact the actual imaging system.

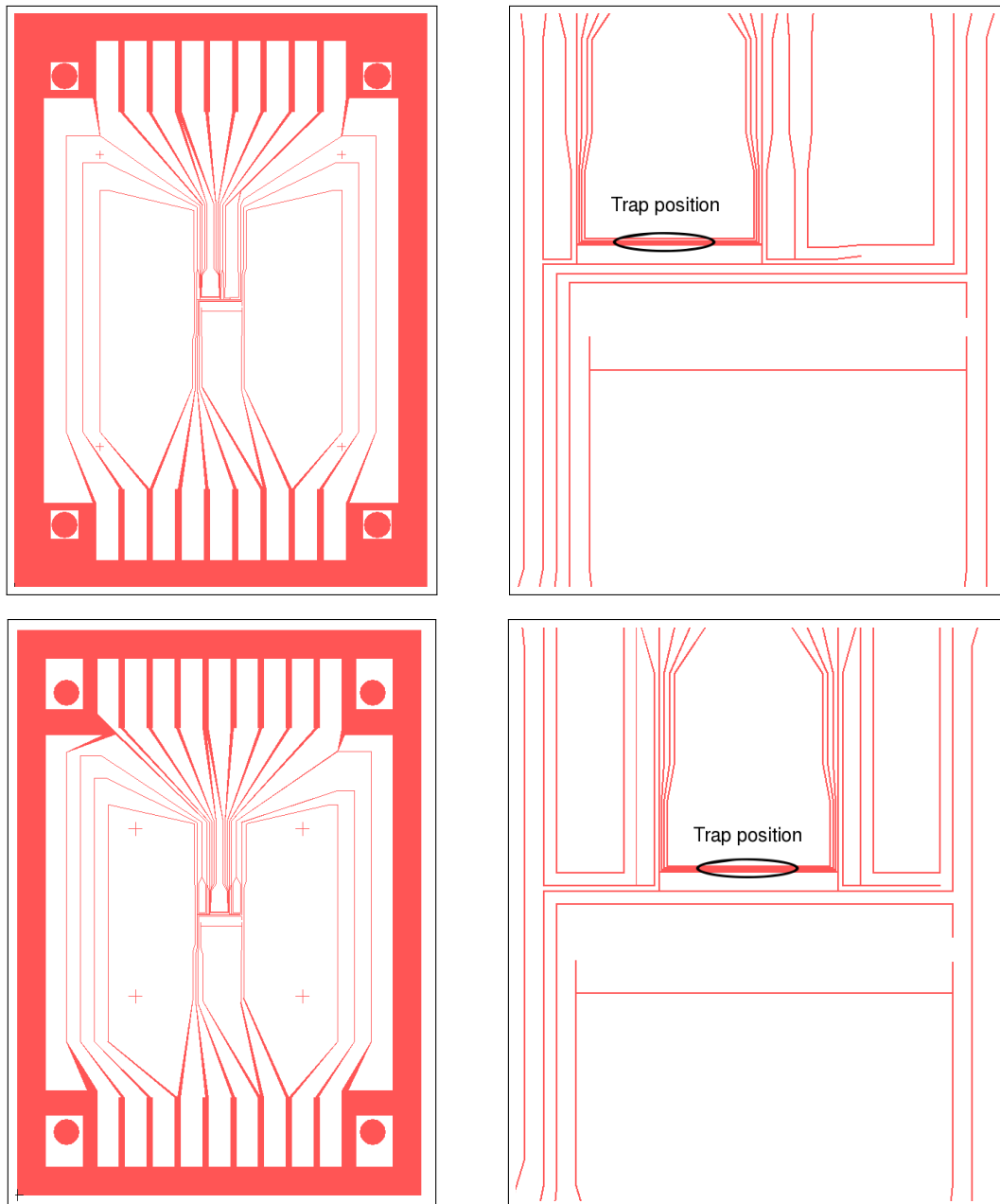


Figure 8.1.: The existing (top) and new (bottom) chip designs. Both the full layout (left) and a zoom (right) showing the atom-trapping wires are shown. The entire chip spans $2.5 \times 3.5 \text{ cm}^2$.

Change of substrate

As mentioned in Sec. 1.2, the AlN substrates that we purchase come with a variable grain size that is beyond our control. Despite its excellent thermal properties [8], our experience indicates that samples with a grain-size beyond $\sim 100 \text{ nm}$ would result in too much potential corrugation, since the shape of the surface mounted wire structures will be irregular. Silicon substrate has been a common

choice among the atom-chip experiments precisely for its flatness. Being a semiconductor, however, it requires a thin electrical insulation layer to reduce current leakage. This is often achieved with ~ 200 nm of silicon oxide, which prevents efficient heat dissipation [68] and in turn restricts the maximal current density that is non-destructive.

Silicon carbide (SiC) is a semiconductor that is now routinely manufactured into wafers for its application in electronic devices and circuits [112]. Such wafers have excellent surface flatness. Since SiC has a larger band gap than Si (see Tab. 8.1), there is a possibility to use SiC as a substrate without an electrical insulation layer. This would require wafers of high purity that are costly. Alternatively, a thin layer (~ 100 nm) of AlN can be deposited to provide the necessary electrical insulation without creating a thermal bottle neck². Both options are being tested right now during the fabrication of the new chip. Note that SiC is also used in the atom-chip experiment at Thales [77], where a conventional six-beam MOT is implemented given the transparency of SiC.

Material	Thermal conductivity at 20°C (W m ⁻¹ K ⁻¹)	Band gap (eV)
AlN	170-180	6.2
Si	80-150	1.12
SiC	360-490	2.4-3.2
SiO ₂	1.46	large

Table 8.1.: Thermal and electrical properties of some materials as potential substrates. Data are harvested from Refs. [112, 121]. The entry for SiC only accounts for three common crystalline structures. It is to be understood as an estimate rather than a precise value.

Protecting the gold mirror

The surface of our chip is coated with a thin layer of gold for its excellent reflectance. Unfortunately, gold is known to be a getter of Rb. Over time, we see the gradual development of a potential bump associated with the usual trap position, most likely due to Rb adsorption³.

²Thin-film AlN has a grain size much smaller than the layer thickness.

³Recall that our usual trap position is merely a few μm away from the chip, so that a small

Given that our chip is operated at room temperature, the mechanism governing the Rb adsorption is most likely chemisorption [32], where chemical bonds are formed between the surface and adsorbate due to their comparable work function (~ 5 eV for gold and 2.26 eV for Rb). Prevention then calls for coating the gold surface with a material of dramatically different work function, while preserving the reflectance of the surface at 780 nm.

A few candidates are possible. SiO₂ deposition is available at Laboratoire de Photonique et de Nanostructure⁴. Since SiO₂ is transparent at 780 nm, it is expected not to modify the reflectance. One attempt was made during the previous fabrication exercise in 2012. The resultant chip was however damaged soon after its installation, possibly caused by the incompatibility of the rigidity of SiO₂ and a strong thermal deformation of the underlying resist⁵ when electrical currents were sent through the on-chip wires. More attempts will be made now with the new chips, paying special attention to fully bake the PMMA, and/or to use a more rigid resist, e.g. benzocyclobutene (BCB). Looking forward, there may also be the possibility to deposit amorphous carbon or sapphire of ~ 10 nm thickness⁶, which should limit the absorption at 780 nm while keeping the gold mirror intact. As the process is more experimental, an old chip would be used for testing at this stage.

8.2. There is more light!

8.2.1. Hybrid magneto-optical potential

A telecomm laser at 1530 nm is being added on the setup to form a 1D optical lattice in the longitudinal direction of the magnetic confinement. The availability of a periodic potential allows for the realization of the lattice Boson models, hence expanding the versatility of the current setup. Technically, such a lattice may

amount of adsorbed Rb is sufficient to cause potential irregularities.

⁴Route de Nozay, 91460 Marcoussis, France

⁵Poly(methyl methacrylate) (PMMA) was used. There is evidence that it was underbaked and therefore softer than usual.

⁶under discussion with Dr. Joakim Andersson and Dr. Björn Hessmo, Centre for Quantum Technologies, National University of Singapore, 3 Science Drive 2, Singapore 117543, Singapore.

also act as a pinning device that prevents the longitudinal motion of the atoms during a transverse compression, which is a crucial step in order to achieve large interaction strength on our current setup.

Other forms of optical potential engineering are possible. For instance, taking advantage of the transverse magnetic guide available on our set up, a homogeneous 1D trap can be formed by superposing optical ‘end-plugs’ on to the wave guide. This can be achieved by means of a phase plate [33, 120] or simply imaging a dark area onto the atoms. The advantage of such a hybrid box trap is that the separation of the end-plugs and thus the size of the 1D box can be easily adjusted⁷. There is also the possibility of spatial selection using a (resonant) cleaning beam, so that Mott insulator states with lower (the outer regions of the atomic cloud) or higher (near the center of the atomic cloud) occupancy can be blasted away before imaging (see Fig. 8.2). The first step of a feasibility study has been developed during the internship of Ms. Laëtitia Farinacci [49].

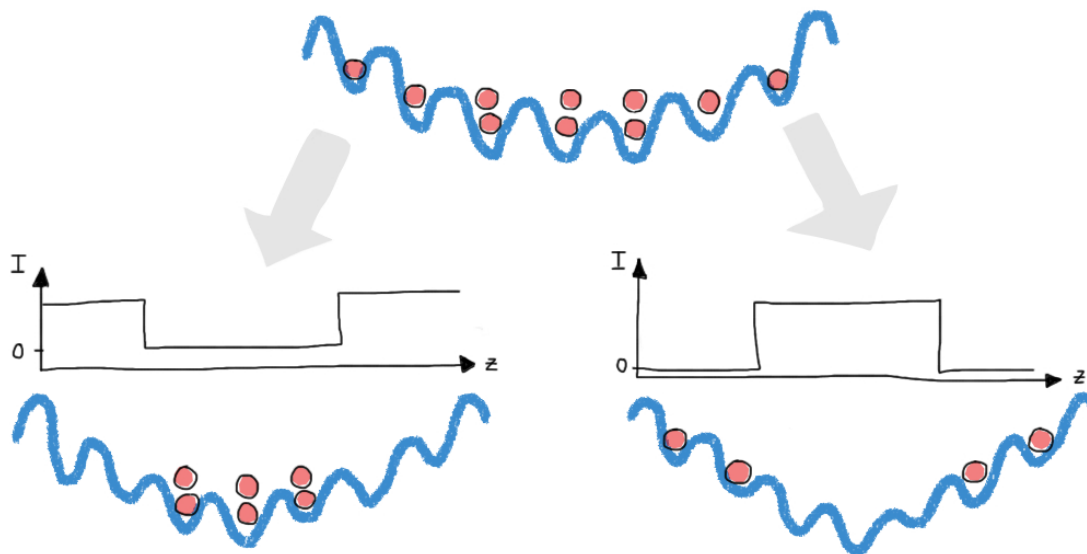


Figure 8.2.: An illustration of optical potentials for spatial selection. I denotes the intensity of the selection beam, and thus the optical potential depth.

⁷In a similar spirit, a magnetic quartic potential has been realized on our setup [82]. However, its applicability to actual measurements is limited as acceptable current values tend to yield a box too large for the typical number of atoms accessible.

8.2.2. Updating the existing laser system

The stability and maximal continuous run time of our current setup are mostly limited by the laser system. On a short time scale, the spectroscopically locked master laser is susceptible to acoustic vibrations. On a long time scale, the alignment of the cooling light which propagates in free space becomes sensitive to changes of the temperature and the humidity. It is certainly up to the operator of the experiment to keep various components at optimal working condition. Yet, improving the hardware is always welcome. Here, I mention two such improvements on the laser system that are carried out in the lab right now.

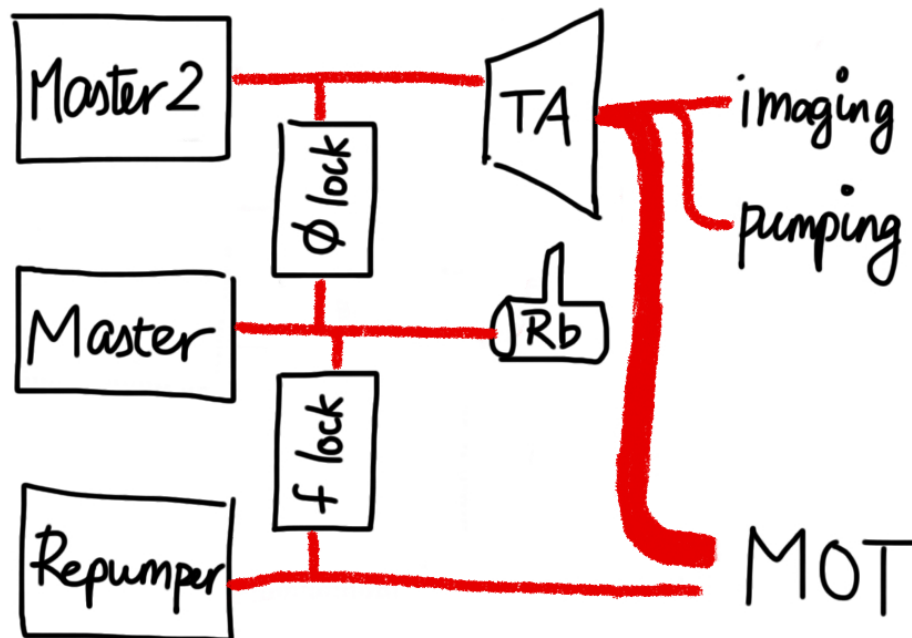


Figure 8.3.: A schematic of the new laser system that is currently being installed.

- A fibered beam splitter will be installed to replace the existing splitter cluster in free space, with outcouplers to be installed directly outside the experimental chamber, thereby eliminating most of the free optics in the cooling path.
- Taking into account potential losses due to fiber injection, the laser system will be slightly modified according to Fig. 8.3. The additional Master 2 laser (M2) will act as the seed for the TA, which will provide light necessary for cooling, optical pumping and imaging. The implementation of the

phase lock between Master and M2 allows an arbitrary frequency offset and sweeps of M2 up to a few GHz [7] with a constant intensity, an essential requirement for constant output power of the TA. The repumper laser will soon be replaced by a DFB laser to supply sufficient power ($\gtrsim 20$ mW before the fiber injection).

Conclusions

In this chapter, we have seen the ongoing technological progress to improve both the atom chip and the laser system of our experiment. Once implemented, these changes will likely improve both the stability and versatility of the experimental setup.

Concluding Remarks

In this thesis, I have presented a study of equilibrium and nonequilibrium behaviors of 1D Bose gases. The experiments performed in this study were carried out on an atom-chip setup at Institut d'Optique, Palaiseau. The setup is able to produce single samples of harmonically trapped, (nearly) 1D Bose gas of ^{87}Rb at tens to hundreds of nK, allowing a prototypical realization of the Lieb-Liniger model.

The equilibrium behavior of 1D Bose gases are fairly well understood theoretically. Its thermodynamic properties are described by the celebrated Yang-Yang equation of state, which is analytic and exact. Powerful numerical tools such as the Quantum Monte Carlo calculations can be used to compute quantities of interest that go beyond the equation of state. In addition, various approximate theory tools exist in their respective domains of validity in the interaction-temperature phase diagram. Such impressive developments have set the stage for quantitative characterizations of experimental realizations of the Lieb-Liniger gas.

In Chapter 3, I have given an overview of the various probes that can be used to quantitatively characterize a single realization of harmonically confined 1D Bose gases at thermal equilibrium. The development of these tools is a joint effort among several experiments with similar setups (making use of atom chips), and spans from around 2006 to date. My discussions focused on the direct application of these tools and methods for thermometry. I also demonstrated the very first momentum correlation measurements performed on such a system. We are currently working on its application as a quantitative characterization tool, a thermometry method in particular.

The ability to quantitatively characterize the 1D Bose gases at (near) equilibrium allows for further investigation of their nonequilibrium behavior. Indeed, the realization of a Lieb-Liniger gas with ultracold atoms constitutes a prime candidate for quantum simulation given the degree of isolation and controllability. It promises the potential to address interesting questions, such as the propagation of elementary excitations in an inhomogeneous medium (dynamic Casimir effect), and the relaxation and thermalization processes (or their absence) in an integrable quantum many-body system.

I performed the following experiments in this direction:

1. A joint theoretical and experimental study of the breathing mode, focusing on quantitative characterization of such a collective excitation in terms of its frequency and lifetime signatures.
 - The frequency signature was probed in various asymptotic regimes and crossovers in the interaction-temperature phase diagram.
 - The measured frequency in real space agrees with existing theoretical predictions in the asymptotic limits.
 - Two finite-temperature models are proposed for the real-space breathing frequency in the quasicondensate to Ideal Bose gas crossover, and I show their qualitative agreement with experimental data.
 - A momentum-space frequency doubling is demonstrated experimentally for the first time.
 - We understand that a self-reflection mechanism induced by the repulsive interaction is responsible for such a signature.
 - I presented an experimental investigation of the disappearance of the self-reflection through the quasicondensate to ideal Bose gas crossover. A possible theoretical description and extensions are proposed.
 - I also investigated the variation of the lifetime through the 1D-3D dimensional crossover. Theory models are currently under development.

2. I probed and characterized a 'two-temperature' phenomenon often seen on our experiment.
 - I described its usual characteristics in terms of the apparent profile temperature and fluctuation temperature using the respective thermometries introduced in Ch. 3.
 - I attempted to vary its characteristics by controlling the waiting time and the evaporation parameters. I have shown that the disagreement between the two apparent temperatures is robust and long-lived.

-
- I discussed possible technical and physical causes, and proposed an extension of this work.
3. I attempted experiments that investigate the evolution of a system deliberately brought far away from equilibrium.
- An analog of parametric amplification in nonlinear optics indicates that the excitation of well-defined phonon modes for a quasicondensate near the quasicondensate to ideal Bose gas crossover is nearly impossible.
 - An interaction double quench leads to a small-amplitude breathing mode in the long run. Its real-space behavior agrees with our characterization in Ch. 4. There are interesting signals in the momentum-space behavior that deserve further exploration. The short-time evolution has not been accessible up to March 2014 due to technical constraints.
 - Slow interaction ramps result in the destruction of the *anticorrelations* between equal but opposite momenta. The analysis of the effect of the ramp duration is pending the construction of a single meaningful quantity of the momentum correlation matrix.

The study of nonequilibrium physics on our experimental setup is still in its infancy. With the information we have gathered thus far and the on-going technical improvements on the setup detailed in Part III, the following perspectives are within reach:

- The modeling of the breathing lifetime, together with possible future experiments, could give access to the physical mechanisms that cause the lifetime variations observed in Sec. 4.4. Its potential connection with integrability and thermalization [94] is worth pursuing.
- The impossibility to excite well-defined phonon modes (of energy much above the collective breathing mode but comparable to the speed of sound) may be related to both the response (susceptibility) of the system (medium) and the lifetime of such excitations. This is in stark contrast with the observation of correlated excitation pairs reported in [85] by the metastable

helium experiment in our group. These two experimental setups differ in the effective interaction parameter due to the different mass of the atomic species. A joint effort may give experimental access to the intermediate behavior (matching the interacting parameter by tuning the linear density), thus probing the phonon lifetime in a 1D system that has been hard to access otherwise.

- The short-time evolution after an interaction double quench may reveal propagation of excitations similar to those reported in [34, 100]. The improved imaging resolution promised by the new objective will give access to finer details in the measured correlations.
- Once a quantitative probe can be formulated from the momentum correlation measurements, we will be in a position to find out the effect of the time scale defined by the interaction ramp. This may in turn address questions such as the breaking of adiabaticity.

Bibliography

- [1] “Contact mechanics”, Wikipedia.
- [2] “Fraunhofer lines”, Wikipedia.
- [3] ABRAMOWITZ, M. and STEGUN, I., *Handbook of Mathematical Functions with Formulas, Graphs, and Mathematical Tables*. Dover Publications, 1964.
- [4] ALT, W., “An objective lens for efficient fluorescence detection of single atoms,” *Optik - International Journal for Light and Electron Optics*, vol. 113, no. 3, pp. 142–144, 2002.
- [5] AMERONGEN, A. V., *One-dimensional Bose gas on an atom chip*. PhD thesis, Universiteit van Amsterdam, Amsterdam, 2008.
- [6] ANDERSON, M. H., ENSHER, J. R., MATTHEWS, M. R., WIEMAN, C. E., and CORNELL, E. A., “Observation of Bose-Einstein condensation in a dilute atomic vapor,” *Science*, vol. 269, pp. 198–201, July 1995.
- [7] APPEL, J., MACRAE, A., and LVOVSKY, A. I., “A versatile digital GHz phase lock for external cavity diode lasers,” *Measurement Science and Technology*, vol. 20, p. 055302, May 2009.
- [8] ARMIJO, J., ALZAR, C. L. G., and BOUCHOULE, I., “Thermal properties of AlN-based atom chips,” *The European Physical Journal D*, vol. 56, pp. 33–39, Jan. 2010.
- [9] ARMIJO, J., JACQMIN, T., KHERUNTSYAN, K., and BOUCHOULE, I., “Mapping out the quasicondensate transition through the dimensional crossover from one to three dimensions,” *Physical Review A*, vol. 83, p. 021605, Feb. 2011.

- [10] ARMIJO, J., JACQMIN, T., KHERUNTSYAN, K. V., and BOUCHOULE, I., "Probing three-body correlations in a quantum gas using the measurement of the third moment of density fluctuations," *Physical Review Letters*, vol. 105, p. 230402, Nov. 2010.
- [11] ARMIJO, J., *Fluctuations de densité dans des gaz de bosons ultrafroids quasi-unidimensionnels*. PhD thesis, Université Paris Sud - Paris XI, May 2011.
- [12] AUSSIBAL, C., *Réalisation d'un condensat de Bose-Einstein sur une microstructure*. PhD thesis, Université Paris Sud - Paris XI, Nov. 2003.
- [13] BENNIE, L. M., STARKEY, P. T., JASPERSE, M., BILLINGTON, C. J., ANDERSON, R. P., and TURNER, L. D., "A versatile high resolution objective for imaging quantum gases," *Optics Express*, vol. 21, pp. 9011–9016, Apr. 2013.
- [14] BERNIER, J.-S., CITRO, R., KOLLATH, C., and ORIGNAC, E., "Correlation dynamics during a slow interaction quench in a one-dimensional Bose gas," *arXiv:1308.4699 [cond-mat]*, Aug. 2013.
- [15] BLOCH, I., DALIBARD, J., and ZWERGER, W., "Many-body physics with ultracold gases," *Reviews of Modern Physics*, vol. 80, pp. 885–964, July 2008.
- [16] BOTHNER, D., KNUFINKE, M., HATTERMANN, H., WÖLBING, R., FERDINAND, B., WEISS, P., BERNON, S., FORTÁGH, J., KOELLE, D., and KLEINER, R., "Inductively coupled superconducting half wavelength resonators as persistent current traps for ultracold atoms," *New Journal of Physics*, vol. 15, p. 093024, Sept. 2013.
- [17] BOUCHOULE, I., ARZAMASOV, M., KHERUNTSYAN, K. V., and GANGARDT, D. M., "Two-body momentum correlations in a weakly interacting one-dimensional Bose gas," *Physical Review A*, vol. 86, p. 033626, Sept. 2012.
- [18] BOUCHOULE, I., KHERUNTSYAN, K. V., and SHLYAPNIKOV, G. V., "Interaction-induced crossover versus finite-size condensation in a weakly interacting trapped one-dimensional Bose gas," *Physical Review A*, vol. 75, p. 031606, Mar. 2007.
- [19] BOUCHOULE, I., VAN DRUTEN, N. J., and WESTBROOK, C. I., "Atom chips and one-dimensional Bose gases," in *Atom chips, Chapter 11* (REICHEL, J. and VULETIC, V., eds.), Weinheim: Wiley-VCH Verlag GmbH, 2011.

- [20] BRADLEY, C. C., SACKETT, C. A., TOLLETT, J. J., and HULET, R. G., "Evidence of Bose-Einstein condensation in an atomic gas with attractive interactions," *Physical Review Letters*, vol. 75, pp. 1687–1690, Aug. 1995.
- [21] BRETIN, V., ROSENBUSCH, P., CHEVY, F., SHLYAPNIKOV, G. V., and DALIBARD, J., "Quadrupole oscillation of a single-vortex Bose-Einstein condensate: Evidence for kelvin modes," *Physical Review Letters*, vol. 90, p. 100403, Mar. 2003.
- [22] BÜCKER, R., PERRIN, A., MANZ, S., BETZ, T., KOLLER, C., PLISSON, T., ROTTMANN, J., SCHUMM, T., and SCHMIEDMAYER, J., "Single-particle-sensitive imaging of freely propagating ultracold atoms," *New Journal of Physics*, vol. 11, p. 103039, Oct. 2009.
- [23] BUSCH, T., ENGLERT, B.-G., RZAŻEWSKI, K., and WILKENS, M., "Two cold atoms in a harmonic trap," *Foundations of Physics*, vol. 28, pp. 549–559, Apr. 1998.
- [24] CARLEO, G., in preparation, 2014.
- [25] CARUSOTTO, I., BALBINOT, R., FABBRI, A., and RECATI, A., "Density correlations and analog dynamical casimir emission of bogoliubov phonons in modulated atomic Bose-Einstein Condensates," *The European Physical Journal D*, vol. 56, pp. 391–404, Feb. 2010.
- [26] CASTIN, Y., "Simple theoretical tools for low dimension Bose gases," *Journal de Physique IV (Proceedings)*, vol. 116, pp. 89–132, Oct. 2004.
- [27] CASTIN, Y. and DUM, R., "Bose-Einstein condensates in time dependent traps," *Physical Review Letters*, vol. 77, pp. 5315–5319, Dec. 1996.
- [28] CASTIN, Y., DUM, R., MANDONNET, E., MINGUZZI, A., and CARUSOTTO, I., "Coherence properties of a continuous atom laser," *Journal of Modern Optics*, vol. 47, no. 14-15, pp. 2671–2695, 2000.
- [29] CAZALILLA, M. A., "Bosonizing one-dimensional cold atomic gases," *Journal of Physics B: Atomic, Molecular and Optical Physics*, vol. 37, p. S1, Apr. 2004.

- [30] CAZALILLA, M. A., CITRO, R., GIAMARCHI, T., ORIGNAC, E., and RIGOL, M., "One dimensional bosons: From condensed matter systems to ultra-cold gases," *Reviews of Modern Physics*, vol. 83, pp. 1405–1466, Dec. 2011.
- [31] CAZALILLA, M. A., HO, A. F., and GIAMARCHI, T., "Interacting Bose gases in quasi-one-dimensional optical lattices," *New Journal of Physics*, vol. 8, p. 158, Aug. 2006.
- [32] CHAN, K. S., SIERCKE, M., HUFNAGEL, C., and DUMKE, R., "Adsorbate electric fields on a cryogenic atom chip," *Physical Review Letters*, vol. 112, p. 026101, Jan. 2014.
- [33] CHENEAU, M., *Transition superfluide et potentiels géométriques dans le gaz de Bose bidimensionnel*. PhD thesis, Université Pierre et Marie Curie - Paris VI, July 2009.
- [34] CHENEAU, M., BARMETTLER, P., POLETTI, D., ENDRES, M., SCHAUSS, P., FUKUHARA, T., GROSS, C., BLOCH, I., KOLLATH, C., and KUHR, S., "Light-cone-like spreading of correlations in a quantum many-body system," *Nature*, vol. 481, pp. 484–487, Jan. 2012.
- [35] CHEVY, F., BRETIN, V., ROSENBUSCH, P., MADISON, K. W., and DALIBARD, J., "Transverse breathing mode of an elongated Bose-Einstein condensate," *Physical Review Letters*, vol. 88, p. 250402, June 2002.
- [36] COLOMBE, Y., STEINMETZ, T., DUBOIS, G., LINKE, F., HUNGER, D., and REICHEL, J., "Strong atom-field coupling for Bose-Einstein condensates in an optical cavity on a chip," *Nature*, vol. 450, pp. 272–276, Nov. 2007.
- [37] CRONIN, A. D., SCHMIEDMAYER, J., and PRITCHARD, D. E., "Optics and interferometry with atoms and molecules," *Reviews of Modern Physics*, vol. 81, pp. 1051–1129, July 2009.
- [38] DAVIS, K. B., MEWES, M. O., ANDREWS, M. R., VAN DRUTEN, N. J., DUFFEE, D. S., KURN, D. M., and KETTERLE, W., "Bose-Einstein condensation in a gas of sodium atoms," *Physical Review Letters*, vol. 75, pp. 3969–3973, Nov. 1995.
- [39] DAVIS, M. J., BLAKIE, P. B., VAN AMERONGEN, A. H., VAN DRUTEN, N. J., and KHERUNTSYAN, K. V., "Yang-yang thermometry and momentum dis-

- tribution of a trapped one-dimensional Bose gas," *Physical Review A*, vol. 85, p. 031604, Mar. 2012.
- [40] DENSCHLAG, J., UMSHAUS, G., and SCHMIEDMAYER, J., "Probing a singular potential with cold atoms: A neutral atom and a charged wire," *Physical Review Letters*, vol. 81, pp. 737–741, July 1998.
- [41] DESBUQUOIS, R., CHOMAZ, L., YEFSAH, T., LÉONARD, J., BEUGNON, J., WEITENBERG, C., and DALIBARD, J., "Superfluid behaviour of a two-dimensional Bose gas," *Nature Physics*, vol. 8, pp. 645–648, Sept. 2012.
- [42] DEURETZBACHER, F., FREDENHAGEN, K., BECKER, D., BONGS, K., SENGSTOCK, K., and PFANNKUCHE, D., "Exact solution of strongly interacting quasi-one-dimensional spinor Bose gases," *Physical Review Letters*, vol. 100, p. 160405, Apr. 2008.
- [43] ES, J. J. P. v., WICKE, P., AMERONGEN, A. H. v., RÉTIF, C., WHITLOCK, S., and DRUTEN, N. J. v., "Box traps on an atom chip for one-dimensional quantum gases," *Journal of Physics B: Atomic, Molecular and Optical Physics*, vol. 43, p. 155002, Aug. 2010.
- [44] ESTEVE, J., TREBBIA, J.-B., SCHUMM, T., ASPECT, A., WESTBROOK, C. I., and BOUCHOULE, I., "Observations of density fluctuations in an elongated Bose gas: Ideal gas and quasicondensate regimes," *Physical Review Letters*, vol. 96, p. 130403, Apr. 2006.
- [45] ESTÈVE, J., *Du miroir au guide d'onde atomique : effets de rugosité*. PhD thesis, Université Pierre et Marie Curie - Paris VI, Nov. 2004.
- [46] FABBRI, N., CLÉMENT, D., FALLANI, L., FORT, C., and INGUSCIO, M., "Momentum-resolved study of an array of one-dimensional strongly phase-fluctuating Bose gases," *Physical Review A*, vol. 83, p. 031604, Mar. 2011.
- [47] FABBRI, N., HUBER, S. D., CLÉMENT, D., FALLANI, L., FORT, C., INGUSCIO, M., and ALTMAN, E., "Quasiparticle dynamics in a Bose insulator probed by interband bragg spectroscopy," *Physical Review Letters*, vol. 109, p. 055301, July 2012.

- [48] FANG, B., CARLEO, G., JOHNSON, A., and BOUCHOULE, I., "Quench-induced breathing mode of one-dimensional Bose gases," *Physical Review Letters*, vol. 113, p. 035301, July 2014.
- [49] FARINACCI, L., *Façonnage d'un potentiel pour l'étude de la transition de Mott d'un gaz bosonique unidimensionnel*. Master internship report, Ecole Polytechnique, 2014.
- [50] FEDICHEV, P. O., *Kinetics and Dynamics of Trapped Bose-condensed Gases*. PhD thesis, 1999.
- [51] FOLMAN, R., KRÜGER, P., CASSETTARI, D., HESSMO, B., MAIER, T., and SCHMIEDMAYER, J., "Controlling cold atoms using nanofabricated surfaces: Atom chips," *Physical Review Letters*, vol. 84, pp. 4749–4752, May 2000.
- [52] FOLMAN, R., KRÜGER, P., SCHMIEDMAYER, J., DENSCHLAG, J., and HENKEL, C., "Microscopic atom optics: From wires to an atom chip," *Advances in atomic, molecular, and optical physics*, vol. 48, p. 263, 2002.
- [53] FOLMAN, R., TREUTLEIN, P., and SCHMIEDMAYER, J., "Atom chip fabrication," in *Atom chips, Chapter 3* (REICHEL, J. and VULETIC, V., eds.), Weinheim: Wiley-VCH Verlag GmbH, 2011.
- [54] FORRESTER, P. J., FRANKEL, N. E., GARONI, T. M., and WITTE, N. S., "Finite one-dimensional impenetrable Bose systems: Occupation numbers," *Physical Review A*, vol. 67, p. 043607, Apr. 2003.
- [55] FORTÁGH, J., "Atoms in microtraps," in *McGraw-Hill Yearbook of Science and Technology*, McGraw-Hill 2013.
- [56] FORTÁGH, J., OTT, H., KRAFT, S., GÜNTHER, A., and ZIMMERMANN, C., "Bose-Einstein condensates in magnetic waveguides," *Applied Physics B*, vol. 76, pp. 157-163, Feb. 2003.
- [57] FORTÁGH, J., and ZIMMERMANN, C., "Magnetic microtraps for ultracold atoms," *Reviews of Modern Physics*, vol. 79, pp. 235–289, Feb. 2007.
- [58] FUCHS, J. N., LEYRONAS, X., and COMBESCOT, R., "Hydrodynamic modes of a one-dimensional trapped Bose gas," *Physical Review A*, vol. 68, p. 043610, Oct. 2003.

- [59] GAUDIN, M., *La fonction d'onde de Bethe*. Paris: Masson, 1983.
- [60] GERBIER, F., "Quasi-1D Bose-Einstein condensates in the dimensional crossover regime," *Europhysics Letters*, vol. 66, pp. 771–777, June 2004.
- [61] GERBIER, F., THYWISEN, J. H., RICHARD, S., HUGBART, M., BOUYER, P., and ASPECT, A., "Momentum distribution and correlation function of quasicondensates in elongated traps," *Physical Review A*, vol. 67, p. 051602, May 2003.
- [62] GIERLING, M., SCHNEEWEISS, P., VISANESCU, G., FEDERSEL, P., HÄFFNER, M., KERN, D. P., JUDD, T. E., GÜNTHER, A., and FORTÁGH, J., "Cold-atom scanning probe microscopy," *Nature Nanotechnology*, vol. 6, pp. 446–451, July 2011.
- [63] GILLESPIE, D. T., "Exact numerical simulation of the ornstein-uhlenbeck process and its integral," *Physical Review E*, vol. 54, pp. 2084–2091, Aug. 1996.
- [64] GIRARDEAU, M., "Relationship between systems of impenetrable bosons and fermions in one dimension," *J. Math. Phys.*, vol. 1, p. 516, Mar. 1960.
- [65] GIRARDEAU, M. D. and MINGUZZI, A., "Soluble models of strongly interacting ultracold gas mixtures in tight waveguides," *Physical Review Letters*, vol. 99, p. 230402, Dec. 2007.
- [66] GRING, M., KUHNERT, M., LANGEN, T., KITAGAWA, T., RAUER, B., SCHREITL, M., MAZETS, I., SMITH, D. A., DEMLER, E., and SCHMIEDMAYER, J., "Relaxation and prethermalization in an isolated quantum system," *Science*, vol. 337, pp. 1318–1322, Sept. 2012.
- [67] GROSS, H., *Handbook of Optical Systems: Aberration theory and correction of optical systems*, vol. 3. Wiley-VCH, 2007.
- [68] GROTH, S., KRÜGER, P., WILDERMUTH, S., FOLMAN, R., FERNHOLZ, T., MAHALU, D., BAR-JOSEPH, I., and SCHMIEDMAYER, J., "Atom chips: Fabrication and thermal properties," *Applied Physics Letters*, vol. 85, no. 14, p. 2980, 2004.

- [69] GUÉRY-ODELIN, D. and STRINGARI, S., "Scissors mode and superfluidity of a trapped Bose-Einstein condensed gas," *Physical Review Letters*, vol. 83, pp. 4452–4455, Nov. 1999.
- [70] GUÉRY-ODELIN, D., ZAMBELLI, F., DALIBARD, J., and STRINGARI, S., "Collective oscillations of a classical gas confined in harmonic traps," *Physical Review A*, vol. 60, pp. 4851–4856, Dec. 1999.
- [71] GÜNTHER, A., HÖLSCHER, H., and FORTÁGH, J., "Cold Atom Scanning Probe Microscopy: An Overview," in *Fundamentals of Picoscience* (SATTLER, K. D. ed.), Taylor & Francis, 2013
- [72] HAASE, A., CASSETTARI, D., HESSMO, B., and SCHMIEDMAYER, J., "Trapping neutral atoms with a wire," *Physical Review A*, vol. 64, p. 043405, Sept. 2001.
- [73] HALLER, E., GUSTAVSSON, M., MARK, M. J., DANZL, J. G., HART, R., PUPILLO, G., and NÄGERL, H.-C., "Realization of an excited, strongly correlated quantum gas phase," *Science*, vol. 325, pp. 1224–1227, Sept. 2009.
- [74] HÄNSEL, W., HOMMELHOFF, P., HÄNSCH, T. W., and REICHEL, J., "Bose-Einstein condensation on a microelectronic chip," *Nature*, vol. 413, pp. 498–501, Oct. 2001.
- [75] HOFFERBERTH, S., LESANOVSKY, I., FISCHER, B., SCHUMM, T., and SCHMIEDMAYER, J., "Non-equilibrium coherence dynamics in one-dimensional Bose gases," *Nature*, vol. 449, pp. 324–327, Sept. 2007.
- [76] HOFFERBERTH, S., LESANOVSKY, I., SCHUMM, T., IMAMBEKOV, A., GRITSEV, V., DEMLER, E., and SCHMIEDMAYER, J., "Probing quantum and thermal noise in an interacting many-body system," *Nature Physics*, vol. 4, pp. 489–495, June 2008.
- [77] HUET, L., AMMAR, M., MORVAN, E., SARAZIN, N., POCHOLLE, J.-P., REICHEL, J., GUERLIN, C., and SCHWARTZ, S., "Magneto-optical trapping and detection of atoms through a transparent atom chip," in *Proceedings of the International Quantum Electronics Conference and Conference on Lasers and Electro-Optics Pacific Rim 2011*, p. I1188, Optical Society of America, Aug. 2011.

- [78] HUGBART, M., RETTER, J. A., GERBIER, F., VARÓN, A. F., RICHARD, S., THYWISSEN, J. H., CLÉMENT, D., BOUYER, P., and ASPECT, A., "Coherence length of an elongated condensate," *The European Physical Journal D - Atomic, Molecular, Optical and Plasma Physics*, vol. 35, pp. 155–163, Aug. 2005.
- [79] HUNG, C.-L., ZHANG, X., GEMELKE, N., and CHIN, C., "Observation of scale invariance and universality in two-dimensional Bose gases," *Nature*, vol. 470, pp. 236–239, Feb. 2011.
- [80] IMAI, H., INABA, K., TANJI-SUZUKI, H., YAMASHITA, M., and MUKAI, T., "Bose-Einstein condensate on a persistent-supercurrent atom chip," *Applied Physics B*, pp. 1–9, Feb. 2014.
- [81] IMAMBEKOV, A., MAZETS, I. E., PETROV, D. S., GRITSEV, V., MANZ, S., HOFFERBERTH, S., SCHUMM, T., DEMLER, E., and SCHMIEDMAYER, J., "Density ripples in expanding low-dimensional gases as a probe of correlations," *Physical Review A*, vol. 80, p. 033604, Sept. 2009.
- [82] JACQMIN, T., *Mesures de corrélations dans un gaz de bosons unidimensionnel sur puce*. PhD thesis, Université Paris Sud - Paris XI, Nov. 2012.
- [83] JACQMIN, T., ARMIJO, J., BERRADA, T., KHERUNTSYAN, K. V., and BOUCHOULE, I., "Sub-poissonian fluctuations in a 1D Bose gas: From the quantum quasicondensate to the strongly interacting regime," *Physical Review Letters*, vol. 106, p. 230405, June 2011.
- [84] JACQMIN, T., FANG, B., BERRADA, T., ROSCILDE, T., and BOUCHOULE, I., "Momentum distribution of one-dimensional Bose gases at the quasicondensation crossover: Theoretical and experimental investigation," *Physical Review A*, vol. 86, p. 043626, Oct. 2012.
- [85] JASKULA, J.-C., PARTRIDGE, G. B., BONNEAU, M., LOPES, R., RUAUDEL, J., BOIRON, D., and WESTBROOK, C. I., "Acoustic analog to the dynamical casimir effect in a Bose-Einstein condensate," *Physical Review Letters*, vol. 109, p. 220401, Nov. 2012.
- [86] JIN, D. S., ENSHER, J. R., MATTHEWS, M. R., WIEMAN, C. E., and CORNELL, E. A., "Collective excitations of a Bose-Einstein condensate in a dilute gas," *Physical Review Letters*, vol. 77, pp. 420–423, July 1996.

- [87] JIN, D. S., MATTHEWS, M. R., ENSHER, J. R., WIEMAN, C. E., and CORNELL, E. A., "Temperature-dependent damping and frequency shifts in collective excitations of a dilute Bose-Einstein condensate," *Physical Review Letters*, vol. 78, pp. 764–767, Feb. 1997.
- [88] JOHNSON, A., *Noise Thermometry in a One-dimensional Bose Gas*. Master internship report, ENS de Lyon, Lyon, 2012.
- [89] JOSE, S., SURENDRAN, P., WANG, Y., HERRERA, I., KRZEMIEN, L., WHITLOCK, S., MCLEAN, R., SIDOROV, A., and HANNAFORD, P., "Periodic array of Bose-Einstein condensates in a magnetic lattice," *Physical Review A*, vol. 89, p. 051602, May 2014.
- [90] KARBACH, M., MÜLLER, G., GOULD, H., and TOBOCHNIK, J., "Introduction to the Bethe Ansatz I," *Computers in Physics*, vol. 11, pp. 36–43, Jan. 1997.
- [91] KARBACH, M., HU, K., and MÜLLER, G., "Introduction to the Bethe Ansatz III," *arXiv:cond-mat/0008018*, Aug. 2000.
- [92] KARBACH, M., HU, K., and MÜLLER, G., "Introduction to the Bethe Ansatz II," *Computers in Physics*, vol. 12, pp. 565–573, Nov. 1998.
- [93] KHERUNTSYAN, K. V., GANGARDT, D. M., DRUMMOND, P. D., and SHLYAPNIKOV, G. V., "Finite-temperature correlations and density profiles of an inhomogeneous interacting one-dimensional Bose gas," *Physical Review A*, vol. 71, p. 053615, May 2005.
- [94] KINOSHITA, T., WENGER, T., and WEISS, D. S., "A quantum newton's cradle," *Nature*, vol. 440, pp. 900–903, Apr. 2006.
- [95] KINOSHITA, T., WENGER, T., and WEISS, D. S., "A quantum newton's cradle," *Nature*, vol. 440, pp. 900–903, Apr. 2006.
- [96] KOREPIN, V. E., "Calculation of norms of bethe wave functions," *Communications in Mathematical Physics*, vol. 86, no. 3, pp. 391–418, 1982.
- [97] KOREPIN, V. E., BOGOLIUBOV, N. M., and IZERGIN, A. G., *Quantum Inverse Scattering Method and Correlation Functions*. Cambridge University Press, 1993.

- [98] KRÜGER, P., HOFFERBERTH, S., MAZETS, I. E., LESANOVSKY, I., and SCHMIEDMAYER, J., “Weakly interacting Bose gas in the one-dimensional limit,” *Physical Review Letters*, vol. 105, p. 265302, Dec. 2010.
- [99] LAMPORESI, G., DONADELLO, S., SERAFINI, S., DALFOVO, F., and FERRARI, G., “Spontaneous creation of kibble-zurek solitons in a Bose-Einstein condensate,” *Nature Physics*, vol. 9, pp. 656–660, Oct. 2013.
- [100] LANGEN, T., GEIGER, R., KUHNERT, M., RAUER, B., and SCHMIEDMAYER, J., “Local emergence of thermal correlations in an isolated quantum many-body system,” *Nature Physics*, vol. 9, pp. 640–643, Oct. 2013.
- [101] LANGEN, T., GEIGER, R., and SCHMIEDMAYER, J., “Ultracold atoms out of equilibrium,” *arXiv:1408.6377 [cond-mat]*, Aug. 2014.
- [102] LIEB, E. H., “Exact analysis of an interacting Bose gas. II. the excitation spectrum,” *Physical Review*, vol. 130, pp. 1616–1624, May 1963.
- [103] LIEB, E. H. and LINIGER, W., “Exact analysis of an interacting Bose gas. I. the general solution and the ground state,” *Physical Review*, vol. 130, pp. 1605–1616, May 1963.
- [104] LUITEN, O. J., REYNOLDS, M. W., and WALRAVEN, J. T. M., “Kinetic theory of the evaporative cooling of a trapped gas,” *Physical Review A*, vol. 53, pp. 381–389, Jan. 1996.
- [105] MANZ, S., BÜCKER, R., BETZ, T., KOLLER, C., HOFFERBERTH, S., MAZETS, I. E., IMAMBEKOV, A., DEMLER, E., PERRIN, A., SCHMIEDMAYER, J., and SCHUMM, T., “Two-point density correlations of quasicondensates in free expansion,” *Physical Review A*, vol. 81, p. 031610, Mar. 2010.
- [106] MARAGÒ, O. M., HOPKINS, S. A., ARLT, J., HODBY, E., HECHENBLAIKNER, G., and FOOT, C. J., “Observation of the scissors mode and evidence for superfluidity of a trapped Bose-Einstein condensed gas,” *Physical Review Letters*, vol. 84, pp. 2056–2059, Mar. 2000.
- [107] MENOTTI, C. and STRINGARI, S., “Collective oscillations of a one-dimensional trapped Bose-Einstein gas,” *Physical Review A*, vol. 66, p. 043610, Oct. 2002.

- [108] MEWES, M.-O., ANDREWS, M. R., VAN DRUTEN, N. J., KURN, D. M., DURFEE, D. S., TOWNSEND, C. G., and KETTERLE, W., "Collective excitations of a Bose-Einstein condensate in a magnetic trap," *Physical Review Letters*, vol. 77, pp. 988–991, Aug. 1996.
- [109] MINGUZZI, A. and GANGARDT, D. M., "Exact coherent states of a harmonically confined tonks-girardeau gas," *Physical Review Letters*, vol. 94, p. 240404, June 2005.
- [110] MORITZ, H., STÖFERLE, T., KÖHL, M., and ESSLINGER, T., "Exciting collective oscillations in a trapped 1D gas," *Physical Review Letters*, vol. 91, p. 250402, Dec. 2003.
- [111] MÜLLER, K., *Coherent transport of ultracold atoms in disordered potentials: Manipulation of time-reversal symmetry in weak localization experiments*. PhD thesis, Université Paris Sud - Paris XI, 2014.
- [112] NEUDECK, P. G., "Silicon carbide," *The VLSI Handbook*, 2012.
- [113] OLSHANII, M., "Atomic scattering in the presence of an external confinement and a gas of impenetrable bosons," *Physical Review Letters*, vol. 81, pp. 938–941, Aug. 1998.
- [114] ONOFRIO, R., DURFEE, D. S., RAMAN, C., KÖHL, M., KUKLEWICZ, C. E., and KETTERLE, W., "Surface excitations of a Bose-Einstein condensate," *Physical Review Letters*, vol. 84, pp. 810–813, Jan. 2000.
- [115] OTT, H., FORTÁGH, J., KRAFT, S., GÜNTHER, A., KOMMA, D., and ZIMMERMANN, C., "Nonlinear dynamics of a Bose-Einstein condensate in a magnetic waveguide," *Physical Review Letters*, vol. 91, p. 040402, July 2003.
- [116] OTT, H., , FORTÁGH, J., and ZIMMERMANN, C., "Dynamics of a Bose-Einstein condensate in an anharmonic trap," *Journal of Physics B: Atomic, Molecular and Optical Physics*, vol. 36, p. 2817, July 2003.
- [117] OTTENSTEIN, T. B., *A New Objective for High Resolution Imaging of Bose-Einstein Condensates*. Diploma thesis.
- [118] PETROV, D. S., SHLYAPNIKOV, G. V., and WALRAVEN, J. T. M., "Regimes of quantum degeneracy in trapped 1D gases," *Physical Review Letters*, vol. 85, pp. 3745–3749, Oct. 2000.

- [119] POLKOVNIKOV, A., SENGUPTA, K., SILVA, A., and VENGALATTORE, M., “Colloquium: Nonequilibrium dynamics of closed interacting quantum systems,” *Reviews of Modern Physics*, vol. 83, pp. 863–883, Aug. 2011.
- [120] RATH, S. P., *Production and investigation of quasi-two-dimensional Bose gases*. PhD thesis, Université Pierre et Marie Curie - Paris VI, Feb. 2010.
- [121] REICHEL, J., “Microchip traps and Bose-Einstein condensation,” *Applied Physics B*, vol. 74, pp. 469–487, Apr. 2002.
- [122] REICHEL, J., HÄNSEL, W., and HÄNSCH, T. W., “Atomic micromanipulation with magnetic surface traps,” *Physical Review Letters*, vol. 83, pp. 3398–3401, Oct. 1999.
- [123] REINAUDI, G., LAHAYE, T., WANG, Z., and GUÉRY-ODELIN, D., “Strong saturation absorption imaging of dense clouds of ultracold atoms,” *Optics Letters*, vol. 32, pp. 3143–3145, Nov. 2007.
- [124] RICHARD, S., GERBIER, F., THYWISSEN, J. H., HUGBART, M., BOUYER, P., and ASPECT, A., “Momentum spectroscopy of 1D phase fluctuations in Bose-Einstein condensates,” *Physical Review Letters*, vol. 91, p. 010405, July 2003.
- [125] RITTER, S., ÖTTL, A., DONNER, T., BOURDEL, T., KÖHL, M., and ESSLINGER, T., “Observing the formation of long-range order during Bose-Einstein condensation,” *Physical Review Letters*, vol. 98, p. 090402, Mar. 2007.
- [126] RÖCK, N., *Quantum manipulation on the Barium quadrupolar transition*. Diploma thesis, University of Innsbruck, 2011.
- [127] ROHRINGER, W., private communications, 2014.
- [128] ROHRINGER, W., FISCHER, D., STEINER, F., MAZETS, I. E., SCHMIED-MAYER, J., and TRUPKE, M., “Scaling of phonons and shortcuts to adiabaticity in a one-dimensional quantum system,” *arXiv:1312.5948 [cond-mat]*, Dec. 2013. arXiv: 1312.5948.
- [129] ROTTER, D., *Quantum feedback and quantum correlation measurements with a single Barium ion*. PhD thesis, Leopold-Franzens-Universität Innsbruck, 2008.

- [130] ROUX, C., EMMERT, A., LUPASCU, A., NIRRENGARTEN, T., NOGUES, G., BRUNE, M., RAIMOND, J.-M., and HAROCHE, S., "Bose-Einstein condensation on a superconducting atom chip," *Europhysics Letters*, vol. 81, p. 56004, Mar. 2008.
- [131] ROWE, D. J., *Nuclear Collective Motion: Models and Theory*. World Scientific, 2010.
- [132] ROWEN, E. E., BAR-GILL, N., PUGATCH, R., and DAVIDSON, N., "Energy-dependent damping of excitations over an elongated Bose-Einstein condensate," *Physical Review A*, vol. 77, p. 033602, Mar. 2008.
- [133] SADLER, L. E., HIGBIE, J. M., LESLIE, S. R., VENGALATTORE, M., and STAMPER-KURN, D. M., "Spontaneous symmetry breaking in a quenched ferromagnetic spinor Bose-Einstein condensate," *Nature*, vol. 443, pp. 312–315, Sept. 2006.
- [134] SANDVIK, A. W., "Computational studies of quantum spin systems," in *AIP Conference Proceedings*, vol. 1297, pp. 135–338, AIP Publishing, Nov. 2010.
- [135] SCHMIDT, B. and FLEISCHHAUER, M., "Exact numerical simulations of a one-dimensional trapped Bose gas," *Physical Review A*, vol. 75, p. 021601, Feb. 2007.
- [136] SCHMIED, R., LEIBFRIED, D., SPREEUW, R. J. C., and WHITLOCK, S., "Optimized magnetic lattices for ultracold atomic ensembles," *New Journal of Physics*, vol. 12, p. 103029, Oct. 2010.
- [137] SCHUMM, T., *Bose-Einstein condensates in magnetic double well potentials*. PhD thesis, Université Paris Sud - Paris XI, Feb. 2006.
- [138] SHERSON, J. F., WEITENBERG, C., ENDRES, M., CHENEAU, M., BLOCH, I., and KUHR, S., "Single-atom-resolved fluorescence imaging of an atomic mott insulator," *Nature*, vol. 467, pp. 68–72, Sept. 2010.
- [139] SORTAIS, Y. R. P., MARION, H., TUCHENDLER, C., LANCE, A. M., LAMARE, M., FOURNET, P., ARMELLIN, C., MERCIER, R., MESSIN, G., BROWAEYS, A., and GRANGIER, P., "Diffraction-limited optics for single-atom manipulation," *Physical Review A*, vol. 75, p. 013406, Jan. 2007.

- [140] STECK, D. A., *Rubidium 87 D line data*. 2001.
- [141] STIMMING, H.-P., MAUSER, N. J., SCHMIEDMAYER, J., and MAZETS, I. E., "Fluctuations and stochastic processes in one-dimensional many-body quantum systems," *Physical Review Letters*, vol. 105, p. 015301, July 2010.
- [142] STOCK, S., BRETIN, V., CHEVY, F., and DALIBARD, J., "Shape oscillation of a rotating Bose-Einstein condensate," *Europhysics Letters*, vol. 65, p. 594, Mar. 2004.
- [143] STRINGARI, S., "Collective excitations of a trapped Bose-condensed gas," *Physical Review Letters*, vol. 77, pp. 2360–2363, Sept. 1996.
- [144] STRINGARI, S., "Dynamics of Bose-Einstein condensed gases in highly deformed traps," *Physical Review A*, vol. 58, pp. 2385–2388, Sept. 1998.
- [145] SYLJUÅSEN, O. F., "Directed loop updates for quantum lattice models," *Physical Review E*, vol. 67, p. 046701, Apr. 2003.
- [146] TEY, M. K., SIDORENKOV, L. A., GUAJARDO, E. R. S., GRIMM, R., KU, M. J. H., ZWIERLEIN, M. W., HOU, Y.-H., PITAEVSKII, L., and STRINGARI, S., "Collective modes in a unitary fermi gas across the superfluid phase transition," *Physical Review Letters*, vol. 110, p. 055303, Jan. 2013.
- [147] TREBBIA, J.-B., ESTEVE, J., WESTBROOK, C. I., and BOUCHOULE, I., "Experimental evidence for the breakdown of a hartree-fock approach in a weakly interacting Bose gas," *Physical Review Letters*, vol. 97, p. 250403, Dec. 2006.
- [148] TREBBIA, J.-B., *Etude de gaz quantiques dégénérés quasi-unidimensionnels confinés par une micro-structure*. PhD thesis, Université Paris Sud - Paris XI, Oct. 2007.
- [149] TROTZKY, S., CHEN, Y.-A., FLESCHE, A., MCCULLOCH, I. P., SCHOLLWÖCK, U., EISERT, J., and BLOCH, I., "Probing the relaxation towards equilibrium in an isolated strongly correlated one-dimensional Bose gas," *Nature Physics*, vol. 8, pp. 325–330, Apr. 2012.

- [150] VAN AMERONGEN, A. H., VAN ES, J. J. P., WICKE, P., KHERUNTSYAN, K. V., and VAN DRUTEN, N. J., "Yang-yang thermodynamics on an atom chip," *Physical Review Letters*, vol. 100, p. 090402, Mar. 2008.
- [151] VIGNERON, K., *Contrôle du bruit quantique de la lumière et mesures quantiques non destructives utilisant des atomes piégés et refroidis*. PhD thesis, Université Paris Sud - Paris XI, July 1998.
- [152] VIGNOLO, P. and MINGUZZI, A., "Universal contact for a tonks-girardeau gas at finite temperature," *Physical Review Letters*, vol. 110, p. 020403, Jan. 2013.
- [153] VOGLER, A., LABOUVIE, R., STUBENRAUCH, F., BARONTINI, G., GUARRERA, V., and OTT, H., "Thermodynamics of strongly correlated one-dimensional Bose gases," *Physical Review A*, vol. 88, p. 031603, Sept. 2013.
- [154] WIDERA, A., TROTZKY, S., CHEINET, P., FÖLLING, S., GERBIER, F., BLOCH, I., GRITSEV, V., LUKIN, M. D., and DEMLER, E., "Quantum spin dynamics of mode-squeezed luttinger liquids in two-component atomic gases," *Physical Review Letters*, vol. 100, p. 140401, Apr. 2008.
- [155] YANG, C. N. and YANG, C. P., "Thermodynamics of a one-dimensional system of bosons with repulsive delta-function interaction," *Journal of Mathematical Physics*, vol. 10, no. 7, p. 1115, 1969.
- [156] ZIMMERMANN, B., MÜLLER, T., MEINEKE, J., ESSLINGER, T., and MORITZ, H., "High-resolution imaging of ultracold fermions in microscopically tailored optical potentials," *New Journal of Physics*, vol. 13, p. 043007, Apr. 2011.